

# **AIMS Materials science**

**VOLUME NO. 10**  
**ISSUE NO. 2**  
**MAY- AUGUST 2023**

**EIS LEARNING**

**No - 198, Upper Hatia, Near Mahatma Gandhi  
Smarak High School, Ranchi - 834003, Jharkhand  
Ph : 919097302256 / Email : [info@eislearning.com](mailto:info@eislearning.com)**

# AIMS Materials science

## **AIMAND SCOPE**

AIMS Materials science is an international journal devoted to publishing peer-reviewed, high quality, original papers in the field of Materials science. We publish the following article types: original research articles, reviews, editorials, letters, and conference reports.

**AIMS Materials Science welcomes, but not limited to, the papers from the following topics:**

- Biological materials
- Ceramics
- Composite materials
- Magnetic materials
- Medical implant materials
- New properties of materials
- Nanoscience and nanotechnology
- Polymers
- Thin films

**Editor in Chief**

<b>Qing Hua Qin</b> Department of Engineering, Shenzhen MSU-BIT University, 1 International University Park Road, Longgang, Shenzhen, Guangdong, 518172, China	<b>Bo Tang</b> Shandong Normal University, 88 East Wenhua Road, Jinan, Shandong, China
---	--

**Founding Editor in Chief**

**Yaroslava G. Yingling**  
Department of Materials Science and Engineering, North Carolina State University,  
Campus Box 7907, Raleigh, NC 27695-7907, USA

**Managing Editor**

Dr. Xu Guo  
Managing and Operation (Journal)

**Editorial Board**

<b>Maria Antonietta Aiello</b> Department of Engineering for Innovation, University of Salento, 73100 Lecce, Italy	<b>Indika U. Arachchige</b> Department of Chemistry, Virginia Commonwealth University, United States
<b>Mario Beiner Fraunhofer</b> Institute for Microstructure of Materials and Systems IMWS, Walter-Hülse-Str. 1, 06120 Halle (Saale), Germany	<b>J. Paige Buchanan</b> US Army Corps of Engineers, Engineering Research and Development Center, Vicksburg, MS, USA
<b>Detlef Bahnemann</b> Institut fuer Technische Chemie, Gottfried Wilhelm Leibniz Universitaet Hannover, Callinstrasse 3, D-30167, Hannover, Germany; Saint-Petersburg State University, Ulyanovskaya str. 1, Peterhof, Saint-Petersburg, 198504, Russia	<b>Kaiyong Cai Key</b> Laboratory of Biorheological Science and Technology, Ministry of Education, College of Bioengineering, Chongqing University, Chongqing, 400044, China
<b>Miguel A. Cambor</b> Instituto de Ciencia de Materiales de Madrid, ICMM- CSIC, Sor Juana Inés de la Cruz, 3, 28039 Madrid, Spain	<b>Surojit Chattopadhyay</b> Institute of Biophotonics, National Yang Ming University, Taipei-112, Taiwan
<b>Daolun Chen</b> Department of Mechanical and Industrial Engineering, Ryerson University, 350 Victoria Street, Toronto, Ontario M5B 2K3, Canada	<b>Jian Chen</b> Department of Chemistry, Western University, 1511 Richmond Street, London, ON, N6A 5B7, Canada
<b>Chong Cheng</b> Department of Chemical and Biological Engineering, University at Buffalo, The State University of New York Buffalo, NY 14260-4200, USA	<b>Phillip Y. K. Choi</b> Donadeo Innovation Centre for Engineering, Department of Chemical & Materials Engineering, University of Alberta, Edmonton, Alberta, T6G 1H9, Canada
<b>Amitava Choudhury</b> Department of Chemistry, Missouri S & T, Rolla, MO 65409, USA	<b>John D. Clayton</b> Impact Physics Department, RDRL-WMP-C, US ARL Aberdeen Proving Ground, MD 21005-5066, USA
<b>Pantaleo Davide Cozzoli</b> Department of Mathematics and Physics, University of Salento, Via Arnesano-73100 Lecce, Italy; CNR NANOTEC-Institute of Nanotechnology, c/o campus Ecotekne, Via Monteroni-73100 Lecce, Italy	<b>A. Cremades</b> Departamento de Física de Materiales, Facultad de Ciencias Físicas, Universidad Complutense de Madrid, 28040 Madrid, Spain
<b>Giuseppe Cruciani</b> Department of Physics and Earth Sciences, University of Ferrara, Via Saragat 1, Bld B Room 209, I-44122 Ferrara, Italy	<b>NilY R. Dan</b> Chemical and Biological Engineering, Drexel University, 3141 Chestnut St., Philadelphia, PA 19104, USA

<p><b>Darren Sun Delai</b> School of Civil and Environmental Engineering, Nanyang Technological University, Singapore 639798, Singapore</p>	<p><b>Yubin Dong</b> College of Chemistry, Chemical Engineering and Material Science, Shandong Normal University, China</p>
<p><b>Antonio Facchetti</b> Department of Chemistry and the Materials Research Center, Northwestern University, 2145 Sheridan Road, Evanston, IL 60208-3113, USA</p>	<p><b>Chunhai Fan</b> Shanghai institute of applied physics, University of Chinese Academy of Sciences, China</p>
<p><b>Te-Hua Fang</b> Department of Mechanical Engineering, National Kaohsiung University of Science and Technology, Kaohsiung 807, Taiwan</p>	<p><b>Paulina Faria</b> Department of Civil Engineering, NOVA School of Science and Technology, Universidade NOVA de Lisboa, 2829-516 Caparica, Portugal</p>
<p><b>Peter Fischer</b> Center for X-ray Optics, Lawrence Berkeley National Laboratory, 1 Cyclotron Road, Berkeley, CA 94720, USA</p>	<p><b>Ines Flores-Colen</b> Construction Section, Department of Civil Engineering, Architecture and Georesources, Instituto Superior Técnico, University of Lisbon, Avenue Rovisco Pais, Lisbon 1049-001, Portugal</p>
<p><b>Francisco Gallego-Gómez</b> Instituto de Ciencia de Materiales de Madrid, C/Sor Juana Inés de la Cruz 3, 28049 Madrid, Spain</p>	<p><b>Xiaonan Gao</b> College of Chemistry, Chemical Engineering and Materials Science, Shandong Normal University, Jinan, Shandong, China</p>
<p><b>Elhem Ghorbel</b> Université de Cergy Pontoise, 5 Mail Guy Lussac Neuville sur Oise, 95031 Cergy Pontoise Cedex, France</p>	<p><b>Juan Cabanillas Gonzalez</b> Madrid Institute for Advanced Studies in Nanoscience, IMDEA Nanociencia, Calle Faraday 9, Ciudad Universitaria de Cantoblanco, 28049 Madrid, Spain</p>
<p><b>Fabrizio Greco</b> Department of Civil Engineering, University of Calabria, 87036 Rende, Cosenza, Italy</p>	<p><b>Anders Hagfeldt</b> Department of Physical and Analytical Chemistry, Uppsala University, Box 259, 75105 Uppsala, Sweden</p>
<p><b>Yang Han</b> Harbin Engineering University, Nantong street, Nangang Distrit, Harbin, Heilongjiang, China</p>	<p><b>Anming Hu</b> Department of Mechanical, Aerospace and Biomedical Engineering, University of Tennessee, 509 Dougherty Engineering Building, Knoxville, TN 37996-2210, USA</p>
<p><b>Xiaodong Huang</b> Faculty of Science, Engineering and Technology, Swinburne University of Technology, Hawthorn, VIC 3122, Australia</p>	<p><b>Christoph Janiak</b> Institut für Anorganische Chemie und Strukturchemie, Universitaet Duesseldorf, Universitaetsstrasse, D-40225 Düsseldorf, Germany</p>
<p><b>Animesh Jha</b> The Institute for Materials Research, University of Leeds, Leeds, LS2 9JT, UK</p>	<p><b>Yang Jiao</b> Materials Science and Engineering, School for Engineering and Matter, Transport and Energy, Arizona State University, Tempe, AZ 85287-6106, USA</p>
<p><b>Andrey P. Jivkov</b> School of Mechanical, Aerospace and Civil Engineering (MACE), The University of Manchester (UoM), Oxford Road, Manchester M13 9PL, UK</p>	<p><b>Kourosh Kalantar-zadeh</b> School of Engineering, RMIT University, Melbourne, VIC 3000, Australia</p>
<p><b>Susan M. Kauzlarich</b> Department of Chemistry, University of California, One Shields Ave, Davis, California 95616, United States</p>	<p><b>Guido Kickelbick</b> Inorganic Solid State Chemistry, Saarland University, Am Markt Zeile 3, 66125 Saarbrücken, Germany</p>
<p><b>Ji-Seon Kim</b> Department of Physics &amp; Centre for Plastic Electronics, Imperial College London, London SW7 2AZ, United Kingdom</p>	<p><b>Khalid Lamnawar</b> Department of Mechanical Engineering, University of Lyon, 20 Avenue A. Einstein, F-69621 Villeurbanne, France</p>

<p><b>Yong Lei Fachgebietsleiter (Head),</b> Fachgebiet 3D-Nanostrukturierung (Chair of 3D-Nanostructuring), Institute of Physics, Faculty of Mathematics and Nature Sciences, Technical University of Ilmenau (Technische Universität Ilmenau), Germany</p>	<p><b>Dawen Li</b> Electrical &amp; Computer Engineering, Box 870286, University of Alabama, Tuscaloosa, AL 35487-0286, USA</p>
<p><b>Ping Li</b> College of Chemistry, Chemical Engineering and Materials Science, Shandong Normal University, Jinan 250014, China</p>	<p><b>Sean Li</b> School of Materials Science and Engineering, The University of New South Wales, Sydney, NSW 2052, Australia</p>
<p><b>Dongsheng Liu</b> Department of Chemistry, Tsinghua University, China Kaohsiung 807, Taiwan</p>	<p><b>Zhuang Liu</b> Functional Nano &amp; Soft Materials Laboratory, Soochow University, China</p>
<p><b>Lin Liu</b> Department of Materials Science and Engineering and State Key Lab for Materials Processing and Die &amp; Mould Technology, Huazhong University of Science and Technology, Wuhan 430074, China</p>	<p><b>Altino Loureiro</b> Department of Mechanical Engineering, University of Coimbra, Pinhal de Marrocos, 3030- 788 Coimbra, Portugal</p>
<p><b>It-Meng (Jim)</b> Low Department of Imaging &amp; Applied Physics, Curtin University, GPO Box U1987, Perth, WA 6845, Australia</p>	<p><b>Enzo Martinelli</b> Department of Civil Engineering, University of Salerno, Via Giovanni Pallo II, 132 84084 Fisciano (SA), Italy</p>
<p><b>Tullio Monetta</b> Department of Chemical Engineering, Materials and Industrial Production, University of Napoli Federico II, Piazzale Tecchio 80, 80125 Napoli, Italy</p>	<p><b>Klaus Müllen</b> Max Planck Institute for Polymer Research Ackermannweg 10, D-55128 Mainz ,Germany</p>
<p><b>Franck Natali</b> School of Chemical and Physical Sciences , Victoria University, Wellington, New Zealand</p>	<p><b>Manashi Nath</b> Department of Chemistry, Missouri University of Science and Technology, Rolla, Missouri 65409, United States</p>
<p><b>Phuong Nguyen-Tri</b> Department of Chemistry, Biochemistry and Physic, University of Quebec in Trois-Rivières, Québec, Canada</p>	<p><b>Shigenobu Ogata</b> Department of Mechanical Science and Bioengineering, Graduate School of Engineering Science, Osaka University, Osaka 560-8531, Japan</p>
<p><b>Amir Pakdel</b> School of Chemistry, University College Dublin (UCD), Belfield, Dublin, Ireland</p>	<p><b>Dario Pasini</b> Department of Chemistry, University of Pavia, Via Taramelli, 10-27100, Pavia, Italy</p>
<p><b>Daiwen Pang</b> College of Chemistry and Molecular Sciences, Wuhan University, China</p>	<p><b>Srikanth Patala</b> Department of Materials Science and Engineering, North Carolina State University, 911 Partners Way, Engineering Building I, Room 3002, Raleigh, NC 27606, USA</p>
<p><b>Andrey P. Jivkov</b> School of Mechanical, Aerospace and Civil Engineering (MACE), The University of Manchester (UoM), Oxford Road, Manchester M13 9PL, UK</p>	<p><b>Kouros Kalantar-zadeh</b> School of Engineering, RMIT University, Melbourne, VIC 3000, Australia</p>
<p><b>Durga Paudyal</b> Division of Materials Sciences and Engineering, The Ames Laboratory, US Department of Energy, Iowa State University, Ames, IA 50011-3020, USA</p>	<p><b>Jian Pei</b> College of Chemistry and Molecular Engineering, Peking University, China</p>
<p><b>Yong Pei</b> Department of Chemistry, Xiangtan University, China</p>	<p><b>Russo Pietro</b> Institute for Polymers, Composites and Biomaterials of National Research Council, Via Campi Flegrei 34, 80078 Pozzuoli, NA, Italy</p>

<p><b>Gustavo Portalone</b> Department of Chemistry, 'La Sapienza' University of Rome, 00185 Rome, Italy</p>	<p><b>Sandipan Pramanik</b> Department of Electrical and Computer Engineering, University of Alberta, Canada</p>
<p><b>Faxiang Qin</b> 1D Nanomaterials Group, National Institute for Materials Science, 1-2-1 Sengen, Tsukuba, Ibaraki 305-0047, Japan</p>	<p><b>Bhakta B. Rath</b> US Naval Research Laboratory, Washington, DC 20375-5341, USA</p>
<p><b>Mauro Ricotta</b> Department of Industrial Engineering, University of Padova, Italy</p>	<p><b>Evgeny Rebrov</b> School of Engineering, University of Warwick, Library Road, CV4 7AL, Coventry, UK</p>
<p><b>Tomasz Sadowski</b> Department of Solid Mechanics, Lublin University of Technology, 20-865 Lublin, Nadbystrzycka 40 Str., Poland</p>	<p><b>Jacobo Santamaria</b> Applied Physics Department, Universidad Complutense de Madrid, Campus Moncloa, Madrid, 28040, Spain</p>
<p><b>Hua Song</b> Department of Chemical and Petroleum Engineering, University of Calgary, 2500 University Drive, NW, Calgary, Alberta T2N 1N4, Canada</p>	<p><b>Hélder Almeida Santos</b> Division of Pharmaceutical Technology, Faculty of Pharmacy, University of Helsinki, FI-00014, Finland</p>
<p><b>Atsushi Shishido</b> Chemical Resources Laboratory, Tokyo Institute of Technology, R1-12, 4259 Nagatsuta, Midori-ku, Yokohama 226-8503, Japan</p>	<p><b>Adam Z. Stieg</b> California NanoSystems Institute, University of California, Los Angeles, CA 90095, USA</p>
<p><b>Xuping Sun</b> College of Chemistry, Sichuan University, China</p>	<p><b>Mukundan Thelakkat</b> Applied Functional Polymers, Macromolecular Chemistry I, University of Bayreuth, 95440 Bayreuth, Germany</p>
<p><b>Alexander Umantsev</b> Department of Chemistry/Physics, Fayetteville State University, Fayetteville, NC 28301, USA</p>	<p><b>Kalman Varga</b> Department of Physics and Astronomy, Vanderbilt University, Nashville, USA</p>
<p><b>Pasquale Vena</b> Department of Chemistry, Materials and Chemical Engineering, Giulio Natta, Laboratory of Biological Structure Mechanics (LaBS), Politecnico di Milano, Piazza Leonardo da Vinci, 32-20133 Milano, Italy</p>	<p><b>Hao Wang</b> Institute of Metal Research, Chinese Academy of Sciences, Shenyang 110016, China</p>
<p><b>Qiang (David) Wang</b> Department of Chemical and Biological Engineering and School of Biomedical Engineering, Colorado State University, USA</p>	<p><b>Haiming Wen</b> Department of Physics, Nuclear and Electrical Engineering, Idaho State University, Idaho Falls, ID 83402, USA</p>
<p><b>Yiquan Wu Kazuo</b> Inamori School of Engineering, New York State College of Ceramics, Alfred University, 2 Pine Street, Alfred, NY 14802-1296, USA</p>	<p><b>Yu-Fei Wu</b> School of Engineering, RMIT University, 376-392 Swanston St, Melbourne GPO Box 2476V, Melbourne VIC 3001, Australia</p>
<p><b>Kai Xiao</b> Center for Nanophase Materials Sciences, Oak Ridge National Laboratory, Bldg 8610, MS-6494, Oak Ridge, TN 37831-6494, USA</p>	<p><b>Jun Yan</b> College of Material Science and Chemical Engineering, Harbin Engineering University, China</p>
<p><b>Yonggang Yang</b> Department of Polymer Science and Engineering, College of Chemistry, Chemical Engineering and Materials Science, Soochow University, Suzhou 215123, China</p>	<p><b>Bin Zhang</b> Department of Chemistry, Tianjin University, China</p>

<b>Chunyang Zhang</b> College of Chemistry, Chemical Engineering and Material Science, Shandong Normal University, China	<b>Junjie Zhang</b> Center for Precision Engineering, Harbin Institute of Technology, China
<b>Liangchi Zhang</b> School of Mechanical and Manufacturing Engineering, The University of New South Wales, NSW, 2052, Australia	<b>Qinyuan Zhang</b> MOE Key Lab of Specially Functional Materials and Institute of Optical Communication Materials, South China University of Technology, Guangzhou 510641, China
<b>Chengzhou Zhu</b> College of Chemistry, Central China Normal University, Wuhan 430079, China	<b>Jianxi Zhu</b> Key Laboratory of Mineralogy and Metallogeny, Guangzhou Institute of Geochemistry, Chinese Academy of Sciences, 511 Kehua St. Wushan, Guangzhou, 510640, China
<b>Zheng Hong (George) Zhu</b> Department of Mechanical Engineering, York University, 435C Bergeron Centre for Engineering Excellence, 4700 Keele Street, Toronto, Canada	

# AIMS Materials science

(Volume No. 10, Issue No. 2, May-August 2023)

## Contents

Sr. No.	Articles / Authors Name	Pg. No.
1	Electrospinning Process Control for Fiber- Structured Poly (Bisphenol A-co-Epichlorohydrin) Membrane - <i>Wisawat Keaswejjareansuk, Xiang Wang, Richard D. Sisson and Jianyu Liang</i>	54 - 63
2	Hydrogen Generation Performance of Al–20at%Ca alloy Synthesized by Mechanical Alloying - <i>A. G. Hernández-Torres, J. L. López-Miranda, I. Santos-Ramos and G. Rosas</i>	64 - 75
3	Construction and Building Materials - <i>Anrea Di Schino and Marco Corradi</i>	76 - 77
4	Structural and Multiferroic Properties of (S <sub>m</sub> , M <sub>n</sub> ) Co-Doped BiFeO <sub>3</sub> Materials - <i>Dao Viet Thang, Nguyen Manh Hung, Nguyen Cao Khang and Le Thi Mai Oanh</i>	78 - 85
5	Large Effects of Tiny Structural Changes on the Cluster Formation Process in Model Colloidal Fluids: An Integral Equation Study - <i>Jean-Marc Bomont, Dino Costa and Jean-Louis Bretonnet</i>	86 - 97
6	Evolution of Intermetallic Compounds in Ti–Al–Nb System by the Action of Mechanoactivation and Spark Plasma Sintering - <i>Yernat Kozhakhmetov, Mazhyn Skakov, Wojciech Wieleba, Kurbanbekov Sherzod, and Nuriya Mukhamedova</i>	98 - 107
7	Microstructures, Mechanical Properties, and Corrosion behavior of Novel Multi-Component Ti–6Mo–6Nb–xSn–xMn Alloys for Biomedical Applications - <i>Cahya Sutowo, Galih Senopati, Andika W Pramono, Sugeng Supriadi and Bambang Suharno</i>	108 - 116

# Electrospinning Process Control for Fiber - Structured Poly (Bisphenol Aco - Epichlorohydrin) Membrane

Wisawat Keaswejjareansuk<sup>1</sup>, Xiang Wang<sup>2</sup>, Richard D. Sisson<sup>1</sup> and Jianyu Liang<sup>1,\*</sup>

<sup>1</sup>Department of Mechanical Engineering, Worcester Polytechnic Institute, 100 Institute Road, Worcester, MA 01609, USA

<sup>2</sup>School of Materials Science and Technology, Wuhan University of Technology, 122 Luoshi Road, Hubei Province 430070, P. R. China

\* Correspondence: Email: jianyu1@wpi.edu; Tel: +15088316649; Fax: +15088315633.

## ABSTRACT

Porous and fiber structures are utilized to create lightweight materials for many applications. Poly(bisphenol A-co-epichlorohydrin) PBE or phenoxy resin is a widely used thermoplastic resin in thermoplastic, blends, and polymer matrices. In this article, PBE was selected as a model thermoplastic to fabricate a porous membrane with suitable structure and properties through an electrospinning process. The morphology of the electrospun membrane was effectively controlled by adjusting solution concentration and solvent composition and regulating acceleration potential, while keeping the solution feed rate and tip-to-collector distance at specific values. It was observed that the elastic modulus and tensile strength of the obtained porous PBE membranes were dependent on structure and form. With consistent fiber morphology, the research process obtained a relatively high elastic modulus, tensile strength, and density at  $9.125 \pm 2.573$  GPa,  $1.260 \pm 0.195$  Mpa, and  $0.420 \pm 0.056$  g/cm<sup>3</sup>, respectively. Thermal analysis showed insignificant differences in the thermal stability between the electrospun samples and raw materials.

**Keywords:** electrospinning; fiber; poly (bisphenol A-co-epichlorohydrin); porous membrane; thermoplastic; structure property; mechanical property

## 1. INTRODUCTION

Thermoplastic is extensively used in many applications such as consumer products, biomedical materials, chemical sensors, filtration and separation, data storage and transmission, energy materials, and in the manufacturing process [1–4]. In addition to the ease of processing, mechanical performance is an important factor for thermoplastic utilization. Adding fiber materials and forming fiber composite thermoplastics to improve mechanical properties is a widely applied and well documented practice [5–10]. Interestingly, recently it was shown that fiber-structured thermoplastics demonstrated significant improvement in mechanical properties compared with the same material having a non-fiber structure. For example, studies of Alexander and Wanasekara showed that the polypropylene PP fibers had tensile strength as high as 200 MPa [5,6]. Ye demonstrated that the polyethylene PE fibers had tensile strength in a range of 26 MPa–3.3 GPa, depending upon the production process, while non-fiber-structured, injection-molded, high-density polyethylene HDPE had a tensile strength of less than 50 MPa [6].

Electrospinning (ES) is an efficient and versatile process to fabricate highly porous membranes [11]. It is a straightforward technique to create continuous fibers with diameters ranging from nano- to micrometers. In this process, a high electric potential is applied to a spinneret (needle), which is connected to a syringe that holds a polymer solution. The polymer solution is fed by a syringe pump to be

spun in the applied electric field. During the spinning process, the charged polymer solution is elongated to fiber-like jets and then collected on a grounded collector. The ES process has been studied for many applications, such as biomaterials, batteries, capacitors, catalysts, and filtration systems [12–16]. Several thermoplastic materials have been deployed to create various ES membranes. A summary of the ES-thermoplastics, solvent system, and applications are shown in Table 1.

**Table 1. A summary of electrospun thermoplastic materials and their applications.**

Material	Solvent	Fiber diameter ( $\mu\text{m}$ )	Applications
Polyvinylidene difluoride PVdF [17,18]	<i>N,N</i> -dimethylacetamide	0.40–0.51	Battery separator; polymer electrolyte
	DMAc/acetone	0.38	Microfiltration membrane
	<i>N,N</i> -dimethylformamide	0.50	Membrane distillation
Polyacrylonitrile PAN [19]	DMF	0.75	Ultrafiltration membrane
Polyethylene oxide PEO [20]	Water	0.27–0.40	Biomedical applications; solid-polymer electrolyte
Polyvinyl alcohol PVA [21]	Water	0.08–0.24	Biomedical applications; filtration membrane
Polypropylene PP [22]	Decalin	0.80	Battery separator; filtration membrane; protective clothing
PAN/PVA [18]	DMF (PAN); water (PVA)	0.15	Ultrafiltration membrane
Polyamide-6 PA-6 [23]	Formic acid	0.17	Air filtration membrane
Polyimide PI [23]	DMF	0.30	High temperature resistance, air filtration membrane

Poly(bisphenol-A-co-epichlorohydrin) PBE, or phenoxy resin, is a copolymer of bisphenol-A with epichlorohydrin and is a widely-used thermoplastic resin. It is ductile, tough, and miscible with various polymers, due to the presence of a pendant hydroxyl group (proton donor with appropriate functional groups) [24–27]. It has been shown to increase the glass-transition temperature of functional polymer blends, such as in thermal-responsive, shape-memory applications [25–29]. It has been used to increase the tensile strength, elongation, elastic modulus, and flexural strength in Surface micrographs were obtained by a field emission scanning electron microscope (FE-SEM, JEOL 7000F), operated at 2 kV. Average density of the membrane spun with each solution concentration was calculated by the weight and volume of three ES samples with an identical diameter of 7/32 inch (0.56 cm). Mechanical properties were measured by a universal testing machine (UTM, Instron 5567A) with a cross-head speed of 2 mm/min. The samples that were used to perform mechanical property measurements were prepared following the previously reported electrospinning studies [43–46]. Each ES membrane was cut into a strip of 0.25 inches (0.63 cm) width, 1 inch (2.54 cm) length, with 0.5 inches (1.27 cm) gauge-length and approximate 65  $\mu\text{m}$  thickness. Each ES-sample was obtained after 40 min. of electrospinning. After drying, the thickness of the deposition was  $\geq 65 \mu\text{m}$  in the thickest portion. A micrometer was used to measure the thickness at different locations in each sample. The portion that had a thickness of approximately 65  $\mu\text{m}$  was chosen and cut into strips for testing. At least three ES samples were measured for each data point. The samples were also analyzed by thermogravimetric analysis (TGA, TA Instrument Q50) in air, in a temperature range of 35–700  $^{\circ}\text{C}$ , at a heating rate of 10  $^{\circ}\text{C}/\text{min}$ .

### 3. RESULTS AND DISCUSSION

#### 3.1. Solvent composition

The use of the acetone and DMF solvent system in this study was informed by the established understanding of the vapor pressure effect. The boiling point and vapor pressures are 56 °C for acetone vs. 153 °C for DMF, and 30.79 kPa for acetone vs. 0.49 kPa for DMF, at 25 °C, respectively [47,48]. Acetone has a relatively high vapor pressure, at 25 °C. Hence, the acetone evaporated quickly, which was expected to assist in obtaining thin fibers. The DMF, on the other hand, evaporated slowly, which was anticipated to provide flexibility and allow the spun jets to elongate [49–51]. The rheology of the acetone and DMF binary mixture was thoroughly studied [52,53]. Previous research has investigated the effects of vapor pressure, boiling point, and viscosity of the various binary solvents on morphology [49,51,54–57]. As the solution jets were spun in the electric field, the dielectric constant was suspected to be a factor in producing a membrane with the desired morphology. Hence, dielectric constants of the acetone and DMF solvents were provided in this report.

Different acetone:DMF (% v/v) ratios were studied to identify a suitable solvent ratio for consistent fiber structures. It was found that a minimum of 20% DMF was needed to fully dissolve 0.200 g/mL of PBE and form a homogeneous solution. Vapor pressure of the mixed solvent at each acetone:DMF ratio was the summation of the partial vapor pressure of acetone and DMF, and calculated by Eq 1 [58]. The dielectric constant of the solvent changes as a function of the composition. O. Kolling experimentally determined and calculated the dielectric constants of the acetone:DMF system at 25 °C by Eq 2, where  $X_{Acetone}$  is the mole fraction of acetone [59]:

$$p_{vapor,total} = X_{Acetone} \times p_{vapor,acetone} + X_{DMF} \times p_{vapor,DMF} \quad (1)$$

$$\epsilon = 36.69 - 15.99X_{Acetone} \quad (2)$$

**Table 2. Dielectric constant of the mixed solvents at different ratios of acetone:DMF.**

Acetone:DMF % (v/v)	Moles of solvent (mol)		Mole fraction of acetone	Vapor pressure (kPa)	Dielectric constant	Membrane structure
	Acetone	DMF				
80:20	0.103	0.031	0.769	23.779	24.400	Fiber with large diameter distribution
70:30	0.088	0.045	0.660	20.476	26.143	
60:40	0.073	0.059	0.555	17.298	27.820	Fiber with small diameter distribution
50:50	0.060	0.072	0.454	14.237	29.435	Fiber-bead
40:60	0.047	0.084	0.356	11.288	30.992	
30:70	0.034	0.096	0.263	8.444	32.493	Nonporous membrane;
20:80	0.022	0.108	0.172	5.699	33.941	process turned to
10:90	0.011	0.119	0.084	3.050	35.339	electrospray
0:100	0.000	0.129	0.000	0.490	36.690	

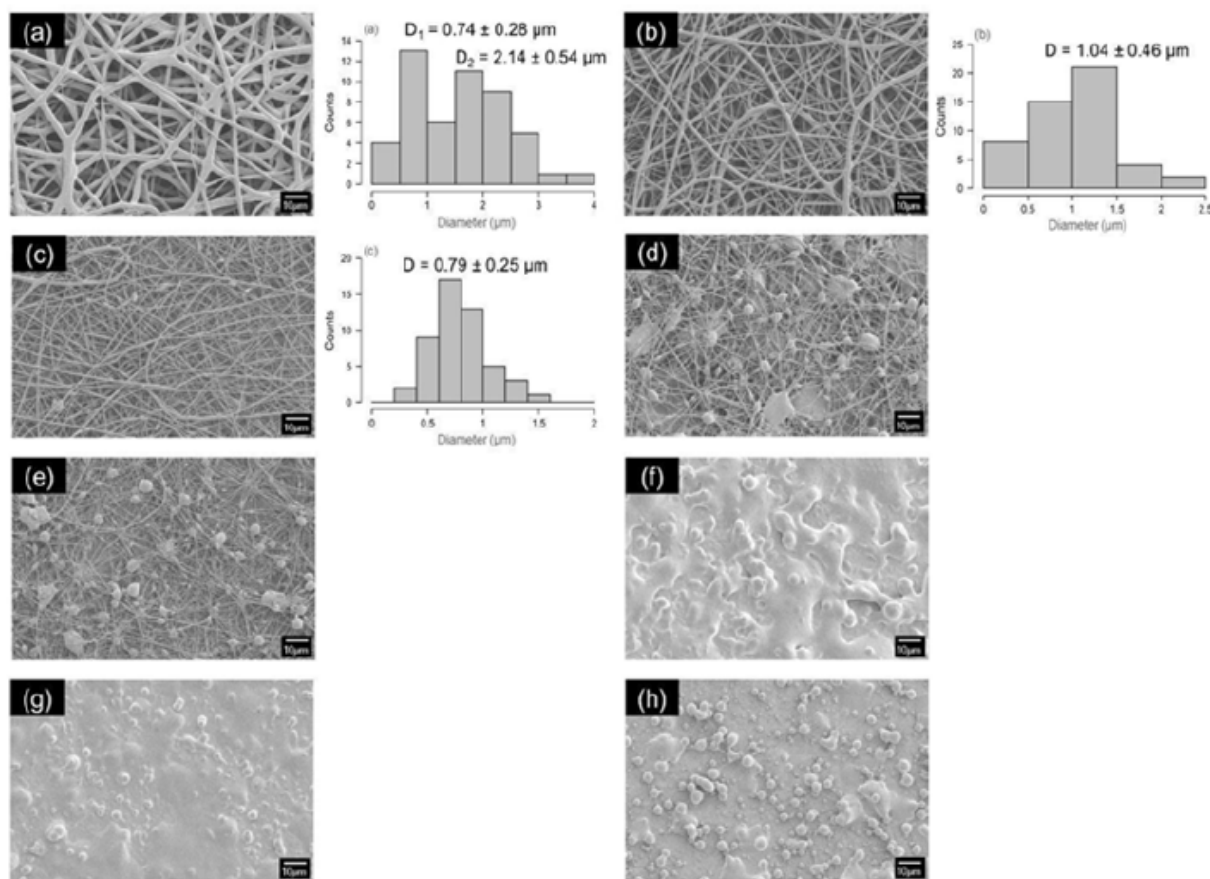


**Figure 1. Effect of solvent composition of acetone:DMF (% , v/v) to morphology of the ES-PBE membrane: (a) 80:20; (b) 70:30; (c) 60:40; (d) 50:50; (e) 40:60; (f) 30:70; (g) 20:80; and (h) 10:90 (700× magnification, scale bar corresponds to 10 μm).**

Using Eq 2, the dielectric constants of the various solvents tested in this study were calculated and are summarized in Table 2. It was observed that a high dielectric constant resulted in a nonporous membrane. Figure 1 shows the typical morphology of ES-PBE membranes with different solvent ratios. Porous structures of the ES-PBE membrane were obtained, with amounts of DMF up to 60% (Figure 1a–c). Fiber structures were obtained up to a dielectric constant ( $\epsilon$  of approximately 28 (Table 2). Although a homogeneous solution can be obtained with pure DMF, acetone is required to control the morphology, because acetone evaporates faster than DMF, and the rapid evaporation is needed to reduce the diameter of the spinning jets prior to being collected on the grounded collector. When the amount of acetone was 40–50% (Figure 1d,e), a mixed fiber-bead structure was obtained. When the amount of acetone was less than 40% (Figure 1f–h), there were no fibers observed, and the membrane became nonporous. A consistently fine fiber structure (Figure 1c) was reliably obtained with an acetone:DMF ratio of 60:40 (% , v/v). Thus, this solvent ratio was selected to be used in future experiments, in order to rule out any variation in solvent composition.

### 3.2. PBE concentration and acceleration potential

The solvent ratio of 60:40 (% , v/v) acetone:DMF was used in experiments with different concentrations and acceleration potentials. Concentrations ranging from 0.125 to 0.250 g/mL were tested under two acceleration potentials, 20 kV and 25 kV. At low concentrations, ranging from 0.125 to 0.175 g/mL (Figure 2a–c and 2a'–c'), a mixed fiber-bead structure was observed with beads dominant at both

acceleration potentials. When the concentrations were increased, this structure gradually transitioned to a fiber-dominant structure. The fiber structure was obtained at concentrations of 0.200–0.250 g/mL (Figure 2d–f and 2d'–f') at both acceleration potentials. At the concentration of 0.200 g/mL, fine and consistent fiber structure was reliably obtained (Figure 2d,d').

At the higher concentration of 0.250 g/mL (Figure 2f,f'), thicker fibers were obtained. At the concentration of 0.125 g/mL, a powder-like deposition was formed on the collector.

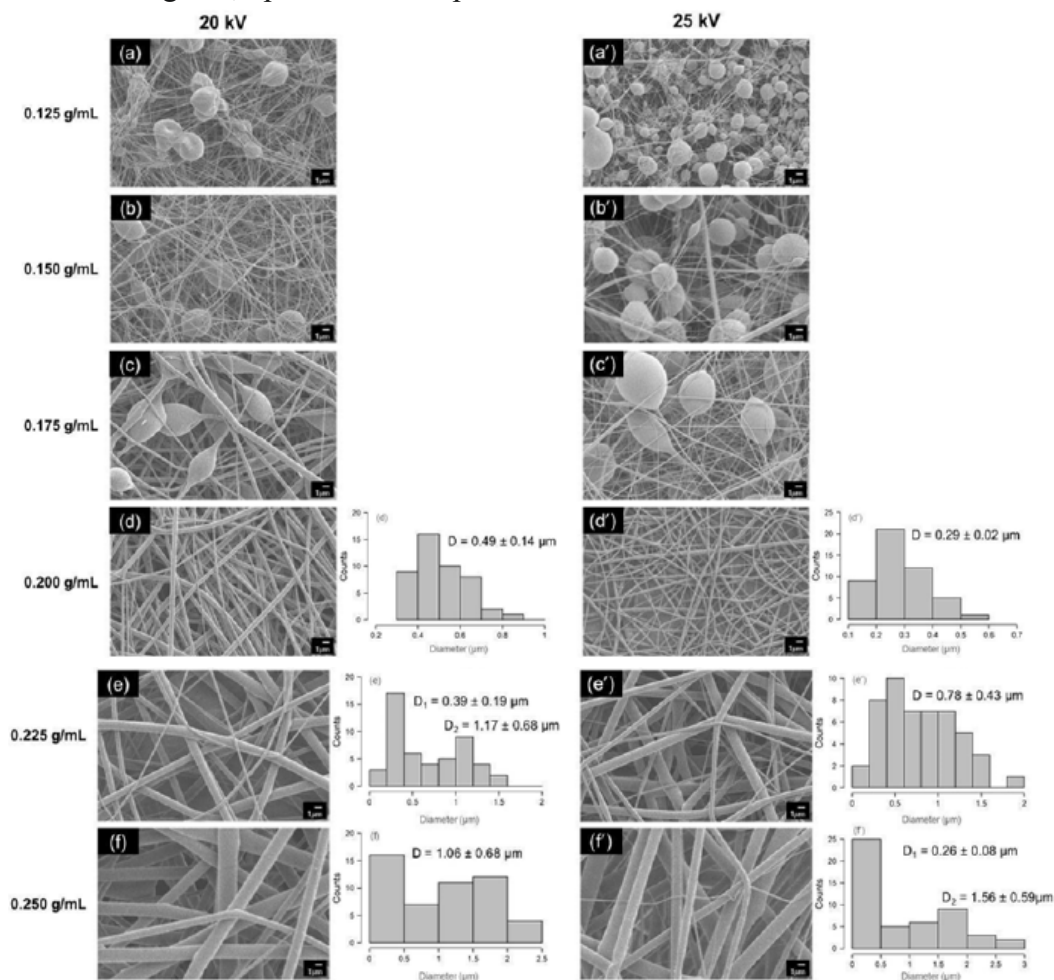


**Figure 2. Effects of the concentration and the acceleration potential at 20 kV (a–f) and 25 kV (a'–f') on the morphology: (a) and (a') 0.125 g/mL; (b) and (b') 0.150 g/mL; (c) and (c') 0.175 g/mL; (d) and (d') 0.200 g/mL; (e) and (e') 0.225 g/mL; (f) and (f') 0.250 g/mL (3000 $\times$  magnification, scale bar corresponds to 1  $\mu$ m).**

It is known that the morphology of the ES membrane may be affected by the acceleration potential. The high acceleration potentials (20 kV and 25 kV) in this study were chosen based on previous studies [21,60,61]. A high-acceleration potential results in a stronger electric field. Hence, the charged solution jets, at high acceleration potential, move faster and produce fibers with a smaller diameter than at the low acceleration potential [61]. The distribution of the fiber diameter (Figure 2d–f and 2d'–f') was measured from 50 different fibers in each SEM figure. The membranes created from the solution concentrations of 0.225 g/mL and 0.250 g/mL had either a wide distribution or showed a bimodal distribution of the fiber diameter. In addition, average fiber diameter expanded with an increase in solution concentration. Similar observations were reported in other studies of electrospun thermoplastics [19,21,61]. The average fiber diameters created from the solution concentration of 0.200 g/mL were  $0.49 \pm 0.14 \mu\text{m}$

(spun at 20 kV, Figure 2d) and  $0.29 \pm 0.02 \mu\text{m}$  (spun at 25 kV, Figure 2d'). An acceleration potential of 20 kV enables better control over the total deposition thickness, due to a slower deposition rate, as compared with that of 25 kV. In this study, 20 kV was used in subsequent experiments.

### 3.3. TGA study of ES-PBE membrane

Figure 3 shows the TGA thermogram of the ES-PBE membranes and pellets. The ES-PBE membranes did not show significant weight change until 370 °C (initial decomposition temperature). Two decomposition steps occurred: the first one at 370–420 °C and the second one between 480–650 °C. This observation is similar to Corres' study on thermal decomposition of the PBE powder under ambient atmosphere [27]. Corres et al.'s study shows that the presence of oxygen in an ambient atmosphere affects the degradation behavior and results in two decomposition steps in air, as opposed to a single decomposition step in a nitrogen environment [27].

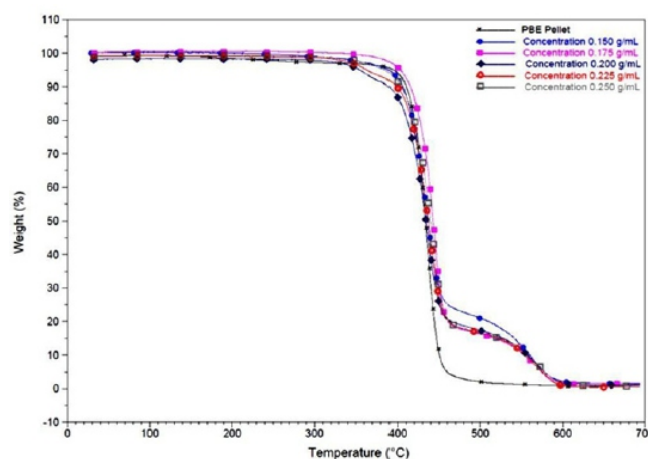


**Figure 3. TGA thermogram illustrating thermal decomposition temperatures (~370 °C) and thermal stability of the ES-PBE membranes.**

The ES-PBE membrane was further examined at temperatures slightly higher than the material's glass-transition temperature  $T_g \sim 108 \text{ °C}$  [42] (Figure 4). Three ES samples, obtained by the same processing conditions (solution concentration = 0.200 g/mL, acceleration potential = 20 kV), were cut into squares of 2 cm (0.78 inch) by 2 cm. The samples were heated in a box furnace, from room temperature to 110 °C (slightly higher than the  $T_g$ ), 115 °C, and 118 °C, then held for 1 h. At 110 °C, a change in the fiber morphology was already noticeable (compared to Figure 2d).

At 118 °C, some fibers were fused together. Even though ES-PBE membranes do not start to decompose until 370 °C, it is probably necessary to set the service temperature lower than the  $T_g$  for applications that demand integrity of the membrane morphology and structure.

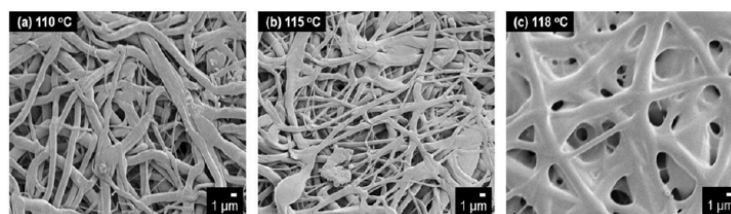


**Figure 4. SEM micrographs demonstrate macroscopic morphology deformation of the ES-PBE membrane (solution concentration = 0.200 g/mL, and acceleration potential = 20 kV) at tested temperatures: (a) 110 °C; (b) 115 °C; and (c) 118 °C (3000 $\times$  magnification, scale bar corresponds to 1  $\mu\text{m}$ ).**

### 3.4. Mechanical property

Elastic modulus and tensile strength of the ES-PBE membranes were measured and listed in Table 3. In comparison to the reported nonporous, cast PBE, the electrospun samples had a similar or higher elastic modulus but exhibited lower tensile strength [63]. The relatively large standard deviation of tensile strength and elastic modulus was typical for the ES fibers deposited on the stationary collector, due to the random depositions. This observation agrees with a previous study by Al-Attabi et al. [64]. Differences in the tensile strength between the electrospun membrane and the raw materials have also been seen in previous electrospinning studies on other thermoplastics, for example, PVdF (1.2–7.5 vs 42–43 MPa) and polyvinyl chloride PVC (0.90 vs 56.6 MPa) [65–68].

As presented in Figure 5, membranes with the mixed fiber-bead structure (solution concentrations <0.200 g/mL) had much lower tensile strength than that of the fiber structure (solution concentration  $\geq$  0.200 g/mL). Although the tensile strength of the fiber-structured membranes was similar, the membranes with a more consistent fiber structure had a higher elastic modulus (Figure 6). It was observed that the membranes produced from a concentration of 0.200 g/mL had the highest elastic modulus and tensile strength among all the samples tested.

**Table 3. Physical and mechanical properties of ES samples, which correspond to different polymer solution concentrations at an acceleration potential of 20 kV.**

Concentration of polymer solution (g/mL)	Membrane structure	Average density (g/cm <sup>3</sup> )	E (GPa)	TS (MPa)
0.150	Fiber-bead	0.345 $\pm$ 0.029	1.129 $\pm$ 0.746	0.135 $\pm$ 0.065
0.175	Fiber-bead	0.263 $\pm$ 0.019	3.322 $\pm$ 0.736	0.294 $\pm$ 0.022
0.200	Consistent fiber	0.420 $\pm$ 0.056	9.125 $\pm$ 2.573	1.260 $\pm$ 0.195
0.225	Inconsistent fiber	0.368 $\pm$ 0.008	2.229 $\pm$ 0.994	1.055 $\pm$ 0.353
0.250	Inconsistent fiber	0.302 $\pm$ 0.005	5.019 $\pm$ 2.309	1.271 $\pm$ 0.112
PBE pellet	-	1.180 [62]	-	-
Cast PBE (thickness = 120 $\mu$ m) [63]	Nonporous	-	1.2 [63]	41 [63]

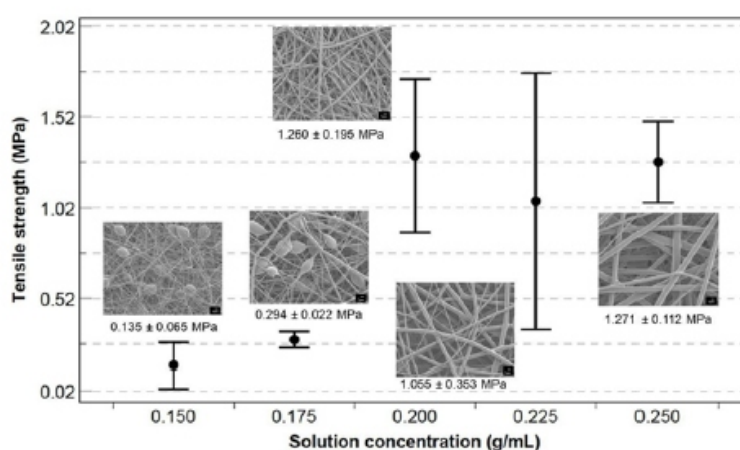


**Figure 5. Tensile strength (MPa) correspondence with the polymer solution concentration (g/mL)**

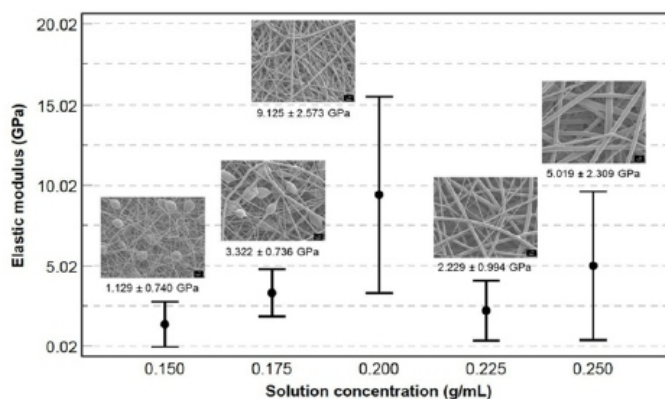


**Figure 6. Elastic modulus (GPa) correspondence with the polymer solution concentration (g/mL).**

#### 4. CONCLUSION

In this report, porous PBE membranes were created by an electrospinning process. The thermal stability of the electrospun samples was confirmed to be similar to that of PBE pellets. In this study, the density, tensile strength, and elastic modulus varied, depending on the membrane morphology. Consistent fiber morphology resulted in high tensile strength and elastic modulus. The concentration of polymer solution, solvent composition, and acceleration potential were important factors influencing membrane morphology. Solvent composition determines the dielectric constant, which affects the spinning rate of the solution jets, and, hence, the membrane morphology. In addition, solvent composition is an important parameter for controlling morphology, due to the boiling point and the vapor pressure of each solvent component. PBE is used as an adhesive, coating agent, additive, and matrix to other functional materials. The porous, non-woven membranes of PBEs, with a high thermal stability similar to that of PBE pellets, may be desirable for applications at elevated temperatures that other ES membranes cannot withstand.

#### Conflict of interests

Authors have declared that no competing interests exist.

#### REFERENCES

- Pang X, Zhuang X, Tang Z, et al. (2010) Polylactic acid (PLA): research, development and industrialization. *Biotechnol J* 5: 1125–1136.
- Abdelrasoul A, Doan H, Lohi A, et al. (2015) Morphology control of polysulfone membranes in filtration processes: a critical review. *ChemBioEng Rev* 2: 22–43.
- Gabor H (2000) Polymer films in sensor applications: A review of present uses and future possibilities. *Sens Rev* 20: 98–105.
- Kang GD, Cao YM (2014) Application and modification of poly(vinylidene fluoride) (PVDF) membranes—A review. *J Memb Sci* 463: 145–165.
- Wanasekara N, Chalivendra V, Calvert P (2011) Sub-micron scale mechanical properties of polypropylene fibers exposed to ultraviolet and thermal degradation. *Polym Degrad Stab* 96: 432–437.
- Alexander JV, Neely JW, Grulke EA (2014) Effect of chemical Functionalization on the mechanical properties of polypropylene hollow fiber membranes. *J Polym Sci Pol Phys* 52: 1366–1373.
- Ye Z, Zhu S, Wang WJ, et al. (2003) Morphological and mechanical properties of nascent polyethylene fibers produced via ethylene extrusion polymerization with a metallocene catalyst supported on MCM-41 particles. *J Polym Sci Pol Phys* 41: 2433–2443.
- Zhang F, Endo T, Qiu W, et al. (2002) Preparation and mechanical properties of composite of fibrous cellulose and maleated polyethylene. *J Appl Polym Sci* 84: 1971–1980.
- Shubhra QTH, Alam AKMM, Quaiyyum MA (2013) Mechanical properties of polypropylene composites: A review. *J Thermoplast Compos* 26: 362–391.
- Bledzki AK, Jaszkievicz A, Scherzer D (2009) Mechanical properties of PLA composites with man-made cellulose and abaca fibres. *Compos Part A-Appl S* 40: 404–412.

11. Reneker DH, Chun I (1996) Nanometre diameter fibres of polymer, produced by electrospinning. *Nanotechnology* 7: 216–223.
12. Yoshimoto H, Shin YM, Terai H, et al. (2003) A biodegradable nanofiber scaffold by electrospinning and its potential for bone tissue engineering. *Biomaterials* 24: 2077–2082.
13. Jung JW, Lee CL, Yu S, et al. (2016) Electrospun nanofibers as a platform for advanced secondary batteries: a comprehensive review. *J Mater Chem A* 4: 703–750.
14. Zhang F, Yuan C, Zhu J, et al. (2013) Flexible films derived from electrospun carbon nanofibers incorporated with Co<sub>3</sub>O<sub>4</sub> hollow nanoparticles as self-supported electrodes for electrochemical capacitors. *Adv Funct Mater* 23: 3909–3915.
15. Formo E, Lee E, Campbell D, et al. (2008) Functionalization of electrospun TiO<sub>2</sub> nanofibers with Pt nanoparticles and nanowires for catalytic applications. *Nano Lett* 8: 668–672.
16. Gopal R, Kaur S, Ma Z, et al. (2006) Electrospun nanofibrous filtration membrane. *J Memb Sci* 281: 581–586.
17. Choi SS, Lee YS, Joo CW, et al. (2004) Electrospun PVDF nanofiber web as polymer electrolyte or separator. *Electrochimica Acta* 50: 339–343.
18. Vanangamudi A, Yang X, Duke MC, et al. (2019) Nanofibers for membrane applications. In: Barhoum A, Bechelany M, Makhoulouf A, *Handbook of Nanofibers*, Springer-Cham, 937–960.
19. Yoon K, Kim K, Wang X, et al. (2006) High flux ultrafiltration membranes based on electrospun nanofibrous PAN scaffolds and chitosan coating. *Polymer* 47: 2434–2441.
20. Deitzel JM, Kleinmeyer JD, Hirvonen JK, et al. (2001) Controlled deposition of electrospun poly(ethylene oxide) fibers. *Polymer* 42: 8163–8170.
21. Zhang C, Yuan X, Wu L, et al. (2005) Study on morphology of electrospun poly(vinyl alcohol) mats. *Eur Polym J* 41: 423–432.
22. Cho D, Zhou H, Cho Y, et al. (2010) Structural properties and superhydrophobicity of electrospun polypropylene fibers from solution and melt. *Polymer* 51: 6005–6012.
23. Al-Attabi R, Morsi YS, Schütz JA, et al. (2018) Electrospun membranes for airborne contaminants capture. In: Barhoum A, Bechelany M, Makhoulouf A, *Handbook of Nanofibers*, Springer-Cham, 1–18.
24. Iriarte MA, Iruin JJ, Eguiazabal JI (1989) Thermal decomposition of miscible phenoxy/ poly(ethylene oxide) blends. *J Mater Sci* 24: 1021–1024.
25. Zhang R, Luo X, Ma D (1995) Miscibility of polyhydroxy ether of bisphenol-A with ethylene terephthalate-caprolactone copolyesters. *Eur Polym J* 31: 1011–1014.
26. Kim BK, Choi CH (1996) Melt blends of poly(methyl methacrylate) with a phenoxy. *Polymer* 37: 807–812.
27. Corres MA, Zubitur M, Cortazar M, et al. (2011) Thermal and thermo-oxidative degradation of poly(hydroxy ether of bisphenol-A) studied by TGA/FTIR and TGA/MS. *J Anal Appl Pyrol* 92: 407–416.
28. Guo Q (1995) Effect of curing agent on the phase behaviour of epoxy resin/phenoxy blends. *Polymer* 36: 4753–4760.
29. Jeong HM, Ahn BK, Kim BK (2001) Miscibility and shape memory effect of thermoplastic polyurethane blends with phenoxy resin. *Eur Polym J* 37: 2245–2252.
30. Yilmaz T, Özarıslan Ö, Yildiz E, et al. (1998) Effects of nonreactive resins on the properties of a UV-curable methacrylated urethane resin. *J Appl Polym Sci* 69: 1837–1845.
31. Qipeng G, Jinyu H, Binyao L, et al. (1991) Blends of phenolphthalein poly(ether ketone) with phenoxy and epoxy resin. *Polymer* 32: 58–65.
32. Choi GD, Kim SH, Jo WH, et al. (1995) The morphology and mechanical properties of phenoxy/ liquid crystalline polymer blends and the effect of transesterification. *J Appl Polym Sci* 55: 561–569.
33. Wu H, Ma CM, Lin J (1997) Processability and properties of phenoxy resin toughened phenolic resin composites. *J Appl Polym Sci* 63: 911–917.
34. Yang BX, Shi JH, Pramoda KP, et al. (2007) Enhancement of stiffness, strength, ductility and toughness of poly(ethylene oxide) using phenoxy-grafted multiwalled carbon nanotubes. *Nanotechnology* 18: 125606.
35. Goh HW, Goh SH, Xu GQ, et al. (2003) Dynamic mechanical behavior of in situ functionalized multi-walled carbon nanotube/phenoxy resin composite. *Chem Phys Lett* 373: 277–83.
36. Ueki T, Nojima K, Asano K, et al. (1998) Toughening of epoxy resin systems for cryogenic use. *Adv Cryog Eng Mater* 44: 277–283.
37. Ueki T, Nishijima S, Izumi Y (2005) Designing of epoxy resin systems for cryogenic use. *Cryogenics* 45: 141–148.
38. Bhat AH, Abdul Khalil HPS, Bhat IUH, et al. (2011) Development and characterization of novel modified red mud nanocomposites based on poly(hydroxy ether) of bisphenol A. *J Appl Polym Sci* 119: 515–522.
39. Yi JW, Lee W, Seong DG, et al. (2016) Effect of phenoxy-based coating resin for reinforcing pitch carbon fibers on the interlaminar shear strength of PA6 composites. *Compos Part A-Appl S* 87: 212–219.

40. Beier U, Sandler JKW, Altstadt V, et al. (2009) Mechanical performance of carbon fibrereinforced composites based on stitched and bindered preforms. *Compos Part A-Appl S* 40: 1756–1763.
41. Beier U, Wolff-Fabris F, Fischer F, et al. (2008) Mechanical performance of carbon fibrereinforced composites based on preforms stitched with innovative low-melting temperature and matrix soluble thermoplastic yarns. *Compos Part A-Appl S* 39: 1572–1581.
42. Chemical Retrieval on the Web (CROW), Polymer properties database: epoxy or phenoxy resin, 2018. Available from: <https://polymerdatabase.com/polymers/bisphenoladiglycidyletherepoxyresin.html>.
43. Lee SG, Han KS, Joo CW, et al. (2004) Electrospun PVDF nanofiber web as polymer electrolyte or separator. *Electrochim Acta* 50: 339–343.
44. Hao J, Lei G, Li Z, et al. (2013) A novel polyethylene terephthalate nonwoven separator based on electrospinning technique for lithium ion battery. *J Memb Sci* 428: 11–16.
45. Zhang J, Liu Z, Kong Q, et al. (2013) Renewable and superior thermal-resistant cellulose-based composite nonwoven as lithium-ion battery separator. *ACS Appl Mater Inter* 5: 128–134.
46. Yanilmaz M, Dirican M, Zhang X (2018) Evaluation of electrospun SiO<sub>2</sub>/nylon 6,6 nanofiber membranes as a thermally-stable separator for lithium-ion batteries. *Electrochim Acta* 133: 501–508.
47. U.S. National Library of Medicine, Acetone, 2004. Available from: <https://pubchem.ncbi.nlm.nih.gov/compound/180>.
48. U.S. National Library of Medicine, N,N-Dimethylformamide, 2004. Available from: <https://pubchem.ncbi.nlm.nih.gov/compound/6228>.
49. Thompson CJ, Chase GG, Yurin AL, et al. (2007) Effects of parameters on nanofiber diameter determined from electrospinning model. *Polymers* 48: 6913–6922.
50. Shawon J, Sung C (2004) Electrospinning of polycarbonate nanofibers with solvent mixtures THF and DMF. *J Mater Sci* 39: 4605–4613.
51. Lin J, Ding B, Yu J, et al. (2010) Direct fabrication of highly nanoporous polystyrene fibers via electrospinning. *ACS Appl Mater Inter* 2: 521–528.
52. Gill DS, Sherma AN (1982) Acetone + NN-Dimethylformamide solvent system. Part 2— Conductance studies of some electrolytes in Acetone + NN-Dimethylformamide mixtures at 25 °C. *J Chem Soc Faraday Trans* 78: 465–474.
53. Gill DS, Schneider H (1980) Acetone–N,N–dimethylformamide solvent system. Part 1— properties of Acetone–N,N–dimethylformamide binary mixtures. *Indian J Chem* 19A: 313–316.
54. Yoon K, Hsiao BS, Chu B (2009) Formation of functional polyethersulfone electrospun membrane for water purification by mixed solvent and oxidation process. *Polymer* 50: 2893–2899.
55. Qian YF, Su Y, Li XQ, et al. (2010) Electrospinning of polymethyl methacrylate nanofibers in different solvents. *Irian Polym J* 19: 123–129.
56. Katsogiannis KAG, Vladislavljevic GT, Georgiadou S (2015) Porous electrospun polycaprolactone (PCL) fibres by phase separation. *Eur Polym J* 69: 284–295.
57. Casasola R, Thomas NL, Trybala A, et al. (2014) Electrospun poly lactic acid (PLA) fibres: effect of different solvent systems on fibre morphology and diameter. *Polymer* 55: 4728–4737.
58. Kugel RW (1998) Raoult's law: binary liquid-vapor phase diagrams, a simple physical chemistry experiment. *J Chem Educ* 75: 1125–1129.
59. Kolling OW (1993) Dielectric characterization of cosolvents containing N,N– dimethylformamide. *Trans Kansas Acad Sci* 97: 88.
60. Ligneris E, Dumeé LF, Al-Attabi R, et al. (2019) Mixed matrix poly(vinyl alcohol)-copper nanofibrous anti-microbial air-microfilters. *Membranes* 9: 87–100.
61. Jacobs V, Anandjiwala RD, Maaza M (2010) The influence of electrospinning parameters on the structural morphology and diameter of electrospun nanofibers. *J Appl Polym Sci* 115: 3130–3136.
62. Sigma-Aldrich, Poly(bisphenol A-co-epichlorohydrin), 2019. Available at: <https://www.sigmaaldrich.com/catalog/product/aldrich/181196>.
63. Sainsbury T, Gnaniah S, Spencer SJ, et al. (2017) Extreme mechanical reinforcement in graphene oxide based thin-film nanocomposites via covalently tailored nanofiller matrix compatibilization. *Carbon* 114: 367–376.
64. Al-Attabi R, Dumeé LF, Schutz JA, et al. (2018) Pore engineering towards highly efficient electrospun nanofibers membranes for aerosol particle removal. *Sci Total Environ* 625: 706–715.
65. Mark JE (2009). *Polymer Data Handbook*, 2 Eds., New York: Oxford University Press, 190: 1170.
66. Kim YJ, Ahn CH, Lee MB, et al. (2011) Characteristics of electrospun PVDF/SiO<sub>2</sub> composite nanofiber membranes as polymer electrolyte. *Mater Chem Phys* 127: 137–142.
67. Yang K, Ma X, Chen F, et al. (2017) Preparation and characterization of gel polymer electrolyte based on electrospun polyhedral oligomeric silsesquioxane-poly(methyl methacrylate) 8/polyvinylidene fluoride hybrid nanofiber membranes for lithium-ion batteries. *J Solid State Electrochem* 22: 581–590.
68. Lee KH, Kim HY, Ryu YJ, et al. (2003) Mechanical behavior of electrospun fiber mats of poly(vinyl chloride)/polyurethane polyblends. *J Polym Sci Pol Phys* 41: 1256–1262.

# Hydrogen Generation Performance of Al–20at%Ca Alloy Synthesized by Mechanical Alloying

A. G. Hernández-Torres<sup>1</sup>, J. L. López-Miranda<sup>2</sup>, I. Santos-Ramos<sup>3</sup> and G. Rosas<sup>3,\*</sup>

<sup>1</sup>Facultad de Química, UNAM circuito exterior, Ciudad Universitaria, 04510, México, D.F.

<sup>2</sup>Centro de Física Aplicada y Tecnología Avanzada, UNAM, Boulevard Juriquilla 3001, Santiago de Querétaro, QRO,76230, México

<sup>3</sup>Instituto de Investigaciones en Metalurgia y Materiales, UMSNH, edificio U, ciudad universitaria, C.P. 58060, Morelia, Michoacán, México

\* Correspondence: Email: grtrejo@yahoo07.com.mx, grtrejo@umich.mx.

## ABSTRACT

*In this study, the Al–20at%Ca alloy was synthesized by mechanical alloy from the elemental powder mixture. Subsequently, the alloy particles were reacted at room temperature to determine the amount of hydrogen released. For these purposes, the powders reacted with different types of water, such as distilled water, tap water, and seawater, and also in the presence of NaCl and CaO additives. Both milled samples and reaction powders were analyzed by X-ray diffraction (XRD), scanning electron microscopy (SEM), transmission electron microscopy (TEM), FT-IR, and Raman spectroscopy (RS). The XRD patterns of the powders prepared show a nanocrystalline alloy consisting of a solid-cubic solution of Al and the tetragonal intermetallic phase CaAl<sub>4</sub>. Studies of XRD and SEM, as well as direct measurements of H<sub>2</sub>, indicated that the best results of H<sub>2</sub> generation were obtained when the alloy reacts with distilled water. Both NaCl and CaO additives improve hydrogen generation, reaching 100% efficiency in distilled water and seawater, and without induction time. Samples with a combination of NaCl and distilled water showed the best reaction times to generate the entire theoretical amount of hydrogen. The XRD and DSC–TGA standards also confirmed the presence of bayerite Al(OH)<sub>3</sub> as a secondary reaction product.*

**Keywords:** hydrogen generation; intermetallic; nanostructured materials; mechanical alloying; microstructure; X-ray diffraction; scanning electron microscopy

## 1. INTRODUCTION

Hydrogen element is an essential fuel for potential use in clean and emission-free transport applications [1,2]. One of the main challenges of hydrogen technologies is its storage capacity [3–5].

However, an alternative to hydrogen storage is the in-situ H<sub>2</sub> generation and feeding on-demand in a hydrogen fuel cell. In this context, aluminum and its alloys have been extensively investigated as useful materials for its reaction with water to release hydrogen [6–8]. Elemental aluminum has difficulty reacting at room temperature with water due to the formation of a passive layer of aluminum oxide [9]. Therefore, to improve the efficiency of the hydrogen reaction, catalytic substances are required that influence the reaction rate by the passive layer elimination. In this sense, several additives such as NaOH [10], KOH [11], NaCl [12], among others [13–14], have been successfully tested. Recently the aluminum has been combining with carbon [12,15] and oxides [16].

Another way to improve the Al reaction with water has been its alloy with Ga and adding several low-melting-point elements such as In, Sn, Zn, and Bi obtaining excellent reaction efficiencies [17]. Also, elements such as Mg, Fe, Co, Ni, have been explored [18–21]. These alloys have carried out by the continuous casting method. However, some elements increase the production cost of the material.

Moreover, in some investigations for the reaction to occur, the temperature must rise [18,22]. Other evaluated production methods include biological and electrochemical processes [23]. However, the biological processes have relatively low efficiency, and the electrochemical methods have a high production cost [24,25].

Alloy and mechanical activation of Al with various elements have also been a successful alternative [26–28]. Mechanical milling is a simple and relatively low-cost method that produces nanocrystalline powder alloys [29]. During the ball milling process, a large number of crystalline defects such as vacancies and dislocations are generated that accumulate a large amount of energy and increase internal stresses in the material. Nanocrystals in the material increase the grain surface area, thus raising the area available for the reaction, that, in addition to the accumulated energy, are structural characteristics that favor the diffusion and reactivity of the chemical species. The effect of increasing surface area on Al's reaction with water was reported in the past. For example, nanoaluminum particles reacted completely to produce bayerite at low temperatures, while microparticles did not [30]. In all cases, the reaction for the hydrogen generation is carried out in three steps: induction time, rapid generation, and passivation. The induction time is the period in which the reaction begins, from the moment the reagents come into contact until the first hydrogen bubble appears [21]. An objective of the new technologies for hydrogen generation is to find the right conditions (maybe room temperature) and appropriated materials so that the induction time was zero or almost zero.

On the other hand, Al-based intermetallic compounds are of our interest because of the hydrogen environmental fracture that affects them [31]. In this process, the Al of the intermetallic compound reacts spontaneously with the water vapor in the air, causing to release of hydrogen. Then, hydrogen releasing causes cleavage fracture of the material increases the surface area, improving the conditions for the reaction of the intermetallic compound with water. Thus, Al-based intermetallic compounds must be explored for these purposes. Thus, in this study, we present the results obtained from the reaction of the Al-based alloy (Al–20at%Ca) with different types of water and in the presence of NaCl and CaO additives. The alloy mixture was obtained by high-energy ball milling in a two-phase region consisting of a solid solution of aluminum, Al[Ca], and the intermetallic phase CaAl<sub>4</sub>, according to the equilibrium phase diagram.

## 2. MATERIALS AND METHODS

### 2.1. Materials

In the present work: Al powder (99.5% purity), Ca powder (99.5% purity), NaCl (99.0% purity), and CaO (96% purity) supplied from Alpha Aesar are used as starting materials.

### 2.2. Alloy preparation

A binary alloy with a nominal composition of Al–20at%Ca was prepared by high-energy ball milling starting from elemental powders. In a container of hardened steel were loaded 3 g of elemental powders and two hardened stainless-steel balls (8.4 g) to give a ball-to-powder mass ratio of 2:8. To form a nanocrystalline alloy, Al and Ca powders were subject to high-energy ball milling in a SPEX 8000 M mill/mixer for 3, 6, and 9 h. During operation, an Ar atmosphere was used to avoid the oxidation of the powders. Then, the alloy particles were exposed to their reaction with different types of water: distilled water, tap water, and seawater. CaO and NaCl additives (10 wt%) were used to improve the response of the synthesized powders with different types of water. A ballmilling process was conducted for 30 min to homogenize the as-synthesized alloy with the additives.

### 2.3. Hydrogen generation properties measurements

During the reaction of the powders and water, the amount of hydrogen released was measured by the method described previously in [21] with minor modifications. Al–20at%Ca alloy particles reacted with different types of water (tap water, natural seawater, or distilled water) inside a 100 ml Kitasato flask. The hydrogen produced by this reaction was taken to a 250 mL distillation flask, inverted and filled with water. This container also served as a water trap for temperature rise during the reaction. The last paragraph constituted the experimental modification with respect to [21]. Water evacuated by hydrogen bubbles in the distillation flask was captured in a 250 mL burette. In each experimental sample, the mass of the Al element contained in the alloy was equivalent to producing 250 mL of H<sub>2</sub> under standard conditions (298 K and 1 atm) with excess water. The formation of the first bubble inside the distillation flask indicates the initial time for H<sub>2</sub> generation. At the end of each experiment, the volume change of the inverted burette was measured to determine the amount of hydrogen released. In addition, the induction time, generation time and total amount of hydrogen released were recorded.

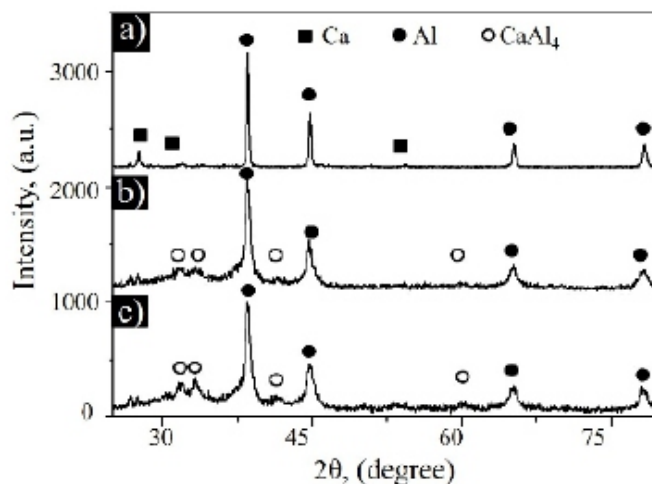
### 2.4. Microstructural characterization

In addition to direct measurements of H<sub>2</sub> release, evidence of the reaction between Al and water can be observed through morphological and chemical changes in the powders after the reaction.

Microstructural characterization of particles with and without additives was performed by X-ray diffraction (XRD, Siemens D5000 X-ray diffractometer) and scanning electron microscopy (SEM, JEOL JSM 2400). In addition, energy dispersive spectroscopy (EDS) analysis was performed on all milled samples to determine their chemical composition. Differential scanning calorimetry analysis (DSC) and thermogravimetric analysis (TGA) was performed using a TA Instruments SDT Q600.

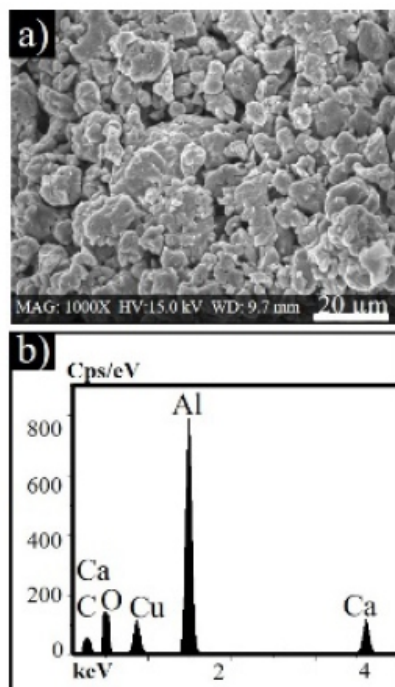
## 3. RESULTS AND DISCUSSION

Figure 1a displays the XRD pattern of the un-milled sample, which contains only the typical diffraction peaks of the Al and Ca. Figure 1b,c shows the XRD patterns of as-milled (Al, Ca) powders after 6 h, and 9 h, respectively. These powders were used in this work for hydrogen generation. The diffraction peaks identified in both XRD patterns confirmed the formation of both Al[Ca] cubic solid solution and the CaAl<sub>4</sub> tetragonal intermetallic phase after 6 h of mechanical milling. The observed phases in the XRD patterns are in good agreement with the Al–Ca phase diagram for the nominal alloy composition used in this work. The crystal size calculated using the Debye–Sherrer equation from the Al (111) crystallographic plane (FWHM) was 17 nm, which confirms the formation of a nanocrystalline alloy [32,33]. According to the Miedema model, the enthalpy of formation for the Al–20at%Ca is negative (–8.65 kJ/mol), which indicates that a mechanical alloy process can form the CaAl<sub>4</sub> phase. A negative enthalpy of formation induces a significant driving force and nucleation due to the relatively simple crystalline structure. The dissolution of Ca in Al is due to crystalline defects induced by milling. All these defects provide the highest percentage of solubility of the solute element in the structure of Al. These defects may include vacancies, dislocations, and grain boundaries, which also participate in the activation of the powders for their reaction with water. On the other hand, ball milling of the additives with the alloyed powders intends to induce a higher number of active sites for their reaction with water.



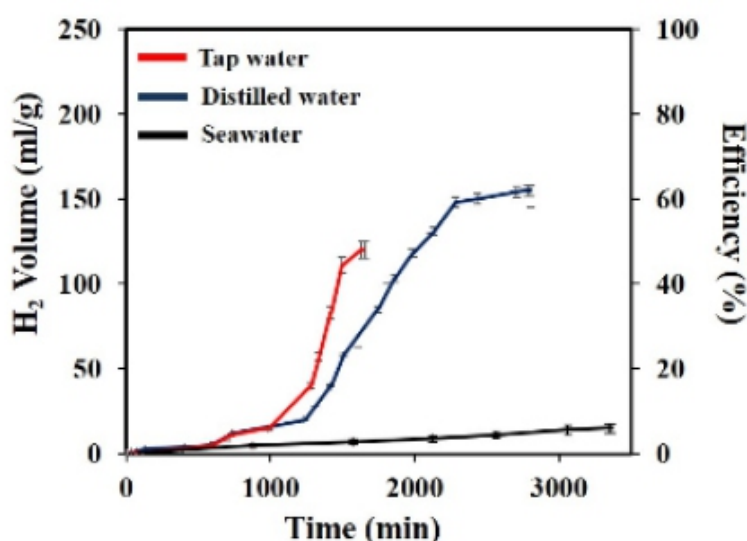
**Figure 1. (a) XRD pattern of the un-milled sample with diffraction peaks of the starting powders (Al, Ca). XRD patterns of as-milled powders after (b) 6 h and, (c) 9 h.**

Figure 2a shows an SEM micrograph illustrating the morphological characteristics of the powders milled for 6 h. The sample exhibits a relatively narrow particle size distribution. The agglomerates observed were formed as a result of these steps: plastic deformation, welding, and fracture that repeatedly occurred in the particles during the ball-milling process. Figure 2b shows the EDS chemical analysis of the sample, indicating the presence of signals of Al, Ca and small amounts of O. The O presence is attributed to the slight oxidation on the particle surface of both metals being approximately 0.5 wt% [34].



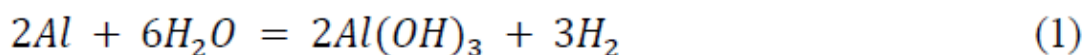
**Figure 2. (a) SEM micrograph of the powders after 6 h high-energy ball milling, (b) EDS analysis of the same particles showing the chemical composition.**

Figure 3 shows the curves of hydrogen generation of the Al–20at%Ca powder as a function of processing time in the different water types. From the graph, we can notice that the use of distilled water indicates the best results for hydrogen generation, followed by the use of tap water and seawater. Similar results were obtained by Wang et al. [35], getting better results in distilled water in comparison with deionized water and tap water. On the contrary, Gai et al. [36] find that the Al reaction with tap water and deionized water is faster than distilled water and seawater. Mag et al. [37] obtained 10% more hydrogen production with seawater, compared with deionized water attribute to the enriched chlorine ions, which accelerate the dissolution reaction of the passivation layer on the Al surface. However, in general, the results of hydrogen generation after the reaction of Al with only different types of water are low; that is why over the years, several additives have used for the reaction activation. In addition, the physicochemical properties of seawater are different from the tap or distilled water. Properties such as density, viscosity, and bacterial content, can make the chemistry of seawater complex, so its reaction to generate hydrogen is also.



**Figure 3. Hydrogen generation of as-milled powders after its reaction under different water types.**

XRD analyses were carried out to know the by-products derived from the hydrogen generation reaction between the milled powders and the different types of water. Figure 4 shows the X-ray diffraction patterns to confirm the existence of reaction products as a result of the generation of hydrogen with the use of the intermetallic phase as an internal additive and different types of water. Figure 4a shows the X-ray diffraction pattern of the powders after their reaction with distilled water. The analysis of this pattern shows the absence of the CaAl<sub>4</sub> intermetallic phase. These findings reveal that the intermetallic phase reacts entirely with water. Therefore, the intermetallic compound decomposes, functioning as an additive in the material. As mentioned earlier, intermetallic materials react spontaneously with water vapor in the air to produce ambient hydrogen [38]. As appreciated, there are small amounts of the starting phase Al[Ca] in the XRD pattern indicating partial reaction with distilled water to produce hydrogen. These results are in good agreement with the results of direct H<sub>2</sub> generation measurements. Additionally, diffraction peaks of the compounds derived from the reaction such as aluminum hydroxide (Al(OH)<sub>3</sub>) with the monoclinic phase and also cubic calcium carbonate (CaCO<sub>3</sub>) were identified. Al(OH)<sub>3</sub> compound (bayerite) appears according to the chemical Eq 1 [39].



where, either Al of the solid solution Al[Ca] or from the intermetallic compound CaAl<sub>4</sub> react with distilled water releasing hydrogen to form bayerite compound. On the other hand, the observed CaCO<sub>3</sub> is due to CaO reaction with CO<sub>2</sub> environmental, according to the chemical Eq 2 [40,41].



Figure 4b shows the XRD pattern of the reacted particles in contact with tap water. The diffraction peaks of the same compounds observed in the as-milled alloy (Al[Ca] cubic and CaAl<sub>4</sub>) were identified. The presence of the starting phases indicates a reduced efficiency of reaction with tap water, which agrees well with the results of the direct measurements of H<sub>2</sub>. These results could be due to the presence of several ions dissociated in tap water. This outcome leads to a lower number of hydroxyl ions and neutral values of pH and affects their reaction with the alloy mixture [20].

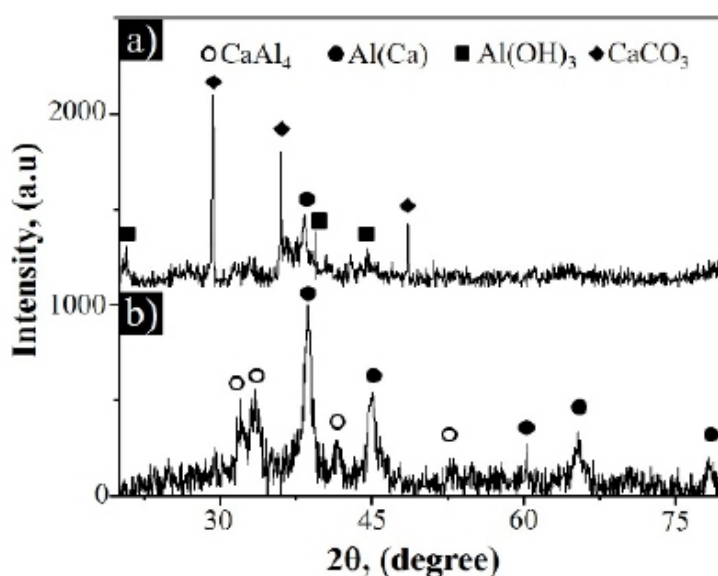


**Figure 4. XRD patterns of the reactant particles in contact with (a) distilled water and, (b) tap water.**

Figure 5 shows the graph of the amount of hydrogen released in the Al–20at%Ca alloy reacting with distilled water and seawater using NaCl and CaO, respectively. It is observed from the curve that the total theoretical yield of hydrogen according to the mass used in these experiments (250 mL) was achieved with the NaCl additive and by using distilled water. Furthermore, the induction time was 0 s, and a higher rate of reaction was obtained in the comparison to the use of seawater + CaO mixture. These findings are comparable to those achieved by using extreme experimental conditions, such as the use of toxic substances as NaOH, KOH or temperature [10–11,18,42].

The sodium chloride salt is highly soluble in water and activates the corrosion of aluminum by promoting the mobility of ions and the transfer of electrical charges [42]. Seawater itself contains NaCl. However, it has been reported that the corrosion process improves when NaCl is milled with the powders before the reaction occurs, leading to a small particle size distribution. Also, when NaCl has increased, the response of the particles to the reaction with water increases [43].

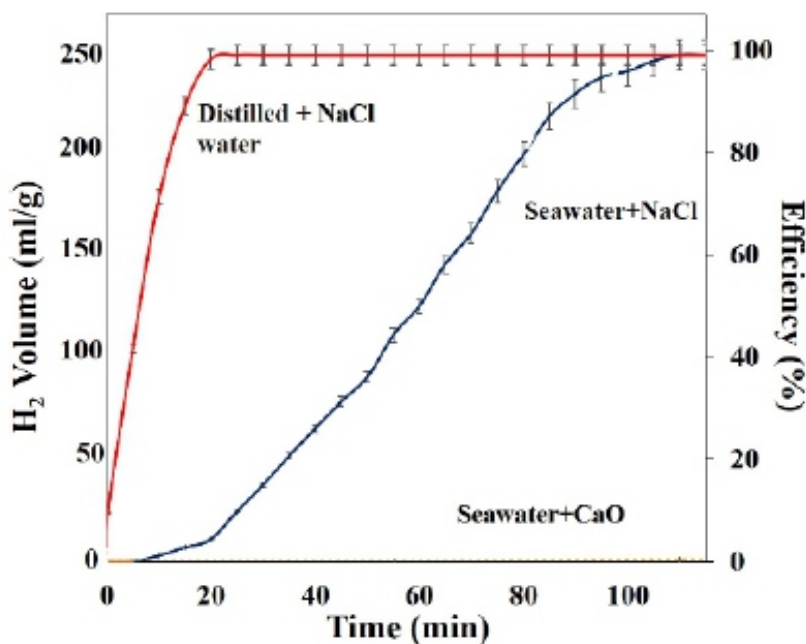


**Figure 5.** Graph showing the amount of hydrogen released from the Al-20at%Ca alloy reacting with distilled water and seawater with the use of NaCl and CaO additives.

Figures 6 show the XRD patterns of the reaction powders in contact with seawater or distilled water and with the addition of NaCl, respectively. In both XRD patterns, some evidence of the starting materials (i.e., Al[Ca] and CaAl<sub>4</sub>) was not displayed. These results indicate their complete reaction with water to produce H<sub>2</sub>. From the patterns, the presence of the monoclinic phase Al(OH)<sub>3</sub> was also determined, which means that the starting materials react to produce hydrogen with water according to the chemical Eq 1. Moreover, XRD peaks of the NaCl and CaCO<sub>3</sub> compounds were also identified. NaCl appears when the sample is dried for its structural characterization. The milled powders are activated for the hydrogen generation reaction due to the crystal size reduction and the increment in internal stresses. Thus, the presence of NaCl additions is useful for obtaining better H<sub>2</sub> generation in the Al-20at%Ca alloy. The hydrogen generation resulting from seawater is a surprising result. It should be considered that in seawater, there is a slight reduction of the OH and H ions, which are occupied by the solvation of metallic salts dissolved in the seawater (3.5 g/L) as compared to the distilled water. In addition, seawater has a higher density, viscosity, and contains organic matter compared to distilled water. These differences in the physicochemical properties of water may also be responsible for the delayed rate of hydrogen generation in seawater. The last can be seen as if there was more water available in distilled water than in the seawater for the reaction with the powders and H<sub>2</sub> generation. On the other hand, the amounts of ions dissolved in the seawater could be acting as agents of charge mobility that, in some way, aids in the process chemistry of hydrogen generation. Obviously, from the commercial point of view, the best result obtained in this work was those achieved with seawater and NaCl additive.

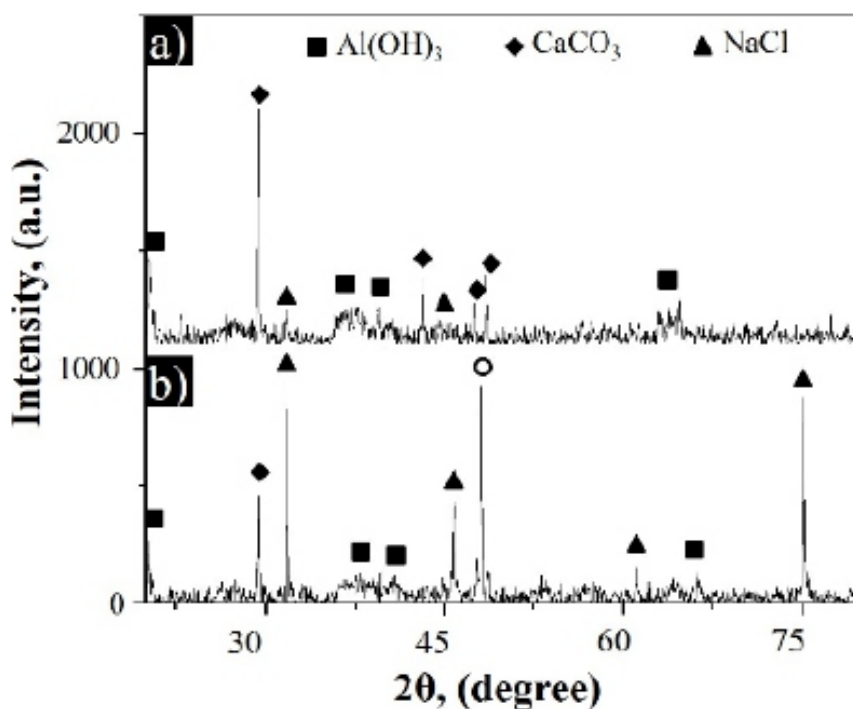


**Figure 6. XRD patterns of the Al–20at%Ca reaction powders with the addition of NaCl in contact with (a) seawater and, (b) distilled water.**

Figures 7a,b show the SEM powders morphology and their corresponding EDS analysis spectra after their reaction with distilled water and seawater and in the presence of NaCl, respectively. As can be seen from micrographs, the agglomerates show signs of reaction on their surface, for example, roughness, in addition to a smaller particle size in comparison with the starting material (Figure 2).

EDS chemical analysis performed on the samples in the case of deionized water (Figure 7c) shows only the alloy elements (i.e., Al and Ca) with the presence of high oxygen counts attribute to the reaction by-products ( $\text{Al(OH)}_3$ ). EDS spectrum of the sample reacted with seawater (Figure 7d), shows elements from the seawater ions (S, Cl, Na, and Mg) and the alloy (Al and Ca). Furthermore, there are also high oxygen counts that can be related to the formation of the  $\text{Al(OH)}_3$  compound. The presence of the  $\text{Al(OH)}_3$  compound is directly related to  $\text{H}_2$  generation, as previously determined by the XRD patterns.

In the past, reports that the intermetallic materials react spontaneously with water to release hydrogen [21]. The hydrogen generated reduces cohesive forces in the solid to provoke cleavage fracture [31]. In this way, the reduction in particle sizes due to the hydrogen fracturing exposes a new surface area to the reaction with water, improving hydrogen generation. That is, the same intermetallic material is acting as an additive within the material.

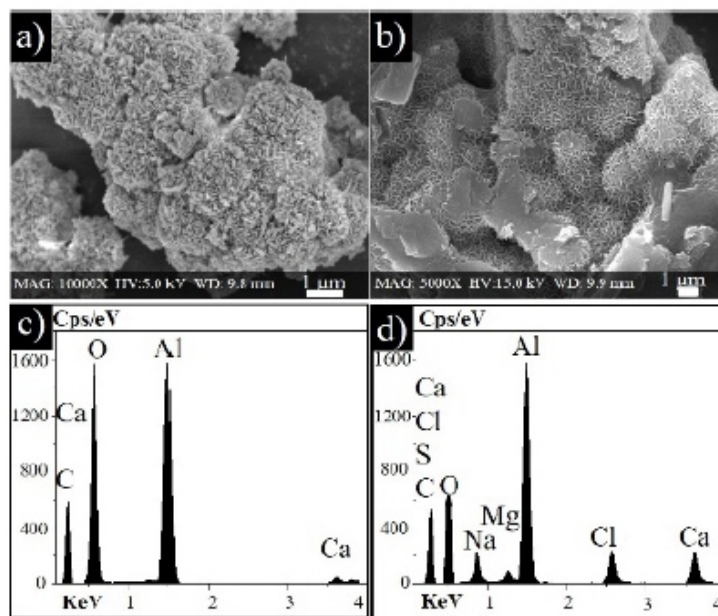


**Figure 7.** SEM micrographs of the Al–20at%Ca reaction powders with the addition of NaCl in contact with (a) distilled water and (b) seawater, (c) and (d) their corresponding EDS analysis.

DSC and TGA experiments obtained after the reaction of the powder with distilled water and seawater and in the presence of NaCl, respectively, are shown in Figures 8a,b. As observed in both curves, an endothermic peak situated around 294 °C corresponding to the dehydration of bayerite appear [44] according to the Eq 3. The integrated area of the peak is more prominent in the sample with distilled water than in the seawater that is in good agreement with the results of the direct measurement of H<sub>2</sub>.

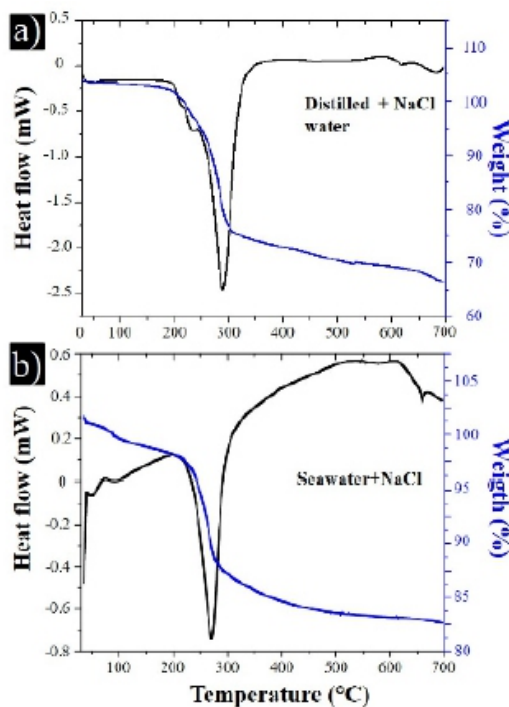
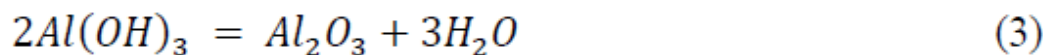


**Figure 8.** DSC–TGA analysis of the powders after reacting using NaCl and different types of water (a) distilled water, and (b) seawater.

Figure 9 shows the micro-Raman spectra for the resulting sample obtained from the reaction of Al–Ca with distilled water using the additive NaCl. The spectrum indicates the presence of bayerite phase,  $\text{Al}(\text{OH})_3$ , and  $\text{CaCO}_3$ . The presence of  $\text{Al}(\text{OH})_3$  in the Raman spectra appears as a solid byproduct during the powder's alloy reaction with water.

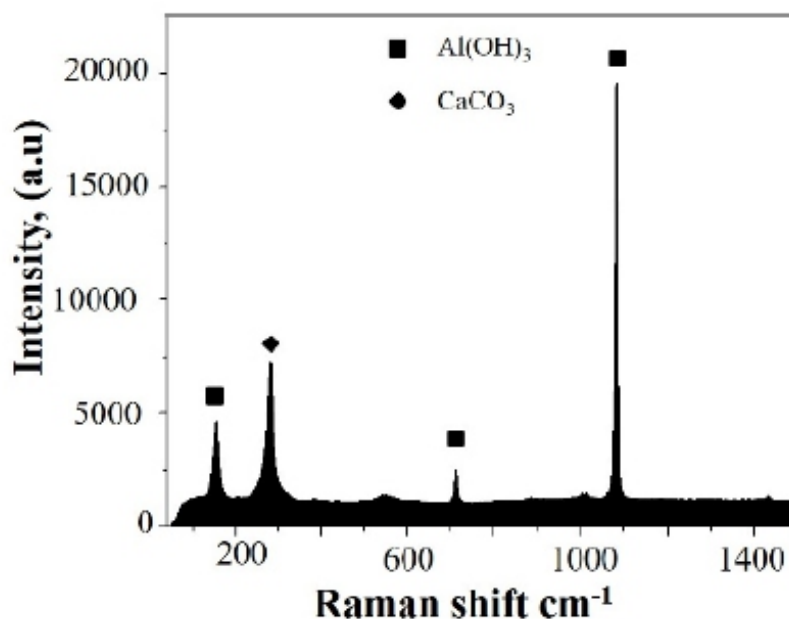


**Figure 9.** Raman spectrum of the reacting particles with distilled water using NaCl as additive.

#### 4. CONCLUSIONS

In summary, in this investigation, the Al–20at%Ca alloy prepared by high-energy ball milling was evaluated as hydrogen generation material. XRD and SEM studies, as well as direct measurements of  $\text{H}_2$ , indicate that the use of distilled water was better than seawater and tap water.

NaCl additions to the intermetallic character alloy improve hydrogen generation in distilled water, reaching 100% efficiency and registering zero induction time. The hydrogen generation from the alloy was not as flattering in samples with the use of seawater and NaCl additive. X-ray diffraction shows that the  $\text{Al}(\text{OH})_3$  compound was the main byproduct of aluminum corrosion.

#### Acknowledgements

The authors want to thank for financial support from Consejo Nacional de Ciencia y Tecnología (CONACYT, México). In special for the Doctoral project to A.G. Hernandez-Torres (CVU 335904) is gratefully acknowledged.

#### Conflict of interests

All authors declare no conflicts of interest in this paper.

#### REFERENCES

1. Chi J, Yu H (2018) Water electrolysis based on renewable energy for hydrogen production. *Chinese J Catal* 39: 390–394.
2. Boran A, Erkan S, Eroglu I (2018) Hydrogen generation from solid state  $\text{NaBH}_4$  by using  $\text{FeCl}_3$  catalyst for portable proton exchange membrane fuel cell applications. *Int J Hydrogen Energ* 44: 18915–18926.
3. Zhang F, Zhao P, Niu M, et al. (2016) The survey of key technologies in hydrogen energy storage. *Int J Hydrogen Energ* 41: 14535–14552.

4. Ancona MA, Antonioni G, Branchini L, et al. (2016) Renewable energy storage system based on a power-to-gas conversion process. *Energ Procedia* 101: 854–861.
5. Kotowicz J, Bartela Ł, Węcel D, et al. (2017) Hydrogen generator characteristics for storage of renewably-generated energy. *Energy* 118: 156–171.
6. Czech E, Troczynski T (2010) Hydrogen generation through massive corrosion of deformed aluminum in water. *International journal of hydrogen energy. Int J Hydrogen Energ* 35: 1029–1037.
7. Soler L, Macanás J, Muñoz M, et al. (2007) Synergistic hydrogen generation from aluminum, aluminum alloys and sodium borohydride in aqueous solutions. *Int J Hydrogen Energ* 32: 4702–4710.
8. Mahmoodi K, Alinejad B (2010) Enhancement of hydrogen generation rate in reaction of aluminum with water. *Int J Hydrogen Energ* 35: 5227–5232.
9. Flores-Chan JE, Bedolla-Jacuinde A, Patiño-Carachure C, et al. (2018) Corrosion study of Al–Fe (20 wt-%) alloy in artificial sea water with NaOH additions. *Can Metall Quart* 57: 201–209.
10. Hurtubise DW, Klosterman DA, Morgan AB (2018) Development and demonstration of a deployable apparatus for generating hydrogen from the hydrolysis of aluminum via sodium hydroxide. *Int J Hydrogen Energ* 43: 6777–6788.
11. Porciúncula CB, Marcilio NR, Tessaro IC, et al. (2012) Production of hydrogen in the reaction between aluminum and water in the presence of NaOH and KOH. *Braz J Chem Eng* 29: 337–348.
12. Al Bacha S, Zakhour M, Nakhl M, et al. (2020) Effect of ball milling in presence of additives (Graphite, AlCl<sub>3</sub>, MgCl<sub>2</sub> and NaCl) on the hydrolysis performances of Mg<sub>17</sub>Al<sub>12</sub>. *Int J Hydrogen Energ* 45: 6102–6109.
13. Razavi-Tousi SS, Szpunar JA (2016) Effect of addition of water-soluble salts on the hydrogen generation of aluminum in reaction with hot water. *J Alloy Compd* 679: 364–374.
14. Li F, Zhu B, Sun Y, et al. (2017) Hydrogen generation by means of the combustion of aluminum powder/sodium borohydride in steam. *Int J Hydrogen Energ* 42: 3804–3812.
15. Xiao F, Yang R, Gao W, et al. (2020) Effect of carbon materials and bismuth particle size on hydrogen generation using aluminum-based composites. *J Alloy Compd* 817: 152800.
16. Guan X, Zhou Z, Luo P, et al. (2019) Hydrogen generation from the reaction of Al-based composites activated by low-melting-point metals/oxides/salts with water. *Energy* 188: 116107.
17. Qiao D, Lu Y, Tang Z, et al. (2019) The superior hydrogen-generation performance of multicomponent Al alloys by the hydrolysis reaction. *Int J Hydrogen Energ* 44: 3527–3537.
18. Yang B, Zhu J, Jiang T, et al. (2017) Effect of heat treatment on AlMgGaInSn alloy for hydrogen generation through hydrolysis reaction. *Int J Hydrogen Energ* 42: 24393–24403.
19. Du BD, He TT, Liu GL, et al. (2018) Al-water reactivity of AlMgGaInSn alloys used for hydraulic fracturing tools. *Int J Hydrogen Energ* 43: 7201–7215.
20. Liang J, Gao LJ, Miao NN, et al. (2016) Hydrogen generation by reaction of Al–M (M = Fe, Co, Ni) with water. *Energy* 113: 282–287.
21. López-Miranda JL, Rosas G (2016) Hydrogen generation by aluminum hydrolysis using the Fe<sub>2</sub>Al<sub>5</sub> intermetallic compound. *Int J Hydrogen Energ* 41: 4054–4059.
22. Brisse A, Schefold J, Zahid M (2008) High temperature water electrolysis in solid oxide cells. *Int J Hydrogen Energ* 33: 5375–5382.
23. Ilyukhina AV, Kravchenko OV, Bulychev BM (2017) Studies on microstructure of activated aluminum and its hydrogen generation properties in aluminum/water reaction. *J Alloy Compd* 690: 321–329.
24. Acar C, Dincer I (2019) Review and evaluation of hydrogen production options for better environment. *J Clean Prod* 218: 835–849.
25. Ho CY, Huang CH (2016) Enhancement of hydrogen generation using waste aluminum cans hydrolysis in low alkaline de-ionized water. *Int J Hydrogen Energ* 41: 3741–3747.
26. Du Preez, SP, Bessarabov DG (2018) Hydrogen generation by the hydrolysis of mechanochemically activated aluminum-tin-indium composites in pure water. *Int J Hydrogen Energ* 43: 21398–21413.
27. Du Preez SP, Bessarabov DG. (2019) The effects of bismuth and tin on the mechanochemical processing of aluminum-based composites for hydrogen generation purposes. *Int J Hydrogen Energ* 44: 21896–21912.
28. Irankhah A, Fattahi SMS, Salem M (2018) Hydrogen generation using activated aluminum/water reaction. *Int J Hydrogen Energ* 43: 15739–15748.
29. Suryanarayana C (2001) Mechanical alloying and milling. *Prog Mater Sci* 46: 1–184.
30. Saceleanu F, Vuong TV, Master ER, et al. (2019) Tunable kinetics of nanoaluminum and microaluminum powders reacting with water to produce hydrogen. *Int J Energ Res* 43: 7384–7396.
31. Salazar M, Pérez R, Rosas G (2005) Environmental embrittlement characteristics of the AlFe and AlCuFe intermetallic systems. *J New Mater Electrochem Syst* 8: 97–100.
32. Krasnowski M, Gierlotka S, Ciołek S, et al. (2019) Nanocrystalline NiAl intermetallic alloy with high hardness produced by mechanical alloying and hot-pressing consolidation. *Adv Powder Technol* 30: 1312–1318.

33. Naghiha H, Movahedi B, Asadabad MA, et al. (2017) Amorphization and nanocrystalline Nb<sub>3</sub>Al intermetallic formation during mechanical alloying and subsequent annealing. *Adv Powder Technol* 28: 340–345.
34. Antipina SA, Zmanovskii SV, Gromov AA, et al. (2017) Air and water oxidation of aluminum flake particles. *Powder Technol* 307: 184–189.
35. Wang HW, Chung HW, Teng HT, et al. (2011) Generation of hydrogen from aluminum and water-effect of metal oxide nanocrystals and water quality. *Int J Hydrogen Energ* 36: 15136–15144.
36. Gai WZ, Deng ZY (2014) Effect of trace species in water on the reaction of Al with water. *Journal Power Sources* 245: 721–729.
37. Ma GL, Dai HB, Zhuang DW, et al. (2012) Controlled hydrogen generation by reaction of aluminum/sodium hydroxide/sodium stannate solid mixture with water. *Int J Hydrogen Energ* 37: 5811–5816.
38. Xu S, Zhao X, Liu J (2018) Liquid metal activated aluminum-water reaction for direct hydrogen generation at room temperature. *Renew Sust Energ Rev* 92: 17–37.
39. Nie H, Schoenitz M, Dreizin EL (2012) Calorimetric investigation of the aluminum–water reaction. *Int J Hydrogen Energ* 37: 11035–11045.
40. Belete TT, Van De Sanden MCM, Gleeson MA (2019) Effects of transition metal dopants on the calcination of CaCO<sub>3</sub> under Ar, H<sub>2</sub>O and H<sub>2</sub>. *J CO<sub>2</sub> Util* 31: 152–166.
41. Liu H, Yang F, Yang B, et al. (2018) Rapid hydrogen generation through aluminum-water reaction in alkali solution. *Catal Today* 318: 52–58.
42. Soler L, Candela AM, Macanás J, et al. (2009) Hydrogen generation by aluminum corrosion in seawater promoted by suspensions of aluminum hydroxide. *Int J Hydrogen Energ* 34: 8511–8518.
43. Xiao F, Guo Y, Li J, et al. (2018) Hydrogen generation from hydrolysis of activated aluminum composites in tap water. *Energy* 157: 608–614.
44. Wang CC, Chou YC, Yen CY (2012) Hydrogen Generation from aluminum and aluminum alloys powder. *Procedia Eng* 36: 105–113.

---

---

# Construction and building materials

**Anrea Di Schino\* and Marco Corradi**

<sup>1</sup>Department of Engineering, University of Perugia, 06125 Perugia, Italy

\* Correspondence: Email: andrea.dischino@unipg.it.

## 1. INTRODUCTION AND SCOPE

Construction materials and related technologies represent a quite interesting wide field from scientific, technological and commercial perspectives. They include metal reinforcement, bricks and mortars, masonry, timber, steels (common and stainless steels), polymers, composite fibers green materials, recycled materials. The scope of the special issue includes, but is not restricted to, new constructions and repair & reinforcement of civil engineering structures, infrastructures, silos, highway pavements, tunnels, water containment structures, sewers, bridges. The scope of this special issue embraces interdisciplinary work covering materials science and technological aspects, reporting about experimental and theoretical progress concerning materials microstructure, microstructure-properties relations, microstructure-applications relations.

## 2. CONTRIBUTIONS

The special issue collects manuscripts from academic and industrial researchers with stimulating new ideas and original results coming from scientists in Croatia, Italy, Japan, Russia, Malaysia, Norway, Pakistan and Russia so showing how such topic is diffused worldwide. The special issue consists of six research papers. Jandrić et al. [1] propose a new mathematical model for calculation of stresses on the basis of experimentally measured values of strains and temperature changes for niobium micro-alloyed steel. Construction of model was done using a multiple regression analysis of the measured values of temperature change, deformation and stresses at four different stretching rates. All investigations were conducted on samples from the niobium micro alloyed steel, using thermography and digital image correlation during static tensile testing. The model was tested and validated on the experimentally obtained results. Model showed a good agreement of calculated stress values with experimentally obtained ones. Di Schino [2] presents a new super-ferritic stainless steels family: these steels are characterized by a micro-structure and properties similar to those of more common ferritic alloys, with the advantage of higher chromium (Cr) and molybdenum (Mo) levels aimed to increase resistance at high temperature and corrosion behavior in aggressive environments, such as seawater. The research focuses on the corrosion behavior of recently developed super-ferritic stainless steels. Such steels are characterized by a Cr content ranging between 21% to 24% and very low carbon and nitrogen levels ( $C + N < 0.015\%$ ).

Moreover, low nickel (Ni) and Mo contents are adopted in such steels, following to the high costs of such elements. Ogawa et al. [3] reported about the tensile properties of ferrite single-phase lowcarbon steel with different initial microstructures were evaluated. Three types of hot-rolled sheet specimens with different microstructure were used. Results suggest that the homogeneous distribution of cementite and the fine recrystallized ferrite grains in specimen M suppress void coalescence, thereby resulting in a good balance between the tensile strength and the local elongation.

Gtnokow et al. report about correlation of the chemical composition, structure and mechanical properties of basalt continuous fibers [4]. They present the Basalt Continuous Fibers (BCF) tensile strength dependence on their chemical composition. 14 different basalt deposits were used to obtain

continuous fibers by a laboratory scale system. Based on the data for more than 15 articles focused on natural basalt continuous fibers (32 different compositions) and experimental data of 14 experimental BCF series, the correlation of the tensile strength, the acid modulus and the NBO/T parameter was calculated. The PCC (Pearson Correlation Coefficient) value of NBO/T and the tensile strength was 0.79, for acidity modulus and tensile strength. Raman data for experimental BCF confirm the significant influence of the chemical composition of basalts on their structure, which determines their tensile strength. With a decrease in NBO/T, the observed ratio between the Raman bands at low- and high-frequencies gradually increases. Thorstensen [5] reports about Preventing early age chloride migration into low-carbon concrete. Results indicate a potential for reducing chloride penetration with efficiency up to 90%, depending on the exposure regime and the maturity level of the concrete and the hydrophobic paint. Ahmad et al. [6] report about mechanical properties of hot-mix asphalt using waste crumber rubber and phenol formaldehyde polymer. The authors demonstrate that crumb rubber and bakelite has potential to enhance the mechanical properties and between them Bakelite shows better result in term of higher strength and stiffness.

## ACKNOWLEDGMENTS

As Guest Editor, we would like to especially thank Huilin Cui, Assistant Editor, for his support and active role in the publication. We are also grateful to the entire staff of AIMS Materials Science for the precious collaboration. Last but not least, we wish to express our gratitude to all the contributing authors and reviewers: without your excellent work it would not have been possible to accomplish this Special Issue that we hope will be a piece of interesting reading and reference literature.

## Conflict of interests

There is not any conflict of interests between authors.

## REFERENCES

1. Jandrić I, Rešković S, Dušan C, et al. (2019) Modeling of stress distribution on the basis of the measured values of strain and temperature changes. *AIMS Mater Sci* 6: 601–609.
2. Di Schino A (2019) Corrosion behavior of new generation super-ferritic stainless steels. *AIMS Mater Sci* 6: 646–656.
3. Ogawa T, Dannoshita H, Adachi Y (2019) Evaluation of tensile properties of ferrite singlephase low-carbon steel with different initial microstructures. *AIMS Mater Sci* 6: 798–805.
4. Gutnikov SI, Zhukovskaya ES, Popov SS, et al. Correlation of the chemical composition, structure and mechanical properties of basalt continuous fibers. *AIMS Mater Sci* 6: 806–820.
5. Thorstensen RT (2019) Preventing early age chloride migration into low-carbon concrete. *AIMS Mater Sci* 6: 1020–1032.
6. Ahmad M, Beddu S, Hussain S, et al. (2019) Mechanical properties of hot-mix asphalt using waste crumber rubber and phenol formaldehyde polymer. *AIMS Mater Sci* 6: 1164–1175.

# Structural and Multiferroic Properties of (Sm, Mn) Co-Doped BiFeO<sub>3</sub> Materials

Dao Viet Thang<sup>1,2,\*</sup>, Nguyen Manh Hung<sup>1,2</sup>, Nguyen Cao Khang<sup>2</sup> and Le Thi Mai Oanh<sup>2</sup>

<sup>1</sup>Departement of Physics, Hanoi University of Mining and Geology, 18 Vien Street, Duc Thang Ward, North Tuliem District, Hanoi, Vietnam

<sup>2</sup>Center for Nano Science and Technology, Hanoi National University of Education, 136 Xuan Thuy Road, Cau Giay District, Hanoi, Vietnam

\* Correspondence: Email: daovietthang@humg.edu.vn; Tel: +84985811377.

## ABSTRACT

*Pure BiFeO<sub>3</sub> (BFO) and (Sm, Mn) co-doped materials were synthesized by the citrate method. Effects of (Sm, Mn) co-doping on the structural, magnetic, electrical and ferroelectric properties of the BFO materials were characterized and investigated by different techniques, such as X-ray diffraction (XRD), Raman scattering spectroscopy, magnetic hysteresis (M–H) loops, electric polarization hysteresis loops, and complex impedance spectra measurements. Analysis results of the XRD measurement show that all samples were crystallized in the rhombohedral structure with R<sub>3</sub>C space group and crystal lattice parameters of  $a = 0.5584$  nm,  $c = 1.3874$  nm and the average crystal size of LXRD = 60 nm for BFO sample. The crystal lattice parameters  $a$ ,  $c$  and the average crystal size LXRD of (Sm, Mn) co-doped samples were found to decrease with the increasing Sm concentration. The Raman scattering spectral show that the position of peaks characteristic for the Fe–O bonds in the (Sm, Mn) co-doped samples shifts toward lower frequency compared to that of BFO. For the (Sm, Mn) co-doped samples, the position of peaks characteristic for Bi–O covalent bonds shifts toward higher frequencies when the Sm concentration increases, confirming that Sm<sup>3+</sup> and Mn<sup>2+</sup> ions are substituted into Bi-sites and Fe-sites, respectively. The data from the magnetic hysteresis loop measurements indicate that all samples exhibit weak ferromagnetic behavior. The BFO sample presents weak ferromagnetic properties with a saturation magnetization of  $M_s = 0.015$  emu/g and the remnant magnetization of  $M_r = 0.007$  emu/g. Ferromagnetic properties of the (Sm, Mn) co-doped samples are found enhanced compared to those of BFO. The origin of ferromagnetism of the materials has been considered.*

**Keywords:** X-ray, Raman, (Sm, Mn) co-doped, ferromagnetic, ferroelectric

## 1. INTRODUCTION

Multiferroic materials are known from several previous studies to contain coexisting ferromagnetic (antiferromagnetic), ferroelectric orders and to exhibit ferroelasticity and magnetoelectric (ME) effect in the same structure phase [1–4]. These materials have found broad application in electronic devices, such as information storage, memory sensor, and also in ultrasonic technologies. Due to the competition between the ferromagnetic and the ferroelectric orders, the multiferroic materials are very rarely available in the nature. BiFeO<sub>3</sub> (BFO) has a small saturated magnetization and a small electric polarization, that limit the applicability of this materials. This problem can be solved by modification of the magnetic and electrical properties substitution of rare earth ions (such as Sm<sup>3+</sup>, Nd<sup>3+</sup>, Gd<sup>3+</sup>, Ho<sup>3+</sup>, etc.) into the Bi-sites [5–7] or transition metal ions (such as Ni<sup>2+</sup>, Co<sup>2+</sup>, Mn<sup>2+</sup>, etc.) into the Fe-sites [8–10]. Recently, some studies showed that both the ferromagnetic and ferroelectric properties are enhanced as rare earth (RE) and transition metal (TM) ions are co-doped into the BFO host materials [11–13].

Chakrabarti et al. [14] and Zhang et al. [15] pointed out that the magnetization of (Eu, Co) or (La, Co) co-doped BFO was enhanced by a few times of that the parent BFO compound. Ye et al. [16] also have shown that the (Ho, Mn) co-doped BFO compound exhibit to improve ferromagnetic and ferroelectric properties compared to those of BFO.

In this work, Sm and Mn are chosen for co-doping into the BFO host materials. Because Sm doped  $\text{BiFeO}_3$  can improve magnetic and dielectric properties, Mn substitution for the Fe-site is expected to further affect the magnetic and ferroelectric properties to a greater extent resulting in a larger ME effect at room temperature [16–18]. Some previous studies also have shown that the Mn concentration of about 2% to 3% molar was the appropriate one for effectively doping into the BFO host materials [12,19,20]. In this work, we use a fixed Mn concentration of 3% molar and a Sm concentration in the range from 2% to 12% molar to study the effect (Sm, Mn) co-doping on the structural and other physical properties of BFO.

## 2. MATERIALS AND METHODS

### 2.1. Materials synthesis

Pure  $\text{BiFeO}_3$  and (Sm, Mn) co-doped  $\text{BiFeO}_3$  materials were synthesized by citrate method. The firstly,  $\text{Bi}(\text{NO}_3)_3 \cdot 5\text{H}_2\text{O}$ ,  $\text{Fe}(\text{NO}_3)_3 \cdot 9\text{H}_2\text{O}$ ,  $\text{Sm}(\text{NO}_3)_3 \cdot 6\text{H}_2\text{O}$ , and  $\text{Mn}(\text{NO}_3)_2 \cdot 4\text{H}_2\text{O}$  were dissolved in 35 mL citric acid solution. The solution was then mixed by magnetic stirring at the temperature of 60 °C for 45 min to obtain so solution. Then, temperature of the sol was increased to 100 °C to evaporate the water for 3 h obtaining the wet gel. In the next, the gel was dried at 130 °C for 4 h. Finally, dry gel was annealed at temperature 800 °C for 7 h in air to obtain the powder materials. The chemicals used were:  $\text{Bi}(\text{NO}_3)_3 \cdot 5\text{H}_2\text{O}$  (Sigma-Aldrich, 98%),  $\text{Fe}(\text{NO}_3)_3 \cdot 9\text{H}_2\text{O}$  (Sigma-Aldrich, 98%),  $\text{Sm}(\text{NO}_3)_3 \cdot 6\text{H}_2\text{O}$  (Sigma-Aldrich, 99.99%),  $\text{Mn}(\text{NO}_3)_2 \cdot 4\text{H}_2\text{O}$  (Sigma-Aldrich, 98%),  $\text{C}_2\text{H}_6\text{O}_2$  (Sigma-Aldrich, 98%), and  $\text{HOC}(\text{COOH})(\text{CH}_2\text{COOH})_2$  (Sigma-Aldrich, 99%).

For the measurements of the complex impedance and electric polarization hysteresis loops of all samples, powder materials were compressed at a pressure of 20 MPa into pellets of 6.106 mm in diameter and 1.06 mm in thickness. The pellets were sintered at of 800 °C for 5 h. Then, the ceramic pellets were polished to the accurate thickness. Finally, the samples were evenly covered with Pt glue as electrode and sintered at of 500 °C for 3 h to obtain the appropriate specimens for the measurements of complex impedance spectra.

### 2.2. Microstructural characterization

The microstructure, magnetic and ferroelectric properties of all samples were investigated by using X-ray diffraction (D8 Advance, Cu-K $\alpha$  radiation), Raman scattering (LabRAM HR Evolution,  $\lambda = 532$  nm), magnetization hysteresis loops (Lake Shore Cryotronics, 704 VSM), and electric polarization hysteresis loops (Radiant, Precision LC 10 V), and complex impedance measurement (LeCroy equipment with frequency range from 10 Hz to 5.3 MHz and using the LabView 8.0 software).

## 3. RESULTS AND DISCUSSION

### 3.1. X-ray diffraction

The phase formation and crystal structure of  $\text{BiFeO}_3$  (BFO) and (Sm, Mn) co-doped  $\text{BiFeO}_3$  materials were investigated by X-ray diffraction (XRD). The XRD patterns of all samples are shown in Figure 1.

The refinement of these patterns following the standard cards JPCDS No. 71-2494 revealed that all samples exhibit rhombohedral crystal structure of the original BiFeO<sub>3</sub> compound. The main diffraction peaks could be indexed to the (012), (104), (110), (006), (202), (024), (116), (122), (018), and (300) crystalline planes, as indicated in Figure 1a. The XRD patterns of (Sm, Mn) co-doped samples show that Sm<sup>3+</sup> and Mn<sup>2+</sup> ions are well incorporated into the BFO crystal lattice.

Figure 1b shows a comparison of the positions of the (012), (104) and (110) peaks, which may depict the effects of (Sm, Mn) co-doping on the crystal structure of BFO. As it is seen, the corresponding peaks of the (Sm, Mn) co-doped samples shift toward higher 2θ values compared to those of the undoped BFO sample. From data of XRD analysis, the crystal lattice parameter and the average crystallite size (LXRD) have been determined by using the UnitCell software and the Debye Scherrer's formula, and results are shown in Table 1. As seen in Table 1, the BFO sample has crystal lattice parameters of a = 0.5584 nm, c = 1.3875 nm and the average crystal size LXRD = 60 nm. It is also seen that the crystal lattice parameters and the average crystal size of the (Sm, Mn) co-doped samples decrease when the Sm-concentration increases. This observation can be easily understood considering the large ionic radius of Mn<sup>2+</sup> (0.067 nm) compared to that of Fe<sup>3+</sup> (0.065 nm). When the Mn<sup>2+</sup> ions are substituted into Fe-sites they cause an expansion of the crystal lattice, which in turn increases the length of the Fe/Mn–O bonds. For the (Sm, Mn) co-doped samples, the diffraction peaks shift toward higher 2θ values compare to those of the BFO sample, which could be explained as due to the smaller ionic radius of Sm<sup>3+</sup> (0.108 nm) compare to that of Bi<sup>3+</sup> (0.117 nm). The presence of the small Sm<sup>3+</sup> ions leads to the contraction of the crystal lattice. Furthermore, the Sm<sup>3+</sup> ion with the small ionic radius is not large enough to fill the 12-sided cavity created by the BO<sub>6</sub> octahedron causing the BO<sub>6</sub> octahedron to rotate (B-site is Fe or Mn), which reduces the 12-sided cavity volume. So, at the low concentration of Sm (x ≤ 0.08), the value of a lattice parameter seems to remain unchanged while the value of c slightly decreases to compared with that of BFO sample.

For the (Sm, Mn) co-doped samples with higher Sm-concentrations, the rotation BO<sub>6</sub> octahedron is significant leading to the significant reduction of both the a and c parameters. So, the simultaneous substitution of Sm<sup>3+</sup> and Mn<sup>2+</sup>, respectively, into the Bi-sites and the Fe-sites leads to the shrank of the crystal lattice, which is related to the decrease of the Bi/Sm–O bonds. This may be the reasons for the decrease of the crystal lattice parameters and the average crystal size, as shown in Table 1.

Previous studies also indicated that the lattice parameters change due to the fact that ionic radius of Sm<sup>3+</sup> is smaller than that of Bi<sup>3+</sup> and the ionic radius of Mn<sup>2+</sup> is larger than that of Fe<sup>3+</sup> [21].

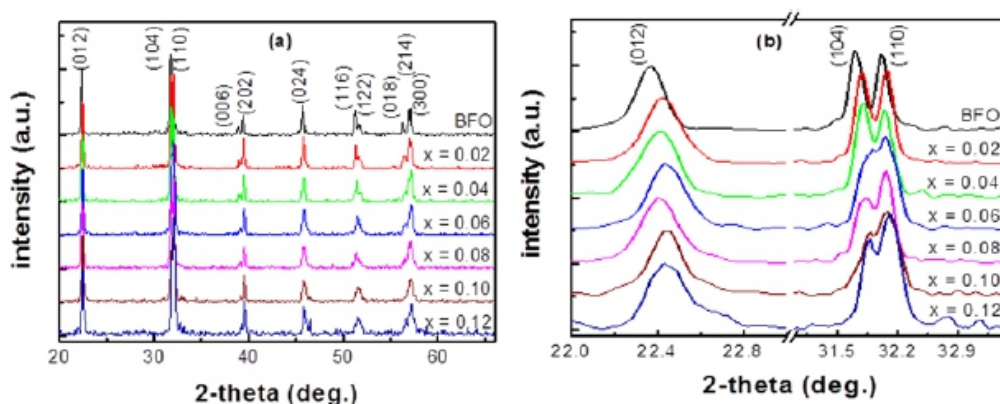


**Figure 1. (a) X-ray diffraction diagrams of BiFeO<sub>3</sub> and Bi<sub>1-x</sub>Sm<sub>x</sub>Fe<sub>0.97</sub>Mn<sub>0.03</sub>O<sub>3</sub> (x = 0.02, 0.04, 0.06, 0.08, 0.10, and 0.12) materials; (b) Comparison of the positions of the (012), (104), and (110) peaks.**

**Table 1. Crystal lattice parameters and average crystal size of BiFeO<sub>3</sub> and Bi<sub>1-x</sub>Sm<sub>x</sub>Fe<sub>0.97</sub>Mn<sub>0.03</sub>O<sub>3</sub> (x = 0.02, 0.04, 0.06, 0.08, 0.10, and 0.12) samples.**

Samples	<i>a</i> (nm)	<i>c</i> (nm)	<i>L</i> <sub>XRD</sub> (nm)
BFO	0.5584	1.3867	60
<i>x</i> = 0.02	0.5575	1.3819	51
<i>x</i> = 0.04	0.5577	1.3819	49
<i>x</i> = 0.06	0.5576	1.3817	49
<i>x</i> = 0.08	0.5578	1.3833	47
<i>x</i> = 0.10	0.5566	1.3754	43
<i>x</i> = 0.12	0.5563	1.3752	40

### 3.2. Raman scattering spectra

Raman scattering spectra of BFO and Bi<sub>1-x</sub>Sm<sub>x</sub>Fe<sub>0.97</sub>Mn<sub>0.03</sub>O<sub>3</sub> (x = 0.02, 0.04, 0.06, 0.08, 0.10, and 0.12) materials, as shown in Figure 2. According to the group theory, 13 Raman active modes could be expected for the rhombohedral BFO structure with the R3C space group ( $\Gamma = 4A_1 + 9E$ ) [22,23]. However, not all modes could be clearly observed at room temperature. In the analysis of the Raman scattering spectra for all samples, the positions of the Raman active modes for all samples are fitted by the Gaussian function. As one can see in Figure 2, Raman scattering spectra of the BFO sample has A1-1, A1-2, A1-3, E-2, E-3, E-4 modes, whereas Raman scattering spectra of the (Sm, Mn) co-doped samples have A1-1, A1-2, A1-3, E-2, E-3, E-4 and E-9 modes. When concentration of Sm increases the A1-1, A1-2, A1-3, E-2, E-3, and E-4 modes shift toward the higher frequencies compared to the situation in the BFO sample. Previous studies have also shown that the A1 modes and the E modes both at low frequencies are characteristic for the Bi–O covalent bonds, while other E modes at high frequencies are characteristic for the Fe–O bonds [24]. The A1-1, A1-2, A1-3, E-2, E-3, and E-4 modes are found characteristic for the Bi–O covalent bonds [13,25], while the E-9 mode is characteristic for the Fe–O bonds [10,26]. So the observed change positions of the E-9 modes shall confirmed that the Mn<sup>2+</sup> ions are substituted into the Fe-sites, and the change of the positions of the A1-1, A1-2, A1-3, E-2, E-3, and E-4 modes also confirmed Sm<sup>3+</sup> ions being substituted into the Bi-sites. These results are consistent with the XRD results, which confirmed that Sm<sup>3+</sup> and Mn<sup>2+</sup> ions are substituted into the Bi- and the Fe-sites, respectively.

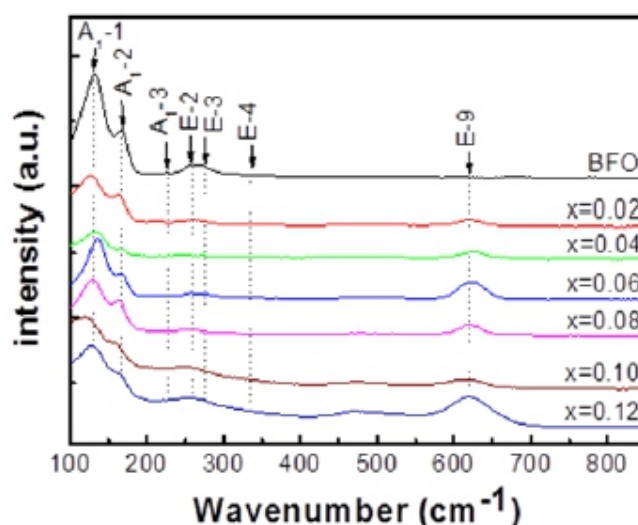


**Figure 2. Raman scattering spectra of BFO and Bi<sub>1-x</sub>Sm<sub>x</sub>Fe<sub>0.97</sub>Mn<sub>0.03</sub>O<sub>3</sub> (x = 0.02, 0.04, 0.06, 0.08, 0.10, and 0.12) materials.**

### 3.3. Magnetic properties

Figure 3a shows the magnetic hysteresis loops recorded for the BFO and  $\text{Bi}_{1-x}\text{Sm}_x\text{Fe}_{0.97}\text{Mn}_{0.03}\text{O}_3$  ( $x = 0.02, 0.04, 0.06, 0.08, 0.10$ , and  $0.12$ ) compounds at room temperature.

As it is seen in Figure 3a, all samples present a weak ferromagnetic behavior. The BFO sample has a saturation magnetization  $M_s = 0.015$  emu/g and remnant magnetization  $M_r = 0.007$  emu/g. For the (Sm, Mn) co-doped samples, the  $M_s$  and  $M_r$  values increase up to  $M_s = 0.04$  emu/g and  $M_r = 0.02$  emu/g, as are seen in Figure 3b. These results could be understood from the following consideration. Firstly, the substitution of the  $\text{Mn}^{2+}$  ions into the Fe-sites creates the exchange interaction between the  $\text{Mn}^{2+}$  ions with the neighbouring  $\text{Fe}^{3+}$  ions [27,28] leading to the change of the material's magnetic state from the antiferromagnetic to the ferrimagnetic order; Secondly, there exist double exchange interaction in the  $\text{Fe}^{3+}-\text{O}_2-\text{Mn}^{2+}$  chains resulting from the contribution of the 3d electrons in the magnetically active Fe/Mn atoms; Thirdly, the substitution of metal ions with another different valence state (i.e.  $\text{Mn}^{2+}$ ) leads to the structural lattice distortion and/or the breakdown of the balance between the antiparallel magnetizations in the sublattice of the  $\text{Fe}^{3+}$  ions. This can cause the canting of the antiferromagnetic ordering spins and thus enhances the total magnetization of materials [28]; Furthermore, the substitution of the  $\text{Mn}^{2+}$  ions into the  $\text{BiFeO}_3$  crystal lattice creates oxygen vacancies and lattice defects, which in turn also contributes to the enhancement of the material's magnetization [29].

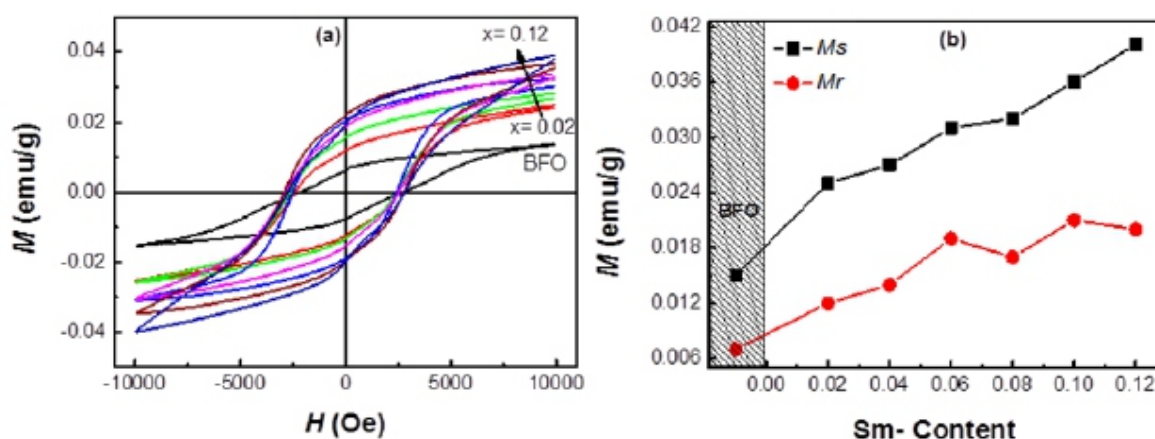


**Figure 3. (a) Magnetization hysteresis loops of  $\text{BiFeO}_3$  and  $\text{Bi}_{1-x}\text{Sm}_x\text{Fe}_{0.97}\text{Mn}_{0.03}\text{O}_3$  ( $x = 0.02, 0.04, 0.06, 0.08, 0.10$ , and  $0.12$ ) materials; (b) The  $M_s$  and  $M_r$  values depend on concentration of Sm.**

### 3.4. Ferroelectric properties

Figure 4a shows the room temperature polarization as a function of applied-electric fields of BFO and (Sm, Mn) co-doped samples. It is clear that all the samples show ferroelectric behavior.

The ferroelectric properties are clearly improved in (Sm, Mn) co-doped samples compared to that of the BFO sample. The saturation polarization ( $P_s$ ) and remnant polarization ( $P_r$ ) values of BFO and ( $S_m$ ,  $M_n$ ) co-doped samples, as shown in Figure 4b. For ( $S_m$ ,  $M_n$ ) co-doped samples show the  $P_s$  and  $P_r$  values, indicating the best improvement of ferroelectric properties of BFO with ( $S_m$ ,  $M_n$ ) codoping.

This observation can be explained as the substitution of Sm into the Bi-sites, leading to modification of the Bi/Sm–O bonding. On the hand, the substitution of Mn into Fe-sites created oxygen vacancies and changes the  $\text{FeO}_6$  octahedron, leading to enhancement of  $P_s$  and  $P_r$ .

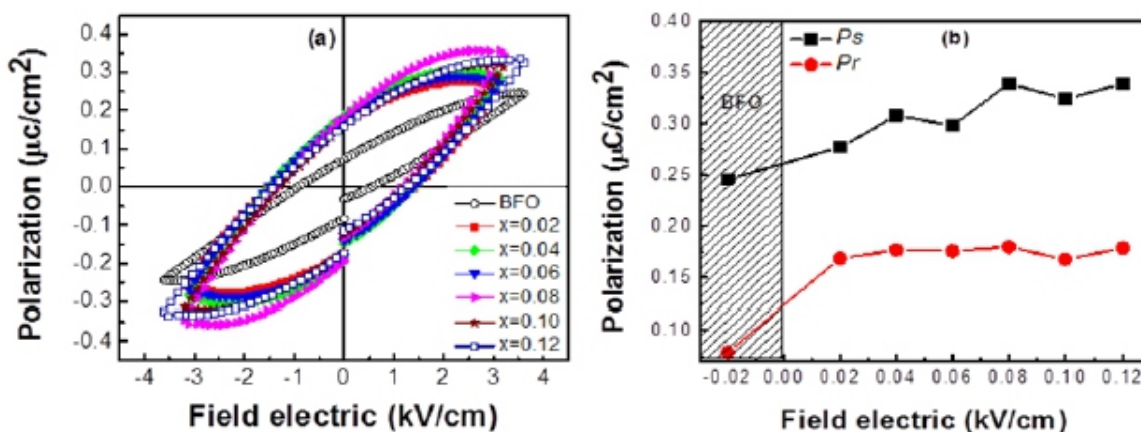


**Figure 4. (a) Polarization electric hysteresis loops of BiFeO<sub>3</sub> and Bi<sub>1-x</sub>Sm<sub>x</sub>Fe<sub>0.97</sub>Mn<sub>0.03</sub>O<sub>3</sub> (x = 0.02, 0.04, 0.06, 0.08, 0.10, and 0.12) materials; (b) The P<sub>s</sub> and P<sub>r</sub> values depend on concentration of S<sub>m</sub>.**

### 3.5. Complex impedance spectra

Figure 5 shows complex impedance spectra of the BiFeO<sub>3</sub> and Bi<sub>1-x</sub>Sm<sub>x</sub>Fe<sub>0.97</sub>Mn<sub>0.03</sub>O<sub>3</sub> (x = 0.02, 0.06, and 0.08) materials. The complex impedance spectra of materials are known to consist of the various contributions from intra- and inter-grains, grain boundaries, and the electrode interfaces. The complex impedance spectra in term of the Cole-Cole plot are presented in successive semicircles indicating the imaginary part vs. the real part in the complex plane. A high frequency semicircles originate from intragrain contributions, a semicircle in the intermediate frequency provides information on the contributions from the grain boundaries, whereas the low frequency semicircle associates to the ion and electron transfer at the contact interface between the sample and the measuring electrode [12,30,31]. Impedance spectra are determined by the frequency range of the measurements, but all these contributions may not be ruled out. Some previous studies also showed the distinction between the intra and the inter-grain contributions which are related to the defects in ferroelectric materials [32,33]. The complex impedance spectra thus can provide reliable information on the dielectric properties of materials. In our work, for all samples, the simulated curves agree quite well with the experimental ones. As it is seen in Figure 5, the impedance spectra of the BFO and (S<sub>m</sub>, M<sub>n</sub>) co-doping samples consist of a semicircle at the high frequency region, toward zero in the complex plane presenting the intragrain contribution and a semicircle at the intermediate frequency, untoward zero in the complex plane presenting the grain boundaries. However, due to limited measurement frequency range, the contribution of the electrode interface to the impedance could not be fairly detected in all the investigate samples. These presented results provide, thus, just some preliminary information pointing out significant modification of the dielectric properties of the (S<sub>m</sub>, M<sub>n</sub>) co-doped BiFeO<sub>3</sub> materials. Which is consistent with results of the hysteresis loop measurement showed the ferroelectric properties of (S<sub>m</sub>, M<sub>n</sub>) co-doping samples was improved to compared with that of BFO sample.

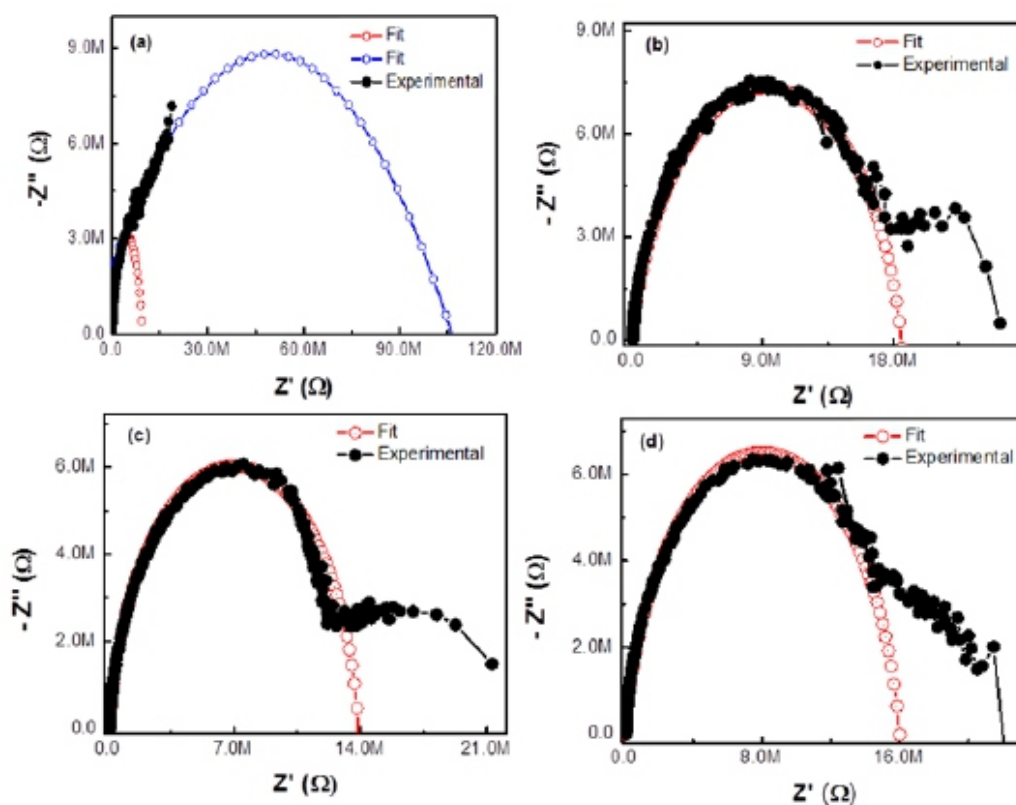


**Figure 5. Impedance spectra of  $\text{BiFeO}_3$  and  $\text{Bi}_{1-x}\text{Sm}_x\text{Fe}_{0.97}\text{Mn}_{0.03}\text{O}_3$  samples: (a)  $\text{BiFeO}_3$ ; (b)  $x = 0.02$ ; (c)  $x = 0.06$ ; (d)  $x = 0.08$ .**

#### 4. CONCLUSION

In summary,  $\text{BiFeO}_3$  and  $\text{Bi}_{1-x}\text{Sm}_x\text{Fe}_{0.97}\text{Mn}_{0.03}\text{O}_3$  ( $x = 0.02, 0.04, 0.06, 0.08, 0.10, \text{ and } 0.12$ ) materials have been successfully fabricated by citrate method. All samples crystallize in rhombohedral structure of  $\text{BiFeO}_3$  materials. Crystal lattice parameters and average crystallite size of ( $\text{S}_m, \text{M}_n$ ) co-doping samples decreased gradually compared to those of  $\text{BiFeO}_3$  sample. X-ray diffraction patterns and Raman scattering spectra confirmed the successful substitution of  $\text{Sm}^{3+}$  and  $\text{Mn}^{2+}$  ions into  $\text{Bi}_i$  and Fe-sites, respectively, which affected obviously to magnetic and ferroelectric properties of  $\text{BiFeO}_3$  host materials. Magnetic and ferroelectric properties of ( $\text{S}_m, \text{M}_n$ ) co-doping samples enhanced to compared with those of  $\text{BiFeO}_3$  materials.

#### Acknowledgements

This work has been supported by the Ministry of Education and Training of Vietnam (Code B2018-MDA-02-CtrVL).

#### Conflict of interests

The authors declare no conflicts of interests.

#### References

1. Eerenstein W, Mathur ND, Scott JF (2006) Multiferroic and magnetoelectric materials. *Nature* 442: 759–765.
2. Ederer C, Spaldin NA (2005) Weak ferromagnetism and magnetoelectric coupling in bismuth ferrite. *Phys Rev B* 71: 060401(R).
3. Ravindran P, Vidya R, Kjekshus A, et al. (2006) Theoretical investigation of magnetoelectric behavior in  $\text{BiFeO}_3$ . *Phys Rev B* 74: 224412.
4. Cheong SW, Mostovoy M (2007) Multiferroics: a magnetic twist for ferroelectricity. *Nat Mater* 6: 13–20.

5. Kumarn M, Sati PC, Chhoker S, et al. (2015) Electron spin resonance studies and improved magnetic properties of Gd substituted BiFeO<sub>3</sub> ceramics. *Ceram Int* 41: 777–786.
6. Zhang X, Sui Y, Wang X, et al. (2010) Effect of Eu substitution on the crystal structure and multiferroic properties of BiFeO<sub>3</sub>. *J Alloy Compd* 507: 157–161.
7. Pradhan SK, Das J, Rout PP, et al. (2010) Effect of holmium substitution for the improvement of multiferroic properties of BiFeO<sub>3</sub>. *J Phys Chem Solids* 71: 1557–1564.
8. Naganuma H, Miura J, Okamura S (2008) Ferroelectric, electrical and magnetic properties of Cr, Mn, Co, Ni, Cu added polycrystalline BiFeO<sub>3</sub> films. *Appl Phys Lett* 93: 052901.
9. Dai YR, Xun Q, Zheng X, et al. (2012) Magnetic properties of Ni-substituted BiFeO<sub>3</sub>. *Physica B* 407: 560–563.
10. Dong G, Tan G, Luo Y, et al. (2014) Optimization of the multiferroic BiFeO<sub>3</sub> thin films by divalent ion (Mn, Ni) co-doping at B-sites. *Mater Lett* 118: 31–33.
11. Thang DV, Hung NM, Khang NC, et al. (2017) Structural, magnetic and electric properties of Nd and Ni co-doped BiFeO<sub>3</sub> materials. *AIMS Mater Sci* 4: 982–990.
12. Thang DV, Hung NM, Khang NC, et al. (2019) Structural, electrical, and magnetic properties of Bi<sub>0.90</sub>Nd<sub>0.10</sub>Fe<sub>0.98</sub>TM<sub>0.02</sub>O<sub>3</sub> (TM = Mn, Co, Ni, and Cu) materials. *IEEE Magn Lett* 10: 1–5.
13. Yan X, Tan G, Liu W, et al. (2015) Structural, electric and magnetic properties of Dy and Mn co-doped BiFeO<sub>3</sub> thin film. *Ceram Int* 41: 3202–3207.
14. Chakrabarti K, Das K, Sarkar B, et al. (2012) Enhanced magnetic and dielectric properties of Eu and Co co-doped BiFeO<sub>3</sub> nanoparticles. *Appl Phys Lett* 101: 042401.
15. Zhang X, Zhang C, Ran N (2016) Tailoring the magnetic and optical characteristics of BiFeO<sub>3</sub> ceramics by doping with La and Co. *Mater Lett* 179: 186–189.
16. Ye W, Tan G, Dong G, et al. (2015) Improved multiferroic properties in (Ho, Mn) co-doped BiFeO<sub>3</sub> thin films prepared by chemical solution deposition. *Ceram Int* 41: 4668–4674.
17. Kumar A, Sharma P, Yang W, et al. (2016) Effect of La and Ni substitution on structure, dielectric and ferroelectric properties of BiFeO<sub>3</sub> ceramics. *Ceram Int* 42: 14805–14812.
18. Yun Q, Xing W, Chen J, et al. (2015) Effect of Ho and Mn co-doping on structural, ferroelectric and ferromagnetic properties of BiFeO<sub>3</sub> thin films. *Thin Solid Films* 584: 103–107.
19. Park JS, Yoo YJ, Hwang JS, et al. (2014) Enhanced ferromagnetic properties in Ho and Ni co-doped BiFeO<sub>3</sub> ceramics. *J Appl Phys* 115: 013904.
20. Rajput SS, Katoch R, Sahoo KK, et al. (2015) Enhanced electrical insulation and ferroelectricity in La and Ni co-doped BiFeO<sub>3</sub> thin film. *J Alloy Compd* 621: 339–344.
21. Xu X, Guoqiang T, Huijun R, et al. (2013) Structural, electric and multiferroic properties of Sm doped BiFeO<sub>3</sub> thin films prepared by the citrate process. *Ceram Int* 39: 6223–6228.
22. Hermet P, Goffinet M, Kreisel J, et al. (2007) Raman and infrared spectra of multiferroic bismuth ferrite from first principles. *Phys Rev B* 75: 220102.
23. Luo L, Wei W, Yuan X, et al. (2012) Multiferroic properties of Y-doped BiFeO<sub>3</sub>. *J Alloy Compd* 540: 36–38.
24. Yuan GL, Or SW, Chan HL (2007) Raman scattering spectra and ferroelectric properties of Bi<sub>1-x</sub>Nd<sub>x</sub>FeO<sub>3</sub> (x = 0–0.2) multiferroic ceramics. *J Appl Phys* 101: 064101.
25. Gautam A, Singh K, Sen K, et al. (2011) Crystal structure and magnetic property of Nd doped BiFeO<sub>3</sub> nanocrystallites. *Mater Lett* 65: 591–594.
26. Arora M, Sati PC, Chauhan S, et al. (2014) Structural, magnetic and optical properties of Ho–Co co-doped BiFeO<sub>3</sub> nanoparticles. *Mater Lett* 132: 327–330.
27. Yu L, Deng H, Zhou W, et al. (2016) Effects of (Sm, Mn and Ni) co-doping on structural, optical and magnetic properties of BiFeO<sub>3</sub> thin films fabricated by a citrate technique. *Mater Lett* 170: 85–88.
28. Rajan PI, Mahalakshmi S, Chandra S (2017) Establishment of half-metallicity, ferrimagnetic ordering and double exchange interactions in Ni-doped BiFeO<sub>3</sub>—A first-principles study. *Comp Mater Sci* 130: 84–90.
29. Xue X, Tan G, Dong G, et al. (2014) Studies on structural, electrical and optical properties of multiferroic (Ag, Ni and In) co-doped Bi<sub>0.9</sub>Nd<sub>0.1</sub>FeO<sub>3</sub> thin films. *Appl Surf Sci* 292: 702–709.
30. Thang DV, Van Minh N (2016) Magnetic properties and impedance spectroscopic studies of multiferroic Bi<sub>1-x</sub>Nd<sub>x</sub>FeO<sub>3</sub> materials. *J Magn* 21: 29–34.
31. Yao Y, Tao T, Liang B, et al. (2019) Pyroelectric properties and AC impedance study of bismuth ferrite (BiFeO<sub>3</sub>) ceramics. *Ceram Int* 45: 1308–1313.
32. Wang X, Liu J, Liang P, et al. (2018) Higher curie temperature and enhanced piezoelectrical properties in (Ba<sub>0.85</sub>Ca<sub>0.15-x</sub>Pbx)(Zr<sub>0.1</sub>Ti<sub>0.90-y</sub>Sny)O<sub>3</sub> Ceramics. *J Electron Mater* 47: 6121–6127.
33. Sahoo S, Hajra S, De M, et al. (2018) Processing, dielectric and impedance spectroscopy of lead free BaTiO<sub>3</sub>–BiFeO<sub>3</sub>–CaSnO<sub>3</sub>. *J Alloy Compd* 766: 25–32.

# Large Effects of Tiny Structural Changes on the Cluster Formation Process in Model Colloidal Fluids: An Integral Equation Study

Jean-Marc Bomont<sup>1</sup>, Dino Costa<sup>2</sup> and Jean-Louis Bretonnet<sup>1</sup>

<sup>1</sup>Universit e de Lorraine, LCP-A2MC UR 3469, 1 Bd. F. Arago, Metz, France

<sup>2</sup>Dipartimento di Scienze Matematiche e Informatiche, Scienze Fisiche e Scienze della Terra  
Universit a degli Studi di Messina, Viale F. Stagno d'Alcontres 31, 98166 Messina, Italy

\* Correspondence: Email: jean-marc.bomont@univ-lorraine.fr; Tel: +33681063922.

## ABSTRACT

The formation of aggregates is commonly observed in soft matter such as globular protein solutions and colloidal suspensions. A lively debated issue concerns the possibility to discriminate between a generic intermediate-range order taking place in the fluid, as contrasted with the more specific presence of a clustered state. Recently, we have predicted by Monte Carlo simulations of a standard colloidal model — spherical particles interacting via a short-range attraction followed by a screened electrostatic repulsion at larger distances — the existence of a tiny structural change occurring in the pair structure. This change consists in a reversal of trend affecting a portion of the local density as the attractive strength increases, that is shown to take place precisely at the clustering threshold. Here, we address the same issue by refined thermodynamically self-consistent integral equation theories of the liquid state. We document how such theoretical schemes positively account for the observed phenomenology, highlighting their accuracy to finely describe the aggregation processes in model fluids with microscopic competing interactions.

**Keywords:** colloidal suspensions, cluster formation process, competing interactions, clustering threshold, simulation, integral equation theories

## 1. INTRODUCTION

It is well established that the breadth of equilibrium fluid phases exhibited by relevant soft matter, such as globular protein solutions and colloidal suspensions, extends well beyond a macroscopic liquid-vapor phase separation, giving rise to inhomogeneous fluids phases composed of clusters or patterned morphologies [1].

At the microscopic level, the origin of such structures is commonly ascribed to the presence of competing interactions acting on different length scales: the propensity to form equilibrium clusters phases — heralding the development of patterned morphologies — stems from the competition between a short-range attraction, favouring aggregation, and a long-range repulsion, frustrating a complete phase separation [2]. Model potentials of this kind are usually referred to as SALR (Short-range Attractive and Long-range Repulsive) interactions [3].

A flourishing literature clarified many aspects of the physics of SALR models (see e.g. [4–17]), including a broad assessment of their accuracy in describing general aspects of structure and thermodynamics of real protein solutions and colloidal suspensions, see e.g. [18–23]. The large interest on this topic is witnessed by several recent reviews [24–27].

At the structural level, a ubiquitous indication to detect the presence of aggregates is provided by a peak in the static structure factor  $S(q)$ , located at a wavenumber  $q_c$  well below the position of the main diffraction peak, see e.g. [28–31]. Nonetheless, a live debate concerns the correct relationship between such a low- $q$  peak and the effective microscopic arrangement taking place in the fluid. Initially, this feature was related to the specific existence of equilibrium clusters, as observed both in colloid-polymer mixtures and in protein solutions [28]. However, the presence of such clusters was questioned by other experiments on similar systems [32–34]. Later on, a series of coupled dynamical and structural experiments on lysozyme solutions suggested the low- $q$  peak in  $S(q)$  to arise from the formation of a generic Intermediate-Range Order (IRO) taking place in the fluid [21–23]. Such a situation, to be contrasted with the more specific formation of clusters, corresponds to a less distinct, locally nonhomogeneous microscopic arrangement characterized by the presence of aggregates with sizes ranging from dimers, trimers on, with a fast decrease of associated probability distribution [35,36]. This picture turns back to prior conclusions about the onset of a “medium-range order” in models for covalently bonded non-crystalline materials [37, 38]. Therein, the presence of the low- $q$  peak was ascribed to a local icosahedral order in the fluid. The original investigations in [21–23] prompted most recent studies, investigating dynamical properties of SALR fluids [39, 40].

Two different criteria, based on the property of the low- $q$  peak, were proposed to discriminate between IRO and genuine clustering in model SALR fluids. In the first scheme [36], it is argued that clusters (at low density) or cluster-percolated states (at higher densities), are signaled by a height of the low- $q$  peak rising over  $2:7$ . This empirical observation closely recalls the Hansen-Verlet criterion for the freezing of simple fluids [41]. As for the second criterion, it is argued in [42] that clustering occurs as far as the thermal correlation length encoded in  $S(q_c)$  becomes larger than the typical length-scale associated with the long-range repulsion. Recently, we addressed the same issue by using Monte Carlo simulation for a common SALR model, focusing on correlations in the real space, as described by the local density ( $r$ ) [43, 44]. We have shown that, as the attractive strength increases, a threshold is crossed, whereupon a portion of ( $r$ ) experiences, at long distance, a tiny peculiar rearrangement, consisting in a reversal of trend. In coincidence,  $S(q_c)$  rapidly rises, in such a way that it goes almost discontinuously well over the threshold  $S(q_c) > 2:7$  (in agreement with the criterion of [36]), with the simultaneous appearance of a shoulder in the cluster-size distribution. Based on all such evidence, we argued that modifications observed in real-space correlation and onset of clustering are tightly linked.

In this work, we extend our previous investigation [43, 44], to ascertain the worth of Integral Equation Theories (IETs) of the liquid state to study the onset of clustering. The possibility to discriminate on the basis of purely structural indicators the underlying arrangement of SALR fluids, coupled with the use of effective theoretical tools, turns to be especially advantageous in all those cases in which microscopic data are not readily available. Theoretical tools are also beneficial for a wide investigation of clustering conditions in different SALR models upon disparate thermodynamic conditions, a task prohibitively costly to bear by simulations only. We have organized the paper as follows: after introducing our SALR model and IETs (Section 2), we present and discuss our main findings in Section 3. Concluding remarks and perspectives follow in Section 4.

## 2. MODEL AND THEORY

Theoretical calculations concern a standard SALR model, constituted by hard spheres of diameter interacting via a potential formed by the sum of two Yukawa contributions of opposite sign (hard-sphere two-Yukawa, HS2Y). Hence, the total interaction between a pair of spheres,  $v(x)$  — with  $x = r$  as the (reduced) interparticle distance — reads:

$$\beta v(x) = \begin{cases} \infty & \text{for } x < 1 \\ -\varepsilon \frac{\exp[-z_a(x-1)]}{x} + A \frac{\exp[-z_r(x-1)]}{x} & \text{for } x \geq 1 \end{cases} \quad (1)$$

where  $\beta = 1/k_B T$ , with  $T$  and  $k_B$  as the temperature and the Boltzmann constant, respectively. Positive parameters  $\varepsilon$  and  $A$  determine the strength of attractive and repulsive contributions respectively, while  $z_a$  and  $z_r$  (with  $z_a > z_r$ ), determine their corresponding ranges. We focus on a particular set of HS2Y parameters, widely adopted in previous studies [2, 8, 9, 15, 45]: we have fixed  $z_a = 1$ ,  $z_r = 0.5$ ,  $A = 0.5$  and let  $\varepsilon$  move from 0.9 to 1.6. Within our choice, the Mean Spherical Approximation predicts the occurrence of a microphase separation [2], the liquid-vapor coexistence taking over only for  $\varepsilon > 5$ .

We carry out our study at fixed reduced density  $\rho = 0.6$ , while the temperature is included in the definition of  $v(x)$ , see Eq 1. Our choice for such a relatively high density allows the fluid to develop spatial correlations extending over relatively large distances. In this way, we observe under optimal conditions the tiny structural rearrangements at the heart of our findings, to be discussed in the next section.

We determine the pair structure of our model by means of two thermodynamically self-consistent integral equations, namely the hybrid mean spherical approximation (HMSA), derived by Zerah and Hansen [46], and the Self-Consistent Integral Equation (SCIE) derived by two of us [47–49]. Both approaches provide a closure to the Ornstein–Zernike equation [1], relating the pair correlation function  $g(x)$  to the direct correlation function  $c(x)$ . Thermodynamically self-consistency is ensured by enforcing the equality of compressibilities obtained by two different routes from structure to thermodynamics [1], thank to the mixing parameter  $f$ , i.e.:

$$\rho k_B T \chi_T = \left[ 1 - \rho \sigma^3 \int c(x; f) d^3x \right]^{-1} = S(q = 0), \quad (2)$$

where  $\chi_T = -1/\rho (\partial P/\partial \rho)^{-1}$  is the isothermal compressibility and  $P$  is the pressure calculated via the virial theorem [1]. In order to calculate the total correlation function  $h(x) = g(x) - 1$  and the structure factor  $S(q)$ , both theories are solved numerically by the iterative Newton–Raphson method [50], over an extended grid of  $2^{14}$  points with a fine mesh of  $\Delta x = 0.005$ . Convergence is assumed when a difference smaller than  $10^{-8}$  is reached between two consecutive iterations. The mixing parameter  $f$  is determined so that Eq 2 is satisfied to within less than one percent.

We also study the onset of clustering in terms of the entropy of the fluid [51]. An approximation for such a property is provided by the pair entropy  $s_2$ , which involves only  $g(x)$ :

$$\frac{s_2}{k_B} = -2\pi\rho\sigma^3 \int_0^\infty [g(x) \ln g(x) - g(x) + 1] x^2 dx \quad (3)$$

This expression derives from the expansion of the configurational entropy in terms of multi-body correlations involving two, three and successively more particles [52–54]. In simple fluids, the leading term  $s_2$  is generally found to account for about 90% of the configurational entropy [54–56].

### 3. RESULTS AND DISCUSSION

In Figure 1, we show SCIE structural predictions for two different attractive strengths, namely

$\varepsilon = 0.9$  and 1.6. A low- $q$  peak is visible in the  $S(q)$  (A) and becomes more and more pronounced

as  $\varepsilon$  increases. According to [36], an IRO state takes place for  $\varepsilon = 0.9$  [where  $S(q_c) \approx 0.2$ ], while a more ordered clustered state occurs for  $\varepsilon = 1.6$  [where  $S(q_c) > 10$ ]. As for  $g(x)$ , in Figure 1B, the amplitude of the first four coordination shells — and apparently of the fifth one — increases with  $\varepsilon$ , while the corresponding position shifts to slightly lower distances. In contrast, for  $\varepsilon = 1.6$ ,  $g(x)$  no longer oscillates around one below  $x = 5$  and, as shown in the large view in the inset, next distant neighbors eventually merge into a single oscillation of wavelength  $\approx 9\sigma$ .

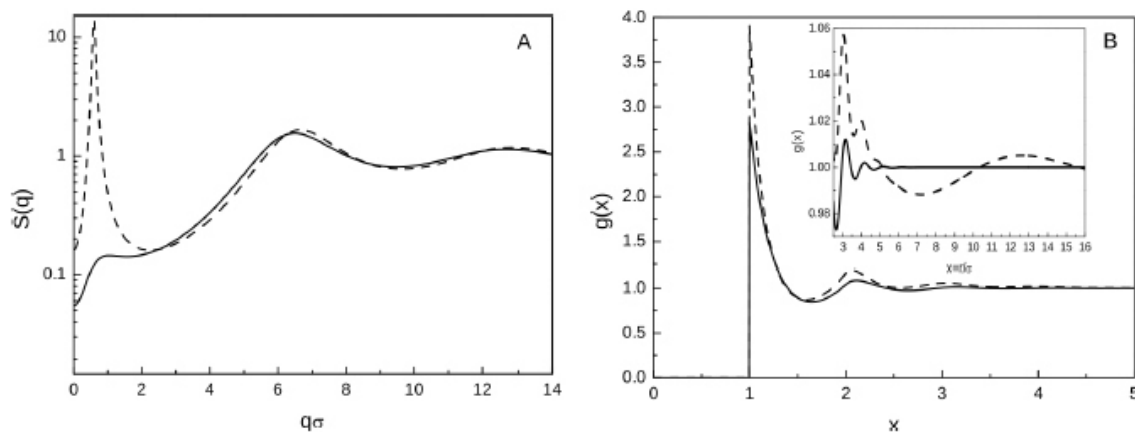


**Figure 1.** SCIE  $S(q)$  (A) and  $g(x)$  (B) for  $\varepsilon = 0.9$  (full lines) and  $\varepsilon = 1.6$  (dashed lines). Inset: overview of  $g(x)$  at intermediate/long interparticle separations: as  $\varepsilon$  increases, a long-wavelength oscillation rises.

Since SCIE correctly predicts the typical structural features we documented by MC [43], the question naturally arises so as to whether IETs are able to discriminate — on the basis of local, real-space properties — between a generic intermediate-range order and the more specific onset of clustering. To this purpose, we examine now in detail the structural modifications undergone by  $h(x)$ , as predicted by SCIE and HMSA, for intermediate attractive strengths. We recall that in [43] we identified the MC clustering threshold as falling at  $\varepsilon_t = 1.47$ . In Figures 2A and 2B we focus on the amplitude of the fifth neighbor peak of  $h(x)$ , denoted as  $h(x_5)$ ; therein, we see that the behavior of  $h(x_5)$  contrasts with that of the first four coordination shells in that it does not monotonically increase with  $\varepsilon$ . Specifically, in Figure 2A SCIE predicts that (i)  $h(x_5)$  starts to decrease from positive values as

$\varepsilon$  increases till, for  $\varepsilon = 1.33 \equiv \varepsilon_0$ , it turns negative and goes on decreasing, pointing to an increase of inhomogeneity in the fluid; apparently, since the fifth shell of neighbors seems to behave as next ones do, one may argue that it is about to merge into the heralding long-range oscillation. However, (ii) for  $\varepsilon = 1.545 \equiv \varepsilon_t$ ,  $h(x_5)$  reaches a minimum and starts rising, going over zero for higher  $\varepsilon$  values; in this way, the fifth coordination shell eventually contributes to the overall stabilization of the structure formed by the first four shells. This scenario remains unchanged within HMSA in Figure 2B, but for slightly different  $\varepsilon_0$  (1.375) and  $\varepsilon_t$  (1.535) and, as shown in Figure 2C, it faithfully reproduces the MC data [43]; the little anticipation of the MC threshold  $\varepsilon_t = 1.47$  does not impair, in our opinion, the quality of our theoretical predictions. To summarize, whatever the method used, a generic behavior of  $h(x_5)$  can be drawn in Figure 2D. Therein, a threshold value  $\varepsilon_t$  is identified, whereupon  $h(x_5)$  reaches a minimum, leading to the local property:

$$\left. \frac{\partial h(x_5; \varepsilon)}{\partial \varepsilon} \right|_{\varepsilon = \varepsilon_t} = 0 \tag{4}$$

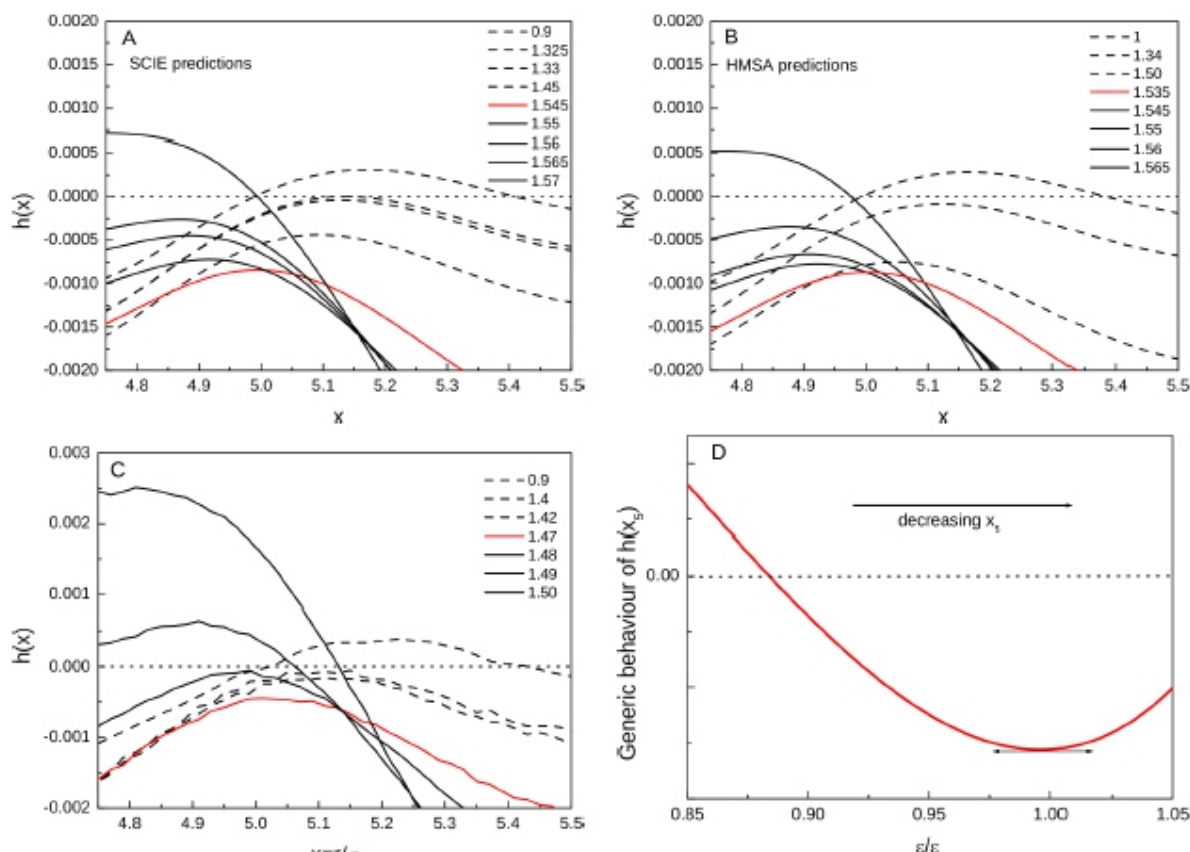


**Figure 2.** Portion of  $h(x)$  corresponding to the fifth coordination shell, for a series of  $\varepsilon$  (see legends), as obtained from SCIE (A), HMSA (B) and MC [43] (C). Dashed lines are for  $\varepsilon < \varepsilon_t$ , red lines for  $\varepsilon = \varepsilon_t$ , full lines for  $\varepsilon > \varepsilon_t$ . (D) Generic picture of  $h(x_5)$  vs  $\varepsilon$ : theories and simulation predict that  $h(x_5)$  passes through a minimum at  $\varepsilon = \varepsilon_t$ .

The consequences of our findings on the low-wavevector portion of the structure factor can be

clearly appraised from Figure 3. In 3A we see that, as  $\varepsilon$  approaches  $\varepsilon_t$ , the height of the low- $q$  peak,  $S(q_c)$ , slowly grows, with the fluid initially characterized by an intermediate-range order, then becoming progressively more structured. At  $\varepsilon = \varepsilon_t$ ,  $S(q_c)$  abruptly rises, exactly in correspondence with the real-space evidence that the fifth coordination shell correlates with the preceding ones. In agreement with our MC results [43], at this point the nature of the fluid changes, almost discontinuously, into a clustered state characterized by  $S(q_c) > 2.7$  [36]. We see in the Figure that SCIE and HMSA results closely agree, and appear slightly delayed with respect to the MC datum [43]; also, theories predict a sharp increase of  $S(q_c)$  whereas MC shows a more rounded growth of this property. Since  $S(q = 0)$  is roughly proportional to  $S(q_c)$  [8], also this property turns to discontinuously rise, as visible from Figure 3B; therein we see moreover that both SCIE and HMSA predict smaller jumps to occur also at  $\varepsilon_0$ .

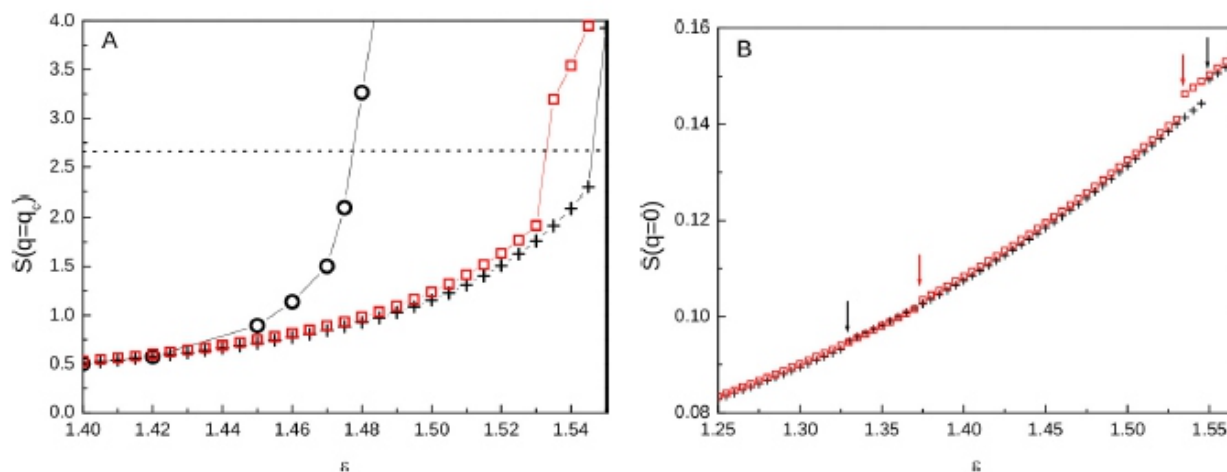


**Figure 3.**  $S(q_c)$  (A) and  $S(q = 0)$  (B) vs  $\varepsilon$ , as obtained by SCIE (crosses) and HMSA (squares). In (A) MC data [43] are also shown (circles); the dotted line represents the clustering threshold according to [35, 36]. In (B), arrows indicate  $\varepsilon_0$  and  $\varepsilon_t$  as predicted by both theories, whereupon jumps occur, witnessing successive rearrangements within the fluid as the attractive strength increases.

The moderate increase of compressibility witnesses the development of larger and larger density fluctuations, as the system progresses within an increasingly inhomogeneous arrangement, heralding the onset of clustering.

If we recall Eq 2, we conclude that structural rearrangements within the fluid taking place at  $\varepsilon_0$  and  $\varepsilon_t$  involve corresponding changes in the isothermal compressibility  $\chi_T$ . Based on all evidence reported so far, both in real-space and reciprocal-space, we conclude that the observed atypical reversal of trend in the pair correlation faithfully witnesses the onset of clustering. The overall phenomenology observed by MC simulations is positively reproduced by IETs.

In agreement with our MC results [43], refined IETs predict a discontinuity in  $S(q_c)$  at  $\varepsilon = \varepsilon_t$ . At this stage, an interesting issue concerns the origin, within the theoretical framework, of the observed discontinuities. Indeed, as seen in Figure 4, successive steps in the gain of inhomogeneity, observed at  $\varepsilon_0$  and  $\varepsilon_t$ , are marked by clear-cut jumps in the mixing parameter  $f$ . Consequently, it is the very fulfillment of the thermodynamic consistency condition (Eq 2) — enforced by any refined IET — that allows us to identify the observed structural changes. In the case  $f = 1$ , both SCIE and HMSA reduce to the thermodynamically inconsistent HyperNetted chain (HNC) approximation. We refer the reader to our recent work [44] for an extended analysis of HNC predictions concerning the HS2Y model of Eq 1 within various parameterizations including the one employed in this work. We simply note here that, consistently with the assumption of a constant  $f$  value, HNC is unable to capture the discontinuous changes in the structural properties documented by MC [43].

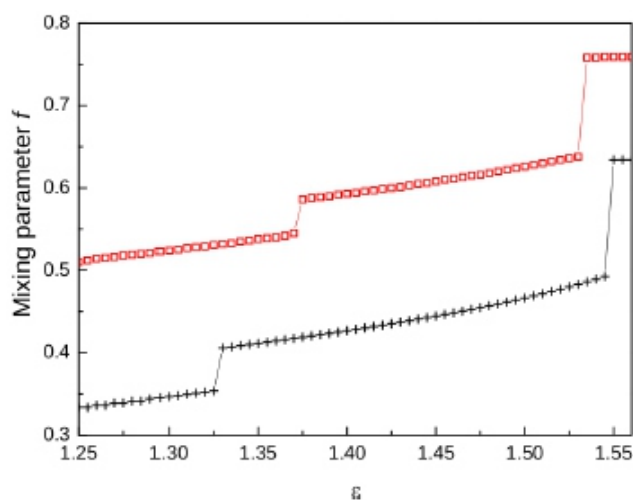


**Figure 4.** Mixing parameter  $f$  vs  $\varepsilon$  for SCIE (crosses) and HMSA (squares). When clustering is underway, inherent structural changes, occurring at  $\varepsilon_0$  and  $\varepsilon_t$ , are marked by clear-cut jumps in  $f$ . Lines are guides to the eye.

We finally turn to the pair entropy  $s_2$  of (Eq 3), a global property found to be a fingerprint to distinguish between liquid-like and solid-like environments on the one hand, and between different crystal structures on the other hand [57]. More generally, in simple liquids  $s_2$  decreases as the system becomes progressively more structured. As seen from Figure 5, this statement holds also for our model, during the clustering process. In fact, as  $\varepsilon$  increases, the formation of a further coordination shell contributes to the overall stabilization of the local environment around a given particle, provided by the existing shells of neighbours; as we have seen, this structural rearrangement abruptly triggers the clustering process, with the consequence that a drastic reduction of available configurational states affects all those particles forming aggregates. This mechanism is exactly reflected in the rapid, almost

discontinuous decrease of pair entropy visible in Figure 5. As  $\varepsilon$  increases, both structural rearrangements affecting  $h(x)$  at  $\varepsilon_0$  and  $\varepsilon_t$  have visible effects on  $s_2$ : a first discontinuity is followed, by further increasing the attractive strength, by a second discontinuous jump observed at  $\varepsilon = \varepsilon_t$  to be ascribed to the entropy change related to the onset of clustering. In a previous study [14], we identified a possible signature of the arising IRO peak in HS2Y models, as a jump in the entropy, based on chemical potential calculations [58–61]; therein, we surmised that the loss of available space within the clusters is tempered by a gain of accessible space between clusters, mitigating overall the decrease of the total entropy due to the decrease of the main contribution provided by  $s_2$ . In general, the search for thermodynamic signatures of clustering could greatly help our understanding of these systems, favouring as well our capability of experimentally identifying aggregation processes.

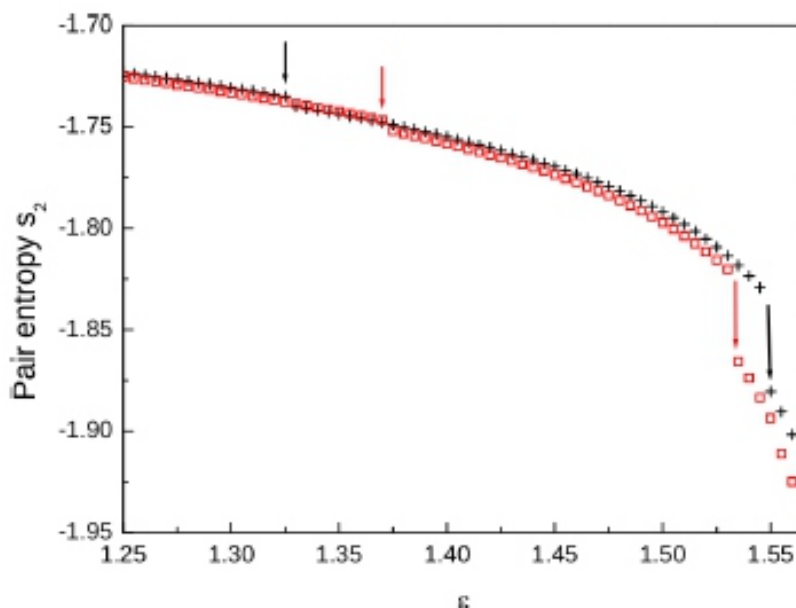


**Figure 5. SCIE (crosses) and HMSA (squares) pair entropy. Arrows indicate  $\epsilon_0$  and  $\epsilon_t$  as predicted by both theories, whereupon jumps occur, witnessing successive rearrangements within the fluid as the attractive strength increases.**

#### 4. CONCLUSION

Refined thermodynamically self-consistent integral equations are shown to reproduce a mechanism, previously unearthed by MC [43], governing the clustering process in a model SALR fluid. Refined IETs, designed a priori for the study of the liquid state, are able to capture the structure of such a system across the clustering threshold. In a previous study [14], we documented the existence of small simultaneous discontinuities of several thermodynamic and structural properties of the same pair potential (but within different parameterizations), under physical conditions close to the early development of an intermediate-range order in the fluid. In comparison, discontinuities presently observed when passing from an IRO to a clustered state are neater. We speculate that in model colloids with competing interactions, the present mechanism is a generic feature intrinsic to the clustering process.

Possibly due to the fact that the scale at which our effect shows up is rather small, this process was overlooked in other studies using the same HS2Y model with identical parameters, but for those we already published [43, 44]. As for the experimental side, the pair potential adopted in this work provides a reasonable description of dispersions of charged colloidal particles in the presence of a depletant, e.g. non-adsorbing polymer-coils, in which  $\epsilon$  is proportional to the polymer concentration, the radius of gyration governs  $z_a$ , and the parameters entering the long-range repulsion depend on the electrostatic properties of the mixture [62]. Hence, an experimental realization of our setup, to gauge our findings against, would consist of a colloidal suspension, where all chemical and physical conditions are held fixed, but for the concentration of the polymer, so as to control the depletion potential strength. Similarly to what observed for simulations, also in experiments the process could be difficult to be traced in the neighborhood of the fifth coordination shell. Nevertheless, this limitation could be overcome since we have preliminary evidence that, for lower densities, the formation of clusters is signaled by reversals of trend occurring at shorter distances, making them easier to be detected.

## ACKNOWLEDGMENTS

The authors wish to thank Prof. Jean-Pierre Hansen, Prof. L. Lloyd Lee and Prof. Gerhard Kahl for their advices on the manuscript and fruitful discussions. We gratefully acknowledge the computer time made available at the Pôle Messin de Modélisation et Simulation (PMMS) and within the PO-FESR 2007-2013 MedNETNA (Mediterranean Network for Emerging Nanomaterials) Project.

## Conflict of interests

All the authors declare no conflict of interest regarding the publication of this article.

## REFERENCES

- Hansen JP, McDonald IR (2013) *Theory of Simple Liquids*, 4th Eds., Amsterdam: Elsevier.
- Pini D, Jialin G, Parola A, et al. (2000) Enhanced density fluctuations in fluid systems with competing interactions. *Chem Phys Lett* 327: 209–215.
- Sear RP, Gelbart WM (1999) Microphase separation versus the vapor-liquid transition in systems of spherical particles. *J Chem Phys* 110: 4582–4588.
- Imperio A, Reatto L (2004) A bidimensional fluid system with competing interactions: spontaneous and induced pattern formation. *J Phys-Condens Mat* 16: S3769–S3791.
- Sciortino F, Mossa S, Zaccarelli E, et al. (2004) Equilibrium cluster phases and low-density arrested disordered states: the role of short-range attraction and long-range repulsion. *Phys Rev Lett* 93: 055701.
- Groenewold J, Kegel WK (2004) Colloidal cluster phases, gelation and nuclear matter. *J Phys- Condens Mat* 16: S4877–S4886.
- Campbell AI, Anderson VJ, van Duijneveldt JS, et al. (2005) Dynamical arrest in attractive colloids: the effect of long-range repulsion. *Phys Rev Lett* 94: 208301.
- Archer AJ, Wilding NB (2007) Phase behavior of a fluid with competing attractive and repulsive interactions. *Phys Rev E* 76: 031501.
- Archer AJ, Ionescu C, Pini D, et al. (2008) Theory for the phase behaviour of a colloidal fluid with competing interactions. *J Phys-Condens Mat* 20: 415106–415117.
- Toledano JCF, Sciortino F, Zaccarelli E (2009) Colloidal systems with competing interactions: from an arrested repulsive cluster phase to a gel. *Soft Matter* 5: 2390–2398.
- Lee LL, Hara MC, Simon SJ, et al. (2010) Crystallization limits of the two-term Yukawa potentials based on the entropy criterion. *J Chem Phys* 132: 074505.
- Costa D, Caccamo C, Bomont J-M, et al. (2011) Theoretical description of cluster formation in two-Yukawa competing fluids. *Mol Phys* 109: 2845–2863.
- Bomont JM, Costa D (2012) A theoretical study of structure and thermodynamics of fluids with long-range competing interactions exhibiting pattern formation. *J Chem Phys* 137: 164901–164911.
- Bomont JM, Bretonnet JL, Costa D, et al. (2012) Thermodynamic signatures of cluster formation in fluids with competing interactions. *J Chem Phys* 137: 011101.
- Sweatman MB, Fartaria R, Lue L (2014) Cluster formation in fluids with competing short-range and long-range interactions. *J Chem Phys* 140: 124508.
- Cigala G, Costa D, Bomont JM, et al. (2015) Aggregate formation in a model fluid with microscopic piecewise-continuous competing interactions. *Mol Phys* 113: 2583–2592.
- Bretonnet JL, Bomont JM, Costa D (2018) A semianalytical “reverse” approach to link structure and microscopic interactions in two-Yukawa competing fluids. *J Chem Phys* 149: 234907.
- Liu Y, Fratini E, Baglioni P, et al. (2005) Effective long-range attraction between protein molecules in solutions studied by small angle neutron scattering. *Phys Rev Lett* 95: 118102.
- Broccio M, Costa D, Liu Y, et al. (2006) The structural properties of a two-Yukawa fluid: Simulation and analytical results. *J Chem Phys* 124: 084501.
- Cardinaux F, Stradner A, Schurtemberger P, et al. (2007) Modeling equilibrium clusters in lysozyme solutions. *EPL (Europhys Lett)* 77: 48004.
- Liu Y, Porcar L, Chen J, et al. (2011) Lysozyme protein solution with an intermediate range order structure. *J Phys Chem B* 115: 7238–7247.
- Porcar L, Falus P, Chen WR, et al. (2010) Formation of the dynamic clusters in concentrated lysozyme protein solutions. *J Phys Chem Lett* 1: 126–129.
- Falus P, Porcar L, Fratini E, et al. (2012) Distinguishing the monomer to cluster phase transition in concentrated lysozyme solutions by studying the temperature dependence of the short-time dynamics. *J Phys-Condens Mat* 24: 064114.

24. Zhuang Y, Charbonneau P (2016) Recent advances in the theory and simulation of model colloidal microphase formers. *J Phys Chem B* 120: 7775–7788.
25. Liu Y, Xi Y (2019) Colloidal systems with a short-range attraction and long-range repulsion: phase diagrams, structures, and dynamics. *Curr Op Colloid In* 39: 123-136.
26. Bretonnet JL (2019) Competing interactions in colloidal suspensions. *AIMS Mat Sci* 6: 509-548.
27. Sweatman MB, Lue L (2019) The giant SALR cluster fluid: a review. *Adv Theory Simul* 2: 1900025.
28. Stradner A, Sedgwick H, Cardinaux F, et al. (2004) Equilibrium cluster formation in concentrated protein solutions and colloids. *Nature* 432: 492–495.
29. Baglioni P, Fratini E, Lonetti B, et al. (2004) Structural arrest in concentrated cytochrome C solutions: the effect of pH and salts. *J Phys-Condens Mat* 16: S5003–S5022.
30. Lonetti B, Fratini E, Chen SH, et al. (2004) Viscoelastic and small angle neutron scattering studies of concentrated protein solutions. *Phys Chem Chem Phys* 6: 1388–1395.
31. Bomont JM, Bretonnet JL, Costa D (2010) Temperature study of cluster formation in two-Yukawa fluids. *J Chem Phys* 132: 184508.
32. Shukla A, Mylonas E, Di Cola E, et al. (2008) Absence of equilibrium cluster phase in concentrated lysozyme solutions. *PNAS* 105: 5075–5080.
33. Stradner A, Cardinaux F, Egelhaaf SU, et al. (2008) Do equilibrium clusters exist in concentrated lysozyme solutions? *PNAS* 105: E75.
34. Shukla A, Mylonas E, Di Cola E, et al. (2008) Reply to stradner et al.: equilibrium clusters are absent in concentrated lysozyme solutions. *PNAS* 105: E76.
35. Godfrin PD, Castaneda-Priego R, Liu Y, et al. (2013) Intermediate range order and structure in colloidal dispersions with competing interactions. *J Chem Phys* 139: 154904.
36. Godfrin PD, Wagner HJ, Liu Y, et al. (2014) Generalized phase behavior of cluster formation in colloidal dispersions with competing interactions. *Soft Matter* 10: 5061–5071.
37. Dzugutov M (1996) A universal scaling law for atomic diffusion in condensed matter. *Nature* 381: 137–139.
38. Dzugutov M, Sadigh B, Elliot SR (1998) Medium-range order in a simple monatomic liquid. *J Non-Cryst Solids* 232–234: 20–24.
39. Riest J, Nagele G (2015) Short-time dynamics in dispersions with competing short-range attraction and long-range repulsion. *Soft Matter* 11: 9273–9281.
40. Godfrin PD, Hudson SD, Hong K, et al. (2015) Short-time glassy dynamics in viscous protein solutions with competing interactions. *Phys Rev Lett* 115: 228302.
41. Hansen JP, Verlet L (1969) Phase transitions of the Lennard–Jones system. *Phys Rev* 184: 151–161.
42. Jadrlich RB, Bollinger JA, Johnson KP, et al. (2015) Origin and detection of microstructural clustering in fluids with spatial-range competitive interactions. *Phys Rev E* 91: 042312.
43. Bomont JM, Costa D, Bretonnet JL (2017) Tiny changes in local order trigger the cluster formation in model fluids with competing interactions. *Phys Chem Chem Phys* 19: 15247–15256.
44. Bomont JM, Costa D, Bretonnet JL (2020) Local order and cluster formation in model fluids with competing interactions: a simulation and theoretical study. *Phys Chem Chem Phys* 22: 5355–5365
45. Pini D, Parola A, Reatto L (2006) Freezing and correlations in fluids with competing interactions. *J Phys-Condens Mat* 18: S2305–S2320.
46. Zerah G, Hansen JP (1986) Self-consistent integral equations for fluid pair distribution functions: another attempt. *J Chem Phys* 84: 2336–2343.
47. Bomont JM, Bretonnet JL (2003) A self-consistent integral equation: bridge function and thermodynamic properties for the Lennard–Jones fluid. *J Chem Phys* 117: 114112.
48. Bomont JM, Bretonnet JL (2004) A consistent integral equation theory for hard spheres. *J Chem Phys* 121: 1548–1552.
49. Bomont JM (2008) Recent advances in the field of integral equation theories: bridge functions and applications to classical fluids. *Adv Chem Phys* 139: 1–83.
50. Labik S, Malijevski A, Vonka P (1985) A rapidly convergent method of solving the OZ equation. *Mol Phys* 56: 709–715.
51. Kikuchi R (1951) A theory of cooperative phenomena. *Phys Rev* 81: 988–1003.
52. Green S (1952) *The Molecular Theory of Fluids*, Amsterdam: Elsevier.
53. Nettleton RE, Green M (1958) Expression in terms of molecular distribution functions for the entropy density in an infinite system. *J Chem Phys* 29: 1365–1370.
54. Baranyai A, Evans DJ (1989) Direct entropy calculation from computer simulation of liquids. *Phys Rev A* 40: 3817–3822.
55. Wallace DC (1987) On the role of density fluctuations in the entropy of a fluid. *J Chem Phys* 87: 2282–2284.
56. Laird BB, Haymet A (1992) Calculation of the entropy from multiparticle correlation functions. *Phys Rev A* 45: 5680–5689.

57. Piaggi PM, Parrinello M (2017) Entropy based fingerprint for local crystalline order. *J Chem Phys* 147: 114112.
58. Bomont JM (2003) Excess chemical potential and entropy for pure fluids. *J Chem Phys* 119: 11484–11486.
59. Bomont JM, Bretonnet JL (2003) A new approximative bridge function for pure fluids. *Molec Phys* 101: 3249–3261.
60. Bomont JM (2006) A consistent calculation of the chemical potential for dense simple fluids. *J Chem Phys* 124: 206101.
61. Bomont JM, Bretonnet JL (2007) Approximative "one particle" bridge function  $B(1)(r)$  for the theory of simple fluids. *J Chem Phys* 126: 214504.
62. Israelachvili JN (2011) *Intermolecular and Surface Forces*, 3rd Eds., Amsterdam: Elsevier.



# Evolution of Intermetallic Compounds in Ti–Al–Nb System by the Action of Mechanoactivation and Spark Plasma Sintering

Yernat Kozhakhmetov<sup>1,\*</sup>, Mazhyn Skakov<sup>2</sup>, Wojciech Wieleba<sup>3</sup>, Kurbanbekov Sherzod<sup>4</sup>, and Nuriya Mukhamedova<sup>2</sup>

<sup>1</sup>D. Serikbayev EKSTU, KZ-070000 Ust-Kamenogorsk, Kazakhstan

<sup>2</sup> National Nuclear Center of the Republic of Kazakhstan, KZ-071100 Kurchatov, Kazakhstan

<sup>3</sup> Wroclaw University of Science and Technology, PL-50-370 Wroclaw, Poland

<sup>4</sup> H.A. Yassawi International Kazakh-Turkish University, KZ-161200 Turkistan, Kazakhstan

\* Correspondence: Email: kozhahmetov\_e@nnc.kz; Tel: +77751316886.

## ABSTRACT

The present study shows promising approach to produce hydrogen-accumulated rechargeable intermetallic compounds (IMC) from three-component powder composition Ti–25Al– 25Nb (at%), through experimentally chosen best modes and combined technological processes. The study includes research results on the effect of mechanoactivation (MA) process and following spark plasma sintering (SPS) technique on structural phase state of intermetallic Ti–Al–Nb composites. It was revealed that upon activation of the initial powder mixtures during their machining, intermetallic phases are formed by the interpenetration of aluminum into titanium and niobium lattices with the formation of solid solutions (Ti, Al) and (Nb, Al). It is found out, that the combination of MA and SPS is good for producing fine-graded predicted micro-structures in Ti–Al–Nb system owing to the activation of particle surface and formation of intermetallic phases at the preparation stage of powder mixture using MA technique as well as due to the effect of fast consolidation using SPS. This points to the fact of prospect for creating metal hydrides by combining MA and SPS techniques that makes it possible to obtain fine-grained IMC containing fair amount of O-phase.

**Keywords:** intermetallic compounds; Ti–25Al–25Nb alloy; spark plasma sintering; mechanoactivation; O-phase

## 1. INTRODUCTION

So far, efforts are underway to study IMC based on titanium aluminides with high content of Niobium. Ti<sub>2</sub>AlNb-based materials belong to the third generation of titanium aluminides and have an orthorhombic basocentric crystal lattice. A wide homogeneity range of these intermetallics confers the possibility to produce the materials with different chemical composition. Intermetallic Ti–Al–Nb composites own interesting structural properties; they are hydride-forming and are able to absorb hydrogen extensively that provides them with a significant advantage while using them as hydrogen storage materials [1,2].

Low density, safety and wide distribution of these elements make them especially attractive. However, at the moment one of the main problems of the development of this direction is the lack of reliable manufacturing technology for producing the Ti<sub>2</sub>AlNb-based IMC, which could provide the best properties depending on the purpose. The present study showed that structural-phase state and physical-mechanical properties of Ti<sub>2</sub>AlNb-based IMC can be controlled directly by the production technology [3,4].

The application of the MA technique at the stage of powder mixture preparation creates active states in a solid body, opening a certain prospect for subsequent conducting and accelerating chemical reactions between the solid bodies and producing materials in a high-equilibrium state. Activation of solids bodies in the course of their mechanical processing by grinding in shock, shock-abrasion or abrasion modes leads to the accumulation of structural defects, increase in curvature and surface area, phase transformations and even amorphization of crystals, thus affecting their chemical activity [5,6].

At the same time, during the last decade there were published a number of studies considering the application of powder sintering technique in spark plasma [7]. Short-term high-temperature effect on powder mixture, optimal ratio of heating and deformation modes of the material, as well as the way of electric current through the powder mixture allow to obtain high-strength materials characterized by a fine-grained structure, low porosity and low mechanical stresses [8,9]. New composites with best properties might be produced in case of realization of this technology.

As reviewed above, the combination of MA and SPS techniques can strike out in an original direction of consolidation of Ti–Al–Nb alloys. Few research works have experienced in this issue, so the effect of sintering process on the structure, phase state and physical and mechanical properties of Ti–Al–Nb alloys should be investigated further. The effect of MA on the process of consolidation of powder mixture is also reasonably to study.

This study aims and focuses on the effect of preliminary MA and subsequent SPS on the structural-phase state of intermetallic compound in the Ti–Al–Nb composite.

## 2. MATERIALS AND METHODS

The studied intermetallic compounds in the Ti–25Al–25Nb composite (at%) have been produced through the combination of two techniques: MA and SPS. Titanium powder with particle size of 45–60  $\mu\text{m}$ , Niobium powder with particle size of 40–63  $\mu\text{m}$ , and Aluminum powder were used as a reference material. Aluminum powder of different dispersity and morphology were used in order to assess the impact of the properties of the initial powder on the final product:

- Aluminum nanopowder with fuzzy-edged particles of ~90–250 nm. The powder is heavy agglomerated.
- Aluminum powder is characterized with quite different size of the particles from 50 to 60  $\mu\text{m}$ . The particles are mostly globular.
- The particles of aluminum chips have compacted and dominant sponge structure. Size of the aluminum chips' particles is in the range of 100–150  $\mu\text{m}$ .

The powders were mixed up in a P100CM planetary mill at the ratio of the masses of molding bodies with a diameter of 10 mm to the processed material as 23:1 than they were subjected to the MA. Table 1 provides details of the MA.

**Table 1. Details of the MA.**

	Materials	Duration (min)	Rotation velocity (rpm)	Changing the direction of rotation of the planetary disk (min)	Testing environment	The degree of grinding Al in the initial mixture
Mixin	Ti–Al–Nb	35	250	–	Argon	
MA	Ti–Al–Nb mixture	20	650	–	Argon	Nanopowder
	Ti–Al–Nb mixture					Powder
	Ti–Al–Nb mixture					Shavings
	Ti–Al–Nb mixture	180	350	every 30		

The morphology and particle size distribution of mechanically activated powders, as well as the microstructure and elemental composition of the obtained IMC were studied in the topographic and compositional contrast mode using scanning electron microscope TescanVega3 with the addition of energy dispersion spectral analysis. X-ray phase analysis (XPA) of studied materials was performed in X-ray diffractometer Empyrean in Cu-K $\alpha$  radiation. Ready diffractograms were processed in the HighScore program.

The SPS of powder mixtures was carried out in the vacuum (10–5 Pa) in SPS-515S machine (SyntexInc., Japan). The powder mixture was consolidated under the temperature of 1300 °C, static pre-pressing pressure of 20 MPa and isothermal exposure for 5 min.

Integrated video cameras recorded some changes in linear dimensions of ceramic material in the course of the sintering process. A high-temperature pyrometer, built-in a technological hole in the side wall of the mold, measured the temperature in the course of the sintering process which ranged from 575 to 2500 °C.

### 3. RESULTS AND DISCUSSIONS

#### 3.1. Mechanoactivation

Detailed analysis of the radiographs of powder mixture after MA has shown it is quite complicate to identify phase composition because of the overlapping most strong lines of the phases.

However, when the MA process lasted for 20 min, regardless the size of their aluminum particles, each powder mixture showed the main peaks of single elements like Ti, Al and Nb. This justifies that the mixture contains unreacted particles.

According to the analysis results of diffractograms  $\alpha$ -Ti with hexagonal crystal lattice of the spatial group P63/mmc, Nb with a body-centered cubic lattice (bcc) of the spatial group Im3m, Al with a cubic lattice, the spatial group Fm-3m are common phases for the composition of samples of all powder mixtures. Figure 1 shows the overlapping of diffractograms of powder mixture Ti–Al–Nb.

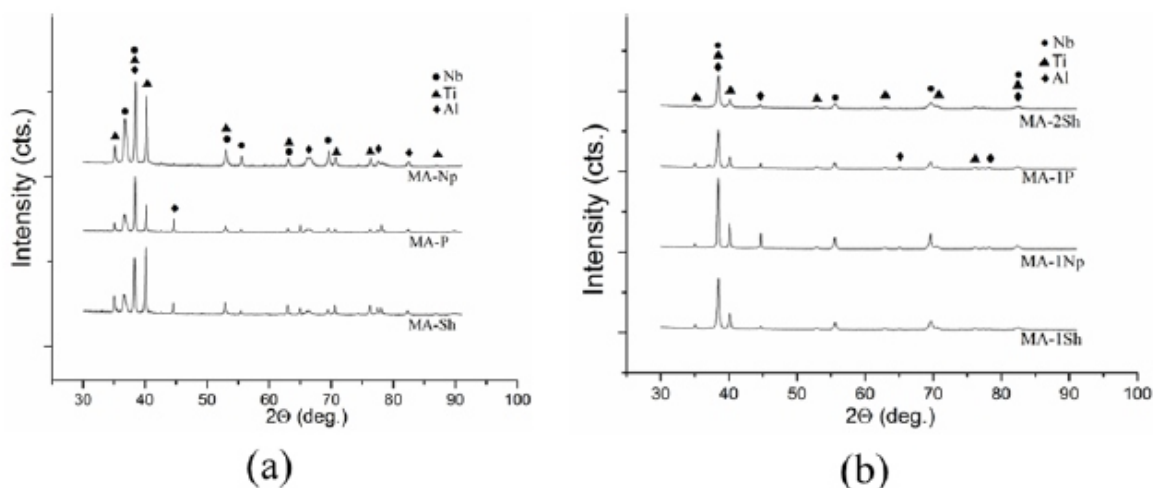


**Figure 1. Diffraction pattern of the mixture Ti–Al–Nb: (a) in the initial state, (b) after MA in different modes.**

While studying diffractograms it was stated that intensity line and width of peaks depend on the MA process and size of aluminum particles. Maximum intensity of peaks of aluminum phase after the MA process is observed on the diffractograms of MA-1Np mixture, whereas the opposite effect is observed for MA-1P mixture: diffraction peaks Ti, Al and Nb decreased in intensity and expanded in width. The same case is typical for MA-2Sh powder mixture after 180 min since the MA has started.

Sim et al. [10] studied that this is due to the process of synthesis of metastable supersaturated solid solutions by mixing elementary powders at MA powder mixture of Ti–Al–Nb system. Therefore, after the MA process, when using MA-1P mixture for 20 min and MA-2Sh mixture for 180 minutes, most of aluminum particles were dissolved in the lattice Ti and Nb by interpenetration with formation solid solutions (Ti, Al) and (Nb, Al). In addition, Mukhamedova et al. [11] studied that in the process of sample preparation by the MA technique the orthorhombic phase  $Ti_2AlNb$  is also formed and by increasing of MA duration the composition of this phase will only raise [12].

Scanning electron microscopy of mechanically activated powder mixtures in the topographic and compositional contrast mode showed that as a result of multiple effects of cold welding of Al, Ti, Nb and destruction we can observe formation of layered composite particles. In case of using MA-1Np mixture with aluminum nanopowder after treatment for 20 min (Figure 2a) there is a sticking of aluminum on titanium and niobium particles, without formation of solid solution, that explains maximum intensity of peaks of aluminum phase after MA.

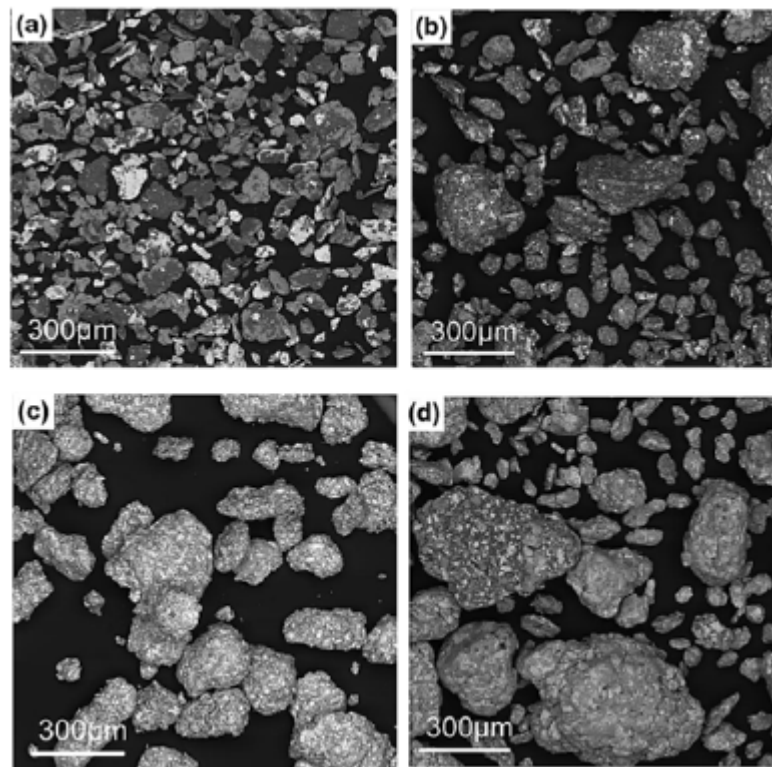


**Figure 2. SEM image of Ti–25Al–25Nb (at%) alloy powder particles after MA: (a) sample MA-1Np, (b) sample MA-1P, (c) sample MA-1Sh, and (d) sample MA-2Sh.**

It was found that after MA, the powder particles become inhomogeneous and polyhedral-shaped. With extending time of the MA process we can observe a gradual transformation of the particle shape into a spherical one that is mainly characterized for small particles. Figure 3 and Table 2 show results of EDS analysis of particle's local regions after cold welding effect.

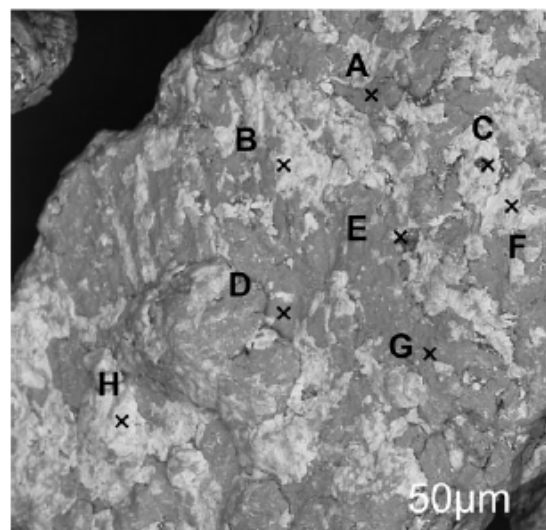


**Figure 3. SEM image and EDS analysis of particle of powder mixture MA-2Sh after MA for 180 min.**

**Table 2. Results of local element analysis of powder mixture MA-2Sh in weight shares.**

Title	Al	Ti	Nb	Title	Al	Ti	Nb
A	13.06	71.20	15.75	E	76.14	7.20	16.66
B	6.37	4.30	89.33	F	6.22	11.82	81.96
C	70.11	9.16	20.73	G	11.05	81.02	7.93
D	6.65	88.53	4.82	H	16.58	28.26	55.16

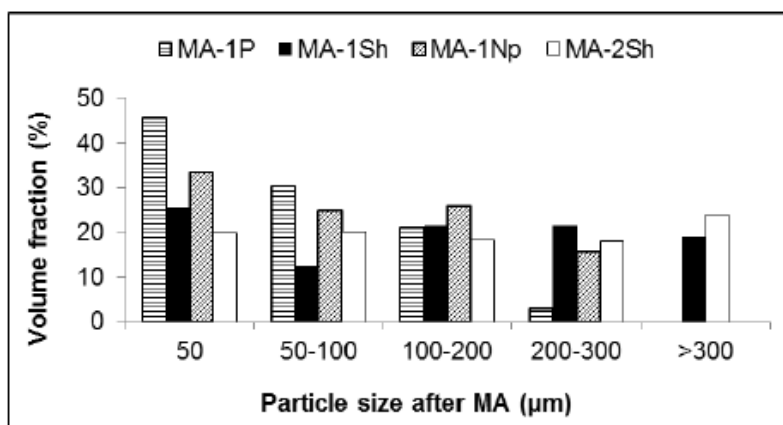
As can be seen in Figure 3, regions with a dark grey tint are typical for areas with high titanium content, whereas the areas of light gray tint are typical for the regions with high content of niobium.

According to the results of EDS-analysis of local points, it can be said that the fractions of powder mixtures are inhomogeneous in each single particle and consist of areas enriched or depleted with titanium and niobium. In this case, aluminum is almost completely dissolved, except of some local areas. At the same time, composition of predominant and secondary initial components varies in a wide range of values.

Nowadays it has been inferred that characteristics of the feedstock mostly determine microstructure, phase composition and operating properties of sintered solid alloys and intermetallic compounds. Many researchers have introduced studies on the effect of characteristics of initial powders on the structure and properties of solid alloys [13]. Morphology and size of particles of powder mixture of Ti–Al–Nb system directly impact on the structure and operating properties of producing material while their consolidation. This is due to nonequilibrium and chemical inhomogeneity of poly-phase particles as well as diffusion velocity while sintering.

The analysis of particle size showed that particles are randomly distributed throughout the mixture (Figure 4). Such distribution is caused by multiple plastic deformations of particles, their cyclic conglomeration and destruction that results in increase of small and large fractions after MA process. As can be seen in Figure 3, powder mixtures with aluminum chips MA-1Sh and MA-2Sh with a particle size of more than 100  $\mu\text{m}$  are the most susceptible to particle conglomeration.

Fractions with size of more than 300  $\mu\text{m}$  are not detected for a mixture using aluminum powder and nanopowder herewith. It is seen, that particle conglomeration depends on duration of MA process because constant activation of particle surface takes place with increasing MA time that, in turn, leads to cold welding of these particles.

**Figure 4. Distribution of particles on sizes after MA process.**

### 3.2. Microstructural research of intermetallic Ti–Al–Nb composites by combining of MA and SPS techniques

The temperature of SPS was experimentally identified according to the phase diagram of Ti–Al–Nb system. Samples sintered under the temperature of 1300 °C are characterized by a homogeneous multiphase structure consisting of intermetallic Ti<sub>3</sub>Al, AlNb<sub>2</sub>, B2 and O-phases, without pores and cracks. The characteristic structure of sintered samples and the results of local elemental analysis are shown in Figure 5 and Table 3.

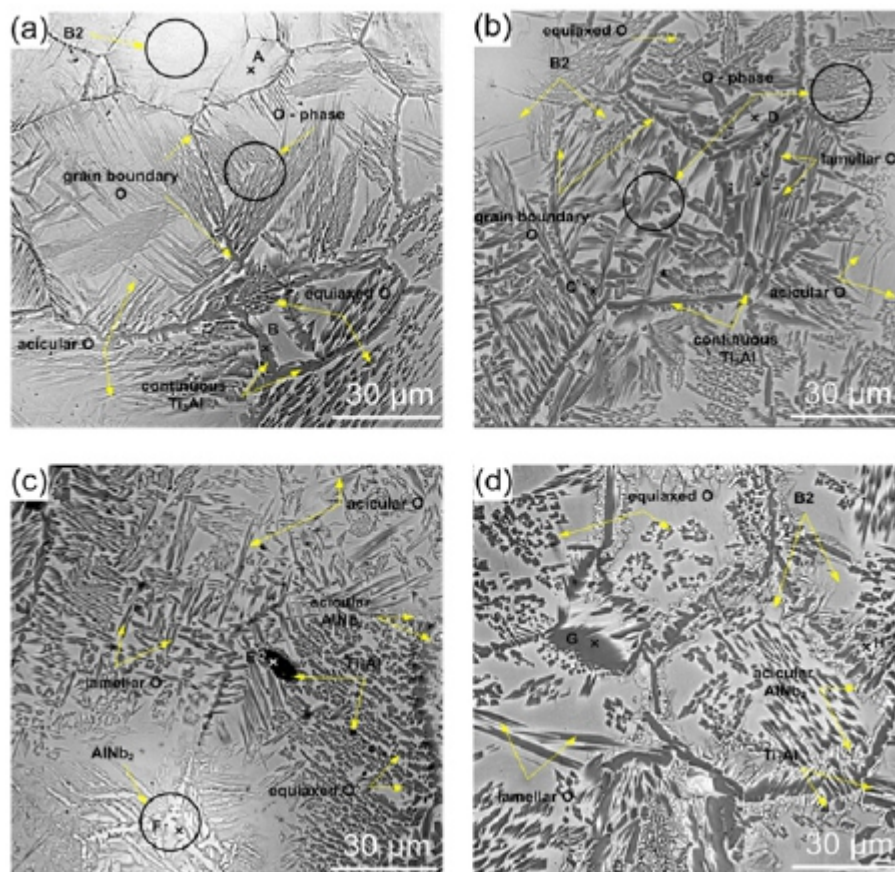


**Figure 5.** SEM image and XPA of samples based on Ti–25Al–25Nb system (at%) after SPS under 1300 °C/5 min/20 MPa: (a) sample MA-2Sh, (b) sample MA-1P, (c) sample MA-1Np, and (d) sample MA-1Sh.

**Table 3.** Results of local element analysis of IMC samples after SPS in weight shares.

Title	Al	Ti	Nb	Phase	Title	Al	Ti	Nb	Phase
A	15.87	56.37	27.75	B2	E	22.08	68.55	9.37	Ti <sub>3</sub> Al
B	25.83	51.03	23.14	O	F	13.62	19.50	66.89	AlNb <sub>2</sub>
C	13.96	57.38	28.66	Ti <sub>3</sub> Al	G	28.14	50.42	21.44	O
D	29.52	58.47	12.02	B2	H	13.01	19.25	67.74	AlNb <sub>2</sub>

Review of microstructure of sintered samples under the temperature of 1300 °C revealed noticeable changes in distributions and in the contents of the main phases. This is evidenced by the images of the surface of the samples obtained by the SEM method. Figure 5 shows SEM images of Ti–25Al–25Nb alloys (at%). It is seen that in the samples, sintered under the temperatures of 1300 °C, almost complete diffusion of unreacted Niobium and titanium occurs, while the grain boundaries of B2 phase are

noticeably enlarged on all samples. This is probably due to the decay of most part of Ti<sub>3</sub>Al phase, which is forming in the course of the sintering. It likely seems that at the sintering stage, the niobium element quickly diffuses and penetrates the intergranular boundary of Ti<sub>3</sub>Al, and the phases with a large average size of Ti<sub>3</sub>Al are broken into many small globular particles and deposited at the boundaries of B2 phase [14]. In addition, Niobium and Aluminum occupy Ti positions in B2 phase and form O-phase at the grain boundaries. Thus, the microstructure of the samples under the given temperature consists mainly of the B2 + O phase, and composition becomes more homogeneous. However, as can be seen in Figures 5b,c at the grain boundaries of B2 phase, there are still intermittent globular deposition and long aligned Ti<sub>3</sub>Al phase bars, which are located parallel to the grain boundary of B2.

It is worth noting that distribution of AlNb<sub>2</sub> phase on the surface of the samples while sintering under the temperature of 1300 °C led to the formation of a coarse-crystalline dendritic structure for this phase. AlNb<sub>2</sub> phase distribution has two features. The main part of particles are plate-shaped and look like needles up to 5 μm thick and 20–25 μm long in the field of metallographic sections and located mainly at the triple joints of B2 phase (Figure 5c), and grow as needles into the grain bodies and B2 phase boundaries. We also can observe accumulation of this phase in the form of short needlelike inclusions distributed throughout the diameter of B2 grains (Figure 5d), which create a barrier with a thickness of 4–5 μm between the main B2 phase and boundary O-phase.

If the first type of distribution of AlNb<sub>2</sub> phase is typical for all samples, the second type is mostly related to sample MA-1Sh. It might be due to short-term technological processes (MA and SPS) and worse diffusion feature. Residual niobium in powder mixture MA-1Sh cannot complete reactive diffusion and deposit as AlNb<sub>2</sub> phase.

As shown from Figure 5, microstructure of samples under this sintering temperature is characterized by the presence of plate-like structure of O-phase 10–25 μm long and 5–6 μm thick. At the same time there are globular accumulations of O-phase from 2 to 5 μm in some areas. O-phase distribution depends on the size of Al particles in the initial burden and pre-Ma modes. For example, MA-1Sh sample is characterized by globular accumulation of O-phase in the grain body of B2 phase which sizes vary widely. MA-1P and MA-1Np samples are characterized by wide lamellar structure and globular accumulation of O-phase sized less than 2 μm. It should be emphasized that these two types of O-phase can be found in separate B2 phase grains and at the same time can be combined in one B2 phase grain matrix. MA-2Sh sample, where MA process was carried out for 180 minutes, differs from other samples by the absence of above mentioned types of O-phase distribution, and it is characterized by the presence of lamellae in the grain body, which are located perpendicular to the grain boundaries of B2 phase and have different lengths and widths. Changes in the volume fractions of the O-phase between different samples are shown in Figure 6. As can be seen from the Figure, while SPS under the temperature of 1300 °C, B2-phase and O-phase are the main ones for all samples, at the same time there is a small amount of Ti<sub>3</sub>Al-phase. Identifying of the volume fraction of AlNb<sub>2</sub>-phase was difficult due to their small content and local distribution. The O-phase content for all samples is the highest in comparison with other phases and reaches a maximum on the MA-2Sh sample at a value of 50.92%. This dependence of O-phase is typical for all samples regardless of particle size and MA duration. This indicates that the O-phase is rapidly precipitated from B2 and Ti<sub>3</sub>Al phases.

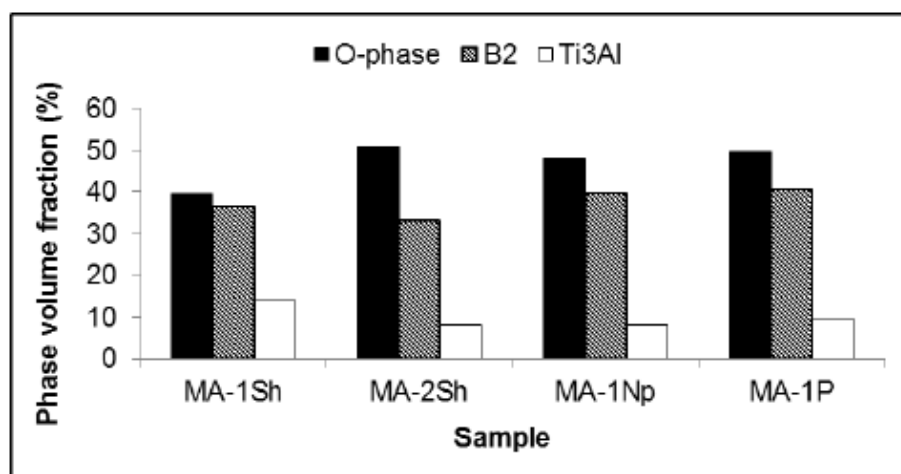


**Figure 6. Changes of volume share of O-phase in samples depending on particle size and MA duration.**

Longer duration of the MA has positive impact on IMC structure especially on the formation of O-phase. Increase in time of MA for MA-2Sh sample led to more homogeneous distribution of O-phase which characterized with fine texture of lamellae, whereas the samples obtained after 20 min since MA has started are more heterogeneous. This is due to the formation of solid solution BCC (Ti, Al, Nb) and its increased content because of longer MA.

#### 4. CONCLUSION

##### The following conclusions were made throughout this work:

- Intermetallic phases are evolving in the process of MA of initial powder mixtures due to aluminum penetration in the Ti and Nb grids and owing to formation of solid solutions (Ti, Al) и (Nb, Al);
- Extending time of MA gives positive effect on the structure of new intermetallic compounds. This is due to formation of solid solution BCC (Ti, Al, Nb) and its increased content while the time extending of the MA;
- By combining MA and SPS processes it is able to monitor structural-phase state of the final product. For example, MA-1Sh specimen is characterized by globular accumulations of O-phase in the body of the grain of B2-phase. Specimens MA-1P and MA-1Np are characterized by lamellar structure and globular accumulation of O-phase no more than 2  $\mu\text{m}$ . Specimen MA-2Sh, where MA lasted for 180 min, differs from other specimens because it hasn't above characteristics with more homogenous distribution of lamellae of O-phase in the body of the grain of B2-phase located up-and-down the boundaries of the grains;
- Lastly through the conclusions as mentioned above, it was proved that the combination of MA and SPS techniques makes it possible to produce fine-grained predicted microstructures in Ti–Al–Nb system. This is due to the activation of particle surface and the formation of intermetallic phases at the preparatory stage of powder mixture using MA as well as due to rapid consolidation reached by SPS. This is promising direction to produce metal hydrides using MA and SPS in order to obtain fine-grained IMC with required amount of O-phase.

## Acknowledgments

The work has been implemented within the framework of the scientific and technical program “Development of nuclear energy in the Republic of Kazakhstan for 2018-2020” on the theme “Study of advanced materials based on Ti–Al–Nb system for hydrogen storage and transportation”.

## Conflict of interests

The authors declare that there is no conflict of interests regarding the publication of this paper.

## REFERENCES

1. Polozov I, Sufiiarov V, Kantyukov A, et al. (2019) Selective laser melting of Ti2AlNb-based intermetallic alloy using elemental powders: effect of process parameters and post-treatment on microstructure, composition, and properties. *Intermetallics* 112: 106554.
2. Karakozov BK, Skakov MK, Kurbanbekov SR, et al. (2018) Structural and phase transformations in alloys during spark plasma sintering of Ti + 23.5 at% Al + 21 at% Nb powder mixtures. *Inorg Mater* 54: 37–41.
3. Niu HZ, Chen YF, Zhang DL, et al. (2016) Fabrication of a powder metallurgy Ti2AlNb-based alloy by spark plasma sintering and associated microstructure optimization. *Mater Design* 89: 823–829.
4. Appel F, Clemens H, Fischer FD (2016) Modeling concepts for intermetallic titanium aluminides. *Prog Mater Sci* 81: 55–124.
5. Luo L, Liu T, Li K, et al. (2016) Microstructures, micro-segregation and solidification path of directionally solidified Ti–45Al–5Nb alloy. *China Foundry* 13: 107–113.
6. Wu J, Xu L, Lu Z, et al. (2015) Microstructure design and heat response of powder metallurgy Ti2AlNb alloys. *J Mater Sci Technol* 31: 1251–1257.
7. Maniere C, Lee G, Olevsky EA (2017) All-materials-inclusive flash spark plasma sintering. *Sci Rep* 7: 15071.
8. Bauri R, Chaudhari R (2014) Microstructure and mechanical properties of titanium processed by spark plasma sintering (SPS). *Metallogr Microst Anal* 3: 30–35.
9. Chen X, Xie FQ, Ma TJ, et al. (2015) Microstructure evolution and mechanical properties of linear friction welded Ti2AlNb alloy. *J Alloy Compd* 646: 490–496.
10. Sim K, Wang G, Son R, et al. (2017) Influence of mechanical alloying on the microstructure and mechanical properties of powder metallurgy Ti2AlNb-based alloy. *Powder Technol* 317: 133–141.
11. Mukhamedova NM, Kozhakhmetov YeA, Skakov MK, et al. (2019) Effect of mechanoactivation on the formation of O-phase in Ti–Al–Nb system. *Bulletin KazNITU* 5: 115–120.
12. Salvo C, Chicardi E, Garc a-Garrido C, et al. (2019) The influence of mechanical activation process on the microstructure and mechanical properties of bulk Ti2AlN MAX phase obtained by reactive hot pressing. *Ceram Int* 45: 17793–17799.
13. Voisin T, Monchoux JP, Couret A (2019) Near-net shaping of titanium–aluminum jet engine turbine blades by SPS, In: Cavaliere P, Spark Plasma Sintering of Materials: Advances in Processing and Applications, Cham, Switzerland: Springer, 713–737.
14. Kurbanbekov ShR, Skakov MK, Baklanov VV, et al. (2017) Effect of spark plasma sintering temperature on structure and phase composition of Ti–Al–Nb based alloys. *Mater Test* 59: 1033–1036.

# Microstructures, Mechanical Properties, and Corrosion Behavior of Novel Multi-Component Ti-6Mo-6Nb-xSn-xMn Alloys for Biomedical Applications

Cahya Sutowo<sup>1</sup>, Galih Senopati<sup>2</sup>, Andika W Pramono<sup>2</sup>, Sugeng Supriadi<sup>3</sup> and Bambang Suharno<sup>1,\*</sup>

<sup>1</sup> Department of Metallurgy and Material Engineering, Faculty of Engineering Universitas Indonesia, Depok 16424, Indonesia

<sup>2</sup> Research Center for Metallurgy and Materials Indonesian Institute of Sciences Tangerang Selatan 15314, Indonesia

<sup>3</sup> Department of Mechanical Engineering, Faculty of Engineering, Universitas Indonesia, Depok 16424, Indonesia

\* Correspondence: Email: suharno@metal.ui.ac.id; Tel: +62217863510.

## ABSTRACT

In this study, novel multi-component Ti-Mo-Nb-Sn-Mn alloys were developed as a solution to the mismatch in elastic moduli of implant and human bone and toxicity of the Ti-6Al-4V alloy commonly used in the biomedical field. This study is aimed to investigate the effects of Sn and Mn addition as beta stabilizers on the microstructural transformation, mechanical properties, and corrosion behavior of the alloys. Ti-6Mo-6Nb-xSn-xMn (x = 0, 4, or 8) alloys were re-melted five times in an arc re-melting process under an argon atmosphere and the obtained ingots were characterized using optical microscopy, X-ray diffractometry, ultrasound, a Vicker's hardness tester, and polarization tests in a Ringer solution. The results show that a Ti-6Mo-6Nb-xSn-xMn alloy had a lower elastic modulus and better corrosion resistance than those of commercial Ti-6Al-4V alloy, making it a potential candidate for use in the biomedical field.

**Keywords:** multi-component beta alloy; Ti-6Mo-6Nb-xSn-xMn; elastic modulus; corrosion resistance

## 1. INTRODUCTION

Although scientific developments and economic growth of a country generally lead to an improvement in the quality of life of its population [1], they may also have a negative impact. For instance, there is an increased need for implant materials that can be used to replace failed body tissues to improve the quality of life of the patients requiring the implant. Around 70–80% of the implants used in the biomedical field are made from metallic materials [2], which have been the case since the beginning of the industrial revolution in the 19th century [3], and these material are now widely used in orthopedic devices such as bone plates, pins, screws, and total joint replacements [4]. Due to their high strength and toughness under loading conditions, metallic implants have better properties than other implant materials, such as ceramics and polymers [5]. However, metallic implants are sometimes toxic and lack corrosion resistance [6]. Compared with metallic materials such as cobalt alloys and steel, titanium shows better corrosion resistance and biocompatibility with the human body [7,8]. Ti-6Al-4V alloy has been widely used in the biomedical fields due to its highly specific strength, good corrosion resistance and biocompatibility [9].

Vanadium has been reported as having cytotoxic effects in the human body, and aluminum is thought to contribute toward Alzheimer's disease [10]. Moreover, the large difference in the elastic modulus of human bone and Ti-6Al-4V may result in a stress shielding effect and, thus, promote implant failure [11]. Stress shielding is a phenomenon that takes place when the load in the area of the implanted material is entirely supported by the implant material, so that the bones around the implanted material are lack in nutrient intake [12]. When this happens over a long period of time, the bone around the area of the implant loses its mass, resulting in the failure of the implant due to the fragility of the surrounding bone [13].

The  $\beta$ -type titanium alloy has been developed with a lower elastic modulus than that of the Ti-6Al-4V alloy to reduce stress shielding effect [14]. The  $\beta$ -phase has been prepared via heat treatment, so it retains its full  $\beta$ -phase upon going from a high ( $\beta$ -phase field) to room temperature [15], which is possibly due to the addition of a sufficient amount of beta stabilizing elements to suppress the growth of  $\alpha'$  and  $\alpha''$  phases usually formed at room temperature [16–18]. In 1996, the first  $\beta$ -type titanium alloy, Ti-13Nb-13Zr, was developed by Mishra, with the later development of a  $\beta$ -type titanium alloy using the low-cost  $\beta$  stabilizing elements Mn, Sn, Fe, and Cr [19–21].

Lately, there has been focus on developing a non-toxic  $\beta$ -type titanium alloy with a low elastic modulus. So far, a  $\beta$ -type titanium alloy, Ti-Nb-Ta-Zr, has been found to have the lowest elastic modulus approaching that of human bone [22]. Gabriel developed a Ti-12Mo-3Nb alloy aimed at reducing the use of Ta and Nb, however, a relatively high elastic modulus of 105 GPa was achieved [23].

Some author stated that Sn is neutral element since it has no influence on both  $\alpha$  or  $\beta$  phase boundary. However, Morinaga stated that Sn and other element (O, Al, and Zr) can behave like  $\beta$  stabilizer. And from Mello's studies of Ti-Mo-Sn and Zhang studies of Ti-7.5Nb-4Mo-xSn reported that Sn has influence on suppressed  $\omega$  phase formation and could reduce the elastic modulus [16,24]. When 6% Sn was added to the Ti-8Mo alloy, the full beta-phase formed an elastic modulus of around 78 GPa [16]. Moreover, Santos also developed a beta titanium alloy containing Mn as a beta stabilizer known as a common alloying element. It was reported that at a Mn content of 9%, the lowest elastic modulus value was achieved at 94 GPa, and after this content, a full betaphase of the binary Ti-Mn alloy formed [25]. Several studies using cheap metal with a lower density did not result in the formation of a beta titanium alloy with an elastic modulus approaching that of a human bone. This study accommodates the use of titanium alloy with various combinations of low cost alloying elements (multi-components).

The addition of stannum and manganese, as both are low-cost elements, is to replace tantalum and reduce the use of niobium and molybdenum as beta-phase stabilizers. In this study, beta-phase titanium alloys were synthesized using Mo, Nb, Sn, and Mn as alloying elements, with the aim of determining the effects of adding Sn and Mn on a multi-component Ti-6Mo-6Nb-4Sn-xMn ( $x = 0, 4, \text{ or } 8 \text{ wt\%}$ ) and Ti-6Mo-6Nb-8Sn-xMn ( $x = 0, 4, \text{ or } 8 \text{ wt\%}$ ) alloys with respect to their phases, mechanical properties, and electrochemical properties in a Ringer solution.

## 2. MATERIALS AND METHODS

Multi-component  $\beta$ -type Ti-Mo-Nb-Sn-Mn (wt%) alloys were synthesized using Ti (99.9% pure), Nb (99.5% pure), Mo (99.5% pure), Sn (99.5% pure), and Mn (99.5% pure) from Nilaco Japan as raw materials. An arc melting furnace with a non-consumable tungsten electrode on a watercooled copper hearth was used to melt the alloys under an ultra-high purity argon atmosphere. Before melted in a

vacuum arc furnace, the raw materials were prepared by cutting them to the applicable sizes, cleaning them using volatile organic solvents, and subsequently weighing them according to the calculation of material balance, and loading them onto the top of a copper crucible in the melting chamber. The melting process took place under vacuum that is achieved by pumping the chamber up to the vacuum condition and subsequently draining it by argon, so that the melting chamber is free of oxygen. The ingots were re-melted five times to ensure the process had undergone completion rather than to improve their chemical homogeneity. The ingot was further homogenized by heating in a tube furnace with an argon atmosphere at 1150 °C for 6 h, followed by water quench cooling. The chemical compositions of the as-cast samples were examined by Rigaku X-ray fluorescence spectroscopy (XRF). The as-cast Ti–Mo–Nb–Sn–Mn was sectioned using an abrasive cutting wheel with dimensions of 2 cm X 2 cm X 1 cm. Samples for microstructure analysis were sanded on different 80–1500 grade SiC paper, polished with alumina paste, and etched using a solution of Kroll's reagent containing 2 mL HF + 6 mL of HNO<sub>3</sub> + 92 mL of H<sub>2</sub>O. The microstructures of the samples were observed using a Meiji optical microscope. Powder X-ray diffraction (XRD) measurements were carried out at room temperature to analyse their phases using a Rigaku diffractometer equipped with a CuK $\alpha$  radiation source, operating at 30 kV and 15 mA. Vicker's hardness measurements were performed using a Mitutoyo hardness tester with a 0.3 N load for a 12 s indentation, and the elastic modulus were measured using an ultrasonic method according to an ASTM-E494-95 standard [26,27]. Square Ti–Mo–Nb–Sn–Mn alloy samples were cut to a size of 0.5 cm<sup>2</sup> for electrochemical testing purposes, and their surfaces polished with fine 1200 grade SiC paper. The electrochemical measurement were performed on autolab 302 Multi BA electrochemical working station. The tests were carried out in a three electrode corrosion cell: Ag–AgCl as the reference electrode, platinum wire as the counter electrode, as well as working electrode. Tests were carried out in Ringer's solution at neutral pH and room temperature. The potentiodynamic polarization curve was recorder at scan rate of 0.5 mV/s.

### 3. RESULTS AND DISCUSSION

Table 1 shows the chemical compositions of the Ti–Mo–Nb–Sn–Mn ingots after being remelted five times in an arc re-melting furnace under an argon atmosphere, the results show that the measured compositions are close to the ideal compositions.

**Table 1. Chemical compositions of the As-cast Ti–Mo–Nb–Sn–Mn alloys.**

Alloy	Composition				
	Mo (wt%)	Nb (wt%)	Sn (wt%)	Mn (wt%)	Ti (wt%)
Ti–6Mo–6Nb–4Sn	5.95	6.16	4.22	-	Bal.
Ti–6Mo–6Nb–4Sn–4Mn	5.55	5.58	4.57	3.30	Bal.
Ti–6Mo–6Nb–4Sn–8Mn	5.39	5.50	4.61	7.58	Bal.
Ti–6Mo–6Nb–8Sn	5.80	5.21	7.91	-	Bal.
Ti–6Mo–6Nb–8Sn–4Mn	5.02	5.47	8.25	4.07	Bal.
Ti–6Mo–6Nb–8Sn–8Mn	5.02	5.80	7.96	7.36	Bal.

Figure 1 shows the XRD patterns of the as-cast Ti–Mo–Nb–Sn–Mn alloys, where the profiles of the quaternary Ti–6Mo–6Nb–4Sn and Ti–6Mo–6Nb–8Sn alloys show the existence of  $\alpha$  and  $\beta$  phases of titanium. Meanwhile, only the  $\beta$ -phase was observed in quinary Ti–Mo–Nb–Sn–Mn alloys.

The diffraction pattern with the  $\alpha$ -phase peak indicated that the alloy has an HCP crystal structure with  $\alpha(101)$ . From Figure 1, it can be seen that the  $\alpha$ -phase in the alloys containing 0% Mn exhibit peaks with  $2\theta$ -angle positions of 35.6°, 40.5°, 53°, 63°, and 76°. The titanium  $\alpha$ -phase peak disappeared after Mn is added. Since Mn is  $\beta$ -phase stabilizer, its addition resulted in the full  $\beta$ -phase alloy with body center cubic crystal structure at the orientations of (110), (200), (211), and (220).

The  $\beta$ -phase was detected at peaks of  $39.5^\circ$ ,  $56.9^\circ$ ,  $70.5^\circ$ ,  $85^\circ$  and  $96^\circ$

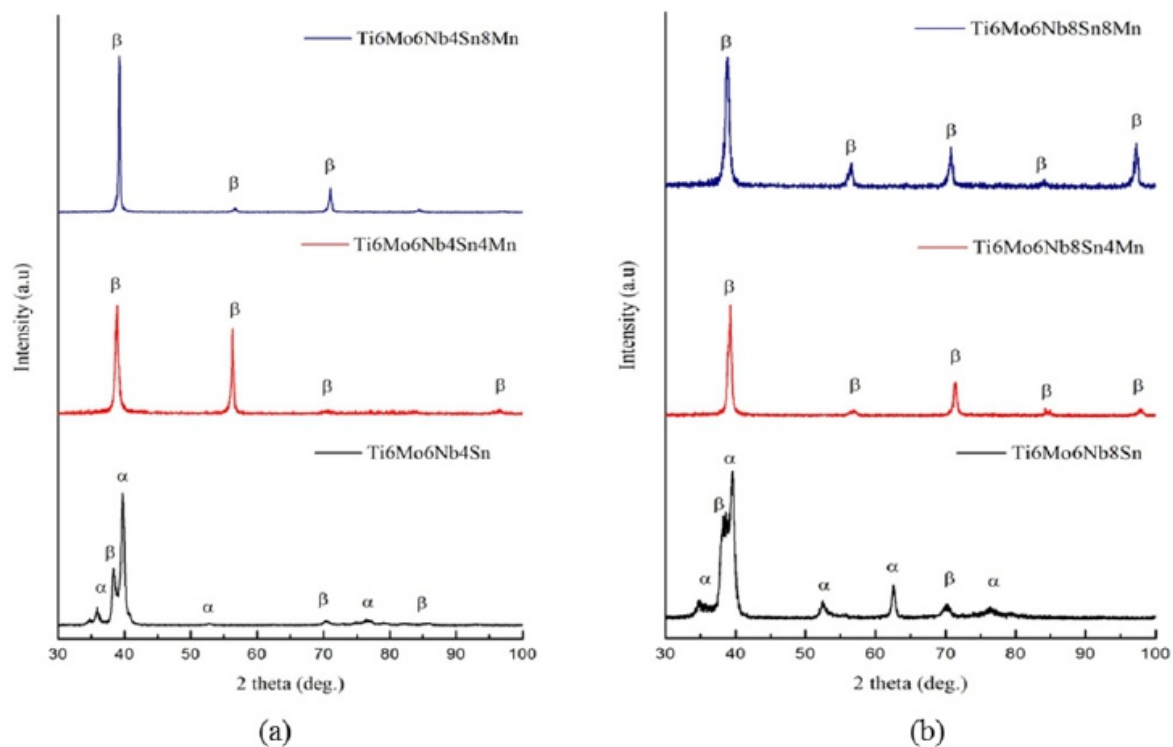


**Figure 1. Diffraction patterns of the Ti–Mo–Nb–Sn–Mn alloys.**

Moreover, Figure 1 shows that adding Mn has a positive impact on the phase constituent formation in the titanium alloys. Prior to Mn addition, the  $\alpha$  phase still existed, and then disappeared when Mn was added to the Ti–6Mo–6Nb–4Sn and Ti–6Mo–6Nb–8Sn alloys. It was previously reported by Wang that only the  $\beta$  phase was observed when 5% Sn was added to a Ti–16Nb alloy [28]. Chen also reported that the  $\alpha$  phase disappeared when 3% Mn was added to a Ti–16Nb alloy, leading to an increase in the  $\beta$  phase content [29].

Figure 2 shows optical microscope images of the microstructures of Ti–Mo–Nb–Sn–Mn alloys synthesized involving five-cycle melting process. The Figure 2a–f show that the  $\beta$ -phase titanium has equiaxed grain shapes. Upon the addition of 4% Mn increased the grain size of the  $\beta$ -phase titanium slightly. Increases Mn content up 8% Mn reduce the grain size to 100–200  $\mu\text{m}$  long grain.

Macro segregation or micro segregation was not observed in the melted samples, which negatively affected the mechanical properties of the alloys. Santos reported the increase in Ti–xMn grain size when 18% of Mn was added [25]. This phenomenon may be caused by the stability of  $\beta$  phase reaching a critical point marked by a decrease in beta transus temperature leading to the grain growth occur. The various content of Sn does not have a significant effect on the grain size. This phenomenon was also reported by Wang where grain size in titanium alloy Ti–Nb–Sn was relatively the same as polygon-shaped grains [28].

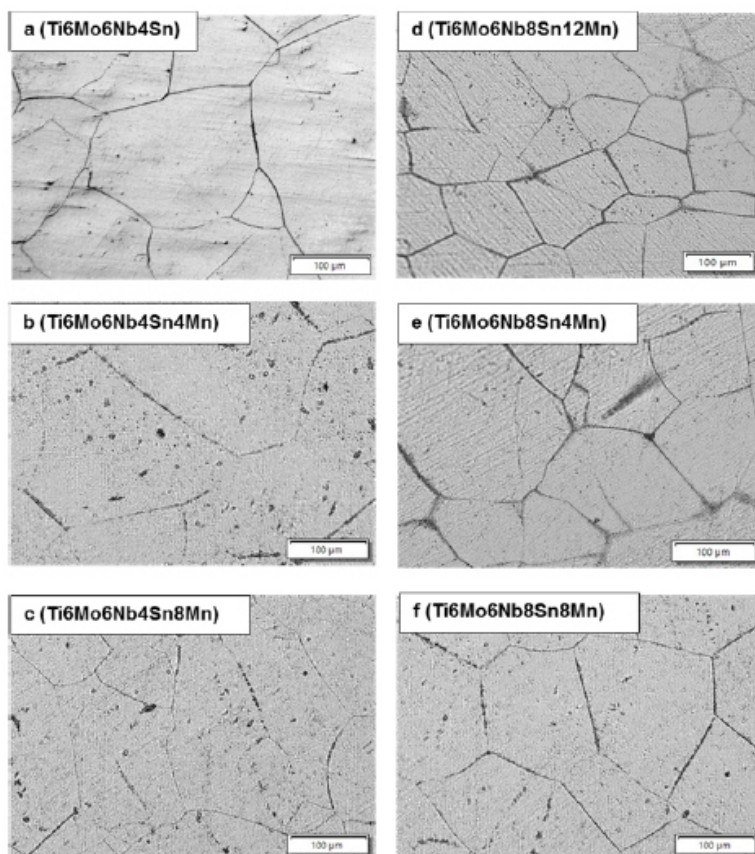


**Figure 2. Optical microscope images of the As-cast Ti–Mo–Nb–Sn–Mn alloys: (a) Ti–6Mo–6Nb–4Sn, (b) Ti–6Mo–6Nb–4Sn–4Mn, (c) Ti–6Mo–6Nb–4Sn–8Mn, (d) Ti–6Mo–6Nb–8Sn, (e) Ti–6Mo–6Nb–8Sn–4Mn, and (f) Ti–6Mo–6Nb–8Sn–8Mn.**

Figure 3 shows a plot of the Vicker's microhardness values of the Ti–Mo–Nb–Sn–Mn alloys synthesized using five-cycle melting process, it can be observed that the addition of Mn changes the hardness values of the Ti–Mo–Nb–Sn–Mn alloys. Prior to the addition of Mn, the hardness value of Ti–6Mo–6Nb–4Sn was 327 HV, which then decreased to 318 HV after the addition of 4% Mn. This decrease in the hardness values of the Ti–6Mo–6Nb–4Sn alloy upon the addition of Mn resulted from changes in the grain size of the  $\beta$  phase of the Ti–6Mo–6Nb–4Sn–xMn alloy. The finer the grain size of the  $\beta$ -phase titanium is, the higher the hardness value of Ti–6Mo–6Nb–4Sn–xMn is. However at 8% Mn and Sn, the hardness of the alloy increased indicating that the Sn and Mn addition have strong solid-solution hardening effect [24].

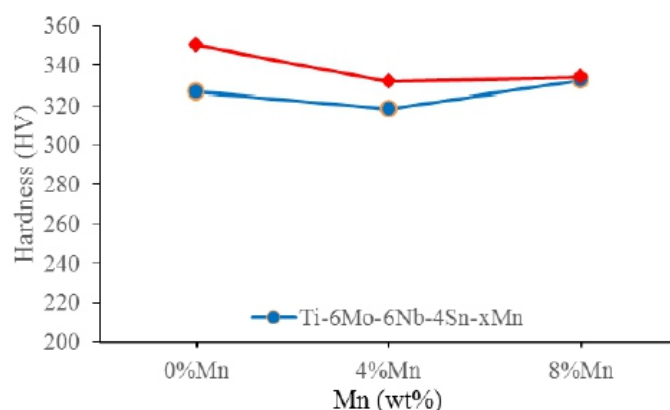


**Figure 3. Vicker's hardness values of the Ti–Mo–Nb–Sn–Mn alloys according to their Mn content.**

The hardness value of Ti–6Mo–6Nb–8Sn–xMn decreased when 4% Mn was added due to an increase in the grain size of the  $\beta$ -phase in the alloy, as shown in Figure 2d,e. However, 4% Mn was not sufficient enough to retain the grain growth in the  $\beta$  phase with higher Sn content (8% Sn). As the Mn content was increased to 8%, it began to suppress the grain growth in the  $\beta$  phase, as shown in Figure 2f, leading to a slight increase in the hardness value of the Ti–6Mo–6Nb–8Sn–8Mn alloy. The hardness value is influenced by the phase constituent of its alloy and the microstructure (phase and grain size). In Figure 2 the grain size of Ti–6Mo–6Nb–4Sn–8Mn and Ti–6Mo–6Nb–8Sn–8Mn were nearly same in size, and from the XRD pattern both alloys only contained  $\beta$  phase (no  $\alpha$  phase observed). This may cause the hardness value of both Ti–6Mo–6Nb–4Sn–8Mn and Ti–6Mo–6Nb–8Sn–8Mn to be relatively the same.

It was also found that further addition of Mn affected the change in the elastic modulus value of the Ti–6Mo–6Nb–4Sn alloy, as shown in Figure 4. The elastic modulus of the Ti–6Mo–6Nb–4Sn alloy was 103 GPa, then decreased to 94 GPa upon the addition of 4% Mn. The elastic modulus of the Ti–6Mo–6Nb–8Sn alloy decreased from 98 to 92 GPa with the addition of 4% Mn. Moreover, changes in the volume fractions of  $\alpha$  and  $\beta$  phase titanium also resulted in changes to the elastic modulus of the titanium alloys, where  $\alpha$ -phase titanium has a higher elastic modulus than that of the  $\beta$ -phase titanium, with the order of elastic modulus values following:  $\beta < \alpha'' < \alpha' < \omega$  [27].

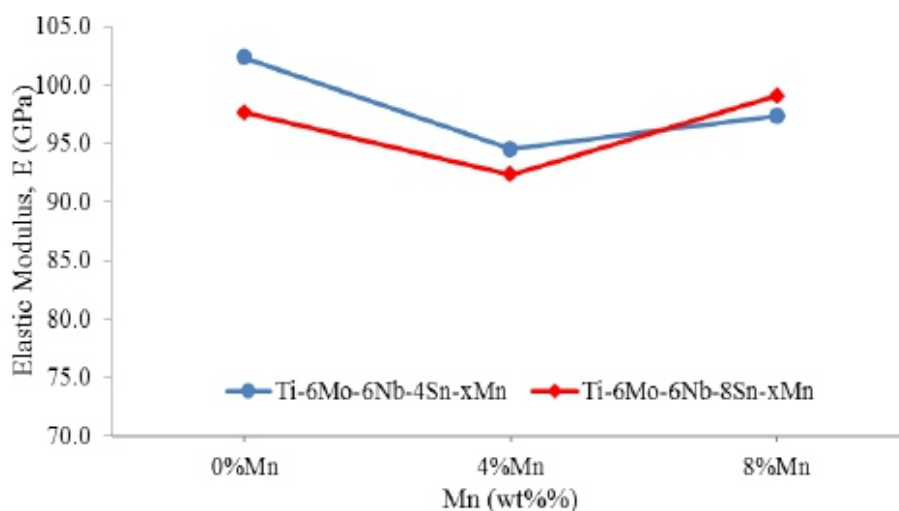


**Figure 4. Elastic modulus of the Ti–Mo–Nb–Sn–Mn alloys according to their Mn content.**

In terms of the Ti–6Mo–6Nb–4Sn alloy, its grain size increased along with the Mn content (see Figure 2a–c), resulting in increases in the strength, elastic modulus, and hardness of the alloy in line with the Hall–Petch equation. For the Ti–6Mo–6Nb–8Sn alloy, a small amount of the  $\beta$ -phase formed (Figure 1) leading to decrease in its elastic modulus with respect to that of the Ti–6Mo–6Nb–4Sn alloy (Figure 4). However, as the Mn content of the Ti–6M–6Nb–8Sn alloy was increased, some intermetallic Mn–Sn compounds may have precipitated within the grains in the form of  $\text{Mn}_3\text{Sn}$ ,  $\text{Mn}_3\text{Sn}_2$ ,  $\text{MnSn}_2$ , or  $\text{Mn}(2-x)\text{Sn}$ . These precipitates significantly hinder the mobility of dislocations, leading to an increase in the elastic modulus [30]. Compared to  $\alpha$ - $\beta$  type titanium alloys, the elastic modulus of the Ti–6Mo–6Nb-based titanium alloy is still lower than that of the Ti–6Al–4V alloy, the value of which is 115 GPa, and a  $\beta$ -type Ti–12Mo–3Nb (105 GPa) alloy [23,27].

Figure 5 shows a polarization curve of the corrosion test results of the Ti–Mo–Nb–Sn–Mn alloys in Ringer solution simulating human body fluid. Many corrosion tests were carried out on commercial Ti–6Al–4V alloy in the same solution. It was observed that both Ti–6Mo–6Nb–4Sn–xMn and

Ti–6Mo–6Nb–8Sn–xMn alloys had similar and typical passive behaviors, indicating the formation of passive film on the surface of Ti–Mo–Nb–Sn–Mn alloys

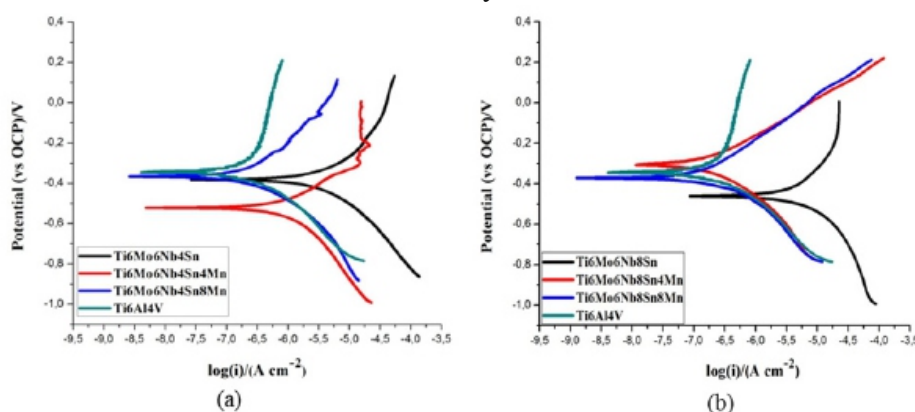


**Figure 5. Potentiodynamic polarization curves of Ti–Mo–Nb–Sn–Mn in the Ringer solution.**

Potentiodynamic polarization tests were carried out in the range of  $-1000$  mV to  $+200$  mV versus OCP for all alloys. The parameters of corrosion, corrosion potential ( $E_{\text{Corr}}$ ) and corrosion current density ( $i_{\text{corr}}$ ) were obtained from the tafel area. The corrosion current represents the degree of degradation of the alloy and is used to determine the corrosion rate of the alloy. Different passive areas were observed on the anodic polarization curves, of which the formation of passive films occurs.

Corrosion rate was calculated from the corrosion current density using the equation according to ASTM Standard G102-89 [31].

Table 2 summarized the electrochemical parameters, such as corrosion potential ( $E_{\text{corr}}$ ) and corrosion current density ( $i_{\text{corr}}$ ) of Ti–Mo–Nb–xSn–xMn alloys in Ringer solution. The  $i_{\text{corr}}$  of the alloys prior to Mn addition showed the values of  $3.162$  and  $5.010$   $\mu\text{A}/\text{cm}^2$ . The  $i_{\text{corr}}$  value subsequently decreased with increasing of Mn content. The potentiodynamic corrosion test data shown in Table 2 also provide evidence that the Ti–6Mo–6Nb–4Sn–4Mn, Ti–6Mo–6Nb–4Sn–8Mn, Ti–6Mo–6Nb–8Sn–4Mn, and Ti–6Mo–6Nb–8Sn–8Mn alloys have better corrosion resistance than that of the commercial Ti–6Al–4V in the Ringer solution, with the Ti–6Mo–6Nb–8Sn–4Mn alloy showing the lowest corrosion rate of  $0.0016$  mm per year (mmpy). Tsao reported that adding Sn to a Ti–7Cu titanium alloy increased its corrosion resistance in NaCl solution [32]. He also carried out energy-dispersive X-ray spectroscopic (EDS) tests to determine the elements present in the alloys after the potentiodynamic corrosion tests, where the results showed the formation of a passive layer in the form of TiO, CuO, and SnO on the surface of a Ti–Cu–Sn alloy [32]. In a heat-treated Az91 magnesium alloy, additional Mn increased the corrosion potential, lowered the corrosion current density, and reduced the corrosion rates, similar to what has been observed in Ti–Mo–Nb–Sn–Mn alloys [33].

**Table 2. Corrosion parameters of the Ti–6Mo–6Nb–xSn–xMn alloy in the Ringer solution.**

Alloy	Corrosion potential $E_{\text{corr}}$ ( $V_{\text{Ag}/\text{AgCl}}$ )	Corrosion current density $i_{\text{corr}}$ ( $\mu\text{A}/\text{cm}^2$ )	Corrosion rate (mmpy)
Ti–6Mo–6Nb–4Sn	–0.383	3.162	0.04934
Ti–6Mo–6Nb–4Sn–4Mn	–0.522	0.633	0.00972
Ti–6Mo–6Nb–4Sn–8Mn	–0.367	0.131	0.00198
Ti–6Mo–6Nb–8Sn	–0.461	5.010	0.07838
Ti–6Mo–6Nb–8Sn–4Mn	–0.306	0.112	0.00160
Ti–6Mo–6Nb–8Sn–8Mn	–0.372	0.127	0.00163
Ti–6Al–4V	–0.350	0.316	0.00504

#### 4. CONCLUSIONS

The Mn and Sn addition had a positive impact on the formation of  $\beta$ -phase titanium in Ti–Mo–Nb–Sn–Mn alloy and reduced  $\alpha$ -phase formation in the  $\beta$ -phase matrix. Due to the reduction of  $\alpha$ -phase content, sample hardness and elastic modulus of  $\beta$ -phase alloy were lower than that of  $\alpha$ - $\beta$  titanium alloy. Moreover, the alloys with stood the formation of  $\alpha$ -phase titanium. The higher the Mn and Sn content, the lower the amount of  $\alpha$ -phase titanium, and the more  $\beta$ -phase titanium were formed. The addition of 4% Mn to this alloy led to the formation of full  $\beta$ -phase titanium with an optimum modulus of elasticity of 92 GPa. It is suggested that the further addition of Mn enhances the corrosion resistance of Ti–6Mo–6Nb–8Sn alloys. The optimum corrosion rate of this alloy was also achieved upon the addition of 4% Mn. To ensure the biocompatibility of these alloys, further studies should be conducted to determine the optimum Mn content without sacrificing the balance of the mechanical properties and corrosion resistance in various simulated body fluids.

#### Acknowledgements

We would like to thank Directorate of Researches and Community Service, Universitas Indonesia (DRPM UI) for their financial support through the TADok grant funds with the contract number NKB-0155/UN2.R3.1/HKP.05.00/2019 and for helping us conduct this study.

#### Conflicts of interests

All authors declare no conflicts of interest in this paper.

#### REFERENCES

- [1] Park JB (1984) *Biomaterials Science and Engineering*, Boston: Springer.
- [2] Niinomi M, Nakai M, Hieda J (2012) Development of new metallic alloys for biomedical applications. *Acta Biomater* 8: 3888–3903.
- [3] Chen Q, Thouas GA (2015) *Metallic implant biomaterials*. *Mat Sci Eng R* 87: 1–57.
- [4] Geetha M, Singh AK, Asokamani R, et al. (2009) Ti based biomaterials, the ultimate choice for orthopaedic implants—A review. *Prog Mater Sci* 54: 397–425.
- [5] He G, Hagiwara M (2006) Ti alloy design strategy for biomedical applications. *Mat Sci Eng Cmater* 26: 14–19.
- [6] Li Y, Yang C, Zhao H, et al. (2014) New developments of Ti-based alloys for biomedical applications. *Materials* 7: 1709–1800.
- [7] Hsu H, Wu S, Hsu S, et al. (2013) The structure and mechanical properties of as-cast Ti–25Nb–xSn alloys for biomedical applications. *Mat Sci Eng A-Struct* 568: 1–7.
- [8] Plecko M, Sievert C, Andermatt D, et al. (2012) Osseointegration and biocompatibility of different metal implants—a comparative experimental investigation in sheep. *BMC Musculoskel Dis* 13: 32.
- [9] Rack HJ, Qazi JI (2006) Titanium alloys for biomedical applications. *Mat Sci Eng C-Mater* 26: 1269–1277.
- [10] Gepreel MA, Niinomi M (2013) Biocompatibility of Ti-alloys for long-term implantation. *J Mech Behav Biomed* 20: 407–415.
- [11] Senopati G, Sutowo C, Kartika I, et al. (2019) The effect of solution treatment on microstructure and mechanical properties of Ti–6Mo–6Nb–8Sn alloy. *Mater Today* 13: 224–228.
- [12] Davis JR (2003) *Handbook of Materials for Medical Devices*. American: ASM International- Materials Park.
- [13] Ballo A, Moritz N (2010) *Biomechanics concepts of bone-oral implan interface*, In: Levy JH, *Biomechanics: Principles, Trends, and Applications*, New York: Nova Science Publisher, 117.
- [14] Mohammed MT, Khan ZA, Siddiquee AN (2014) Beta titanium alloys: the lowest elastic modulus for biomedical applications: a review. *Int J Chem Mol Nucl Mater Metall Eng* 8: 726–731.
- [15] Kollu RP (2018) A review of metastable beta titanium alloys. *Metals* 8: 1–41.
- [16] De Mello MG, Salvador CF, Cremasco A, et al. (2015) The effect of Sn addition on phase stability and phase evolution during aging heat treatment in Ti–Mo alloys employed as biomaterials. *Mater Charact* 110: 5–13.
- [17] Xu L, Xiao S, Tian J, Chen Y (2013) Microstructure, mechanical properties and dry wear resistance of  $\beta$ -type Ti–15Mo–xNb alloys for biomedical applications. *T Nonferr Metal Soc* 23: 692–698.

- [18] Lu J, Zhao Y, Ge P, et al. (2013) Microstructure and beta grain growth behavior of Ti–Mo alloys solution treated. *Mater Charact* 84: 105–111.
- [19] Cho K, Niinomi M, Nakai M, et al. (2016) Improvement in mechanical strength of low cost beta type Ti–Mn alloys fabricated by metal injection molding through cold rolling. *J Alloy Compd* 664: 272–283.
- [20] Markovs PE, Ikeda M (2013) Influence of alloying elements on the aging of economically alloyed metastable titanium beta alloy. *Mater Sci* 49: 78–84.
- [21] Ehtemam-Haghighi S, Cao G, Zhang LC (2016) Nano indentation study of mechanical properties of Ti based alloys with Fe and Ta additions. *J Alloy Compd* 692: 892–897.
- [22] Narita K, Niinomi M, Nakai M, et al. (2012) Development of thermo-mechanical processing for fabricating highly durable  $\beta$ -type Ti–Nb–Ta–Zr rod for use in spinal fixation devices. *J Mech Behav Biomed* 9: 207–216.
- [23] Gabriel SB, Panaino JVP, Santos ID, et al. (2012) Characterization of a new beta titanium alloy Ti–12Mo–3Nb for biomedical applications. *J Alloy Compd* 536: S208–S210.
- [24] Zhang DC, Yang S, Wei M, et al. (2012) Effect of Sn addition on the microstructure and superelasticity in Ti–Nb–Mo–Sn alloys. *J Mech Behav Biomed* 13: 156–165.
- [25] Santos PF, Niinomi M, Cho K, et al. (2015) Microstructures, mechanical properties and cytotoxicity of low cost beta Ti–Mn alloys for biomedical applications. *Acta Biomater* 26: 366–376.
- [26] ASTM International (1995) Standard practice for measuring ultrasonic velocity in materials. ASTM E494-95. Available from: <https://www.astm.org/DATABASE.CART/HISTORICAL/E494-95.htm>.
- [27] Majumdar P, Singh SB, Chakraborty M (2008) Elastic modulus of biomedical titanium alloys by nano-indentation and ultrasonic techniques—A comparative study. *Mater Sci Eng A-Struct* 489: 419–425.
- [28] Wang BL, Zheng YF, Zhao LC (2008) Effects of Sn content on the microstructure, phase constitution and shape memory effect of Ti–Nb–Sn alloys. *Mater Sci Eng A-Struct* 486: 146–151.
- [29] Chen Z, Liu Y, Jiang H, et al. (2017) Microstructures and mechanical properties of Mn modified Ti–Nb-based alloys. *J Alloy Compd* 723: 1091–1097.
- [30] Aljarrah M, Obeidat S, Fouad RH, et al. (2015) Thermodynamic calculations of the Mn–Sn, Mn–Sr and Mg–Mn–{Sn, Sr} systems. *IET Sci Meas Technol* 9: 681–692.
- [31] ASTM International (1999) Standard practice for calculation of corrosion rates and related information from electrochemical measurements. ASTM G102-89. Available from: <https://www.astm.org/DATABASE.CART/HISTORICAL/G102-89R99.htm>
- [32] Tsao LC (2015) Effect of Sn addition on the corrosion behavior of Ti–7Cu–Sn cast alloys for biomedical applications. *Mater Sci Eng C-Mater* 46: 246–252.
- [33] Li XY, Li MZ, Fan LQ, et al. (2014) Effects of Mn on corrosion resistant property of Az91 alloys. *Rare Metal Mater Eng* 43: 278–282.

# Instructions for Authors

## Essentials for Publishing in this Journal

- 1 Submitted articles should not have been previously published or be currently under consideration for publication elsewhere.
- 2 Conference papers may only be submitted if the paper has been completely re-written (taken to mean more than 50%) and the author has cleared any necessary permission with the copyright owner if it has been previously copyrighted.
- 3 All our articles are refereed through a double-blind process.
- 4 All authors must declare they have read and agreed to the content of the submitted article and must sign a declaration correspond to the originality of the article.

## Submission Process

All articles for this journal must be submitted using our online submissions system. <http://enrichedpub.com/> . Please use the Submit Your Article link in the Author Service area.

---

## Manuscript Guidelines

The instructions to authors about the article preparation for publication in the Manuscripts are submitted online, through the e-Ur (Electronic editing) system, developed by **Enriched Publications Pvt. Ltd.** The article should contain the abstract with keywords, introduction, body, conclusion, references and the summary in English language (without heading and subheading enumeration). The article length should not exceed 16 pages of A4 paper format.

### Title

The title should be informative. It is in both Journal's and author's best interest to use terms suitable. For indexing and word search. If there are no such terms in the title, the author is strongly advised to add a subtitle. The title should be given in English as well. The titles precede the abstract and the summary in an appropriate language.

### Letterhead Title

The letterhead title is given at a top of each page for easier identification of article copies in an Electronic form in particular. It contains the author's surname and first name initial .article title, journal title and collation (year, volume, and issue, first and last page). The journal and article titles can be given in a shortened form.

### Author's Name

Full name(s) of author(s) should be used. It is advisable to give the middle initial. Names are given in their original form.

### Contact Details

The postal address or the e-mail address of the author (usually of the first one if there are more Authors) is given in the footnote at the bottom of the first page.

### Type of Articles

Classification of articles is a duty of the editorial staff and is of special importance. Referees and the members of the editorial staff, or section editors, can propose a category, but the editor-in-chief has the sole responsibility for their classification. Journal articles are classified as follows:

#### Scientific articles:

1. Original scientific paper (giving the previously unpublished results of the author's own research based on management methods).
2. Survey paper (giving an original, detailed and critical view of a research problem or an area to which the author has made a contribution visible through his self-citation);
3. Short or preliminary communication (original management paper of full format but of a smaller extent or of a preliminary character);
4. Scientific critique or forum (discussion on a particular scientific topic, based exclusively on management argumentation) and commentaries. Exceptionally, in particular areas, a scientific paper in the Journal can be in a form of a monograph or a critical edition of scientific data (historical, archival, lexicographic, bibliographic, data survey, etc.) which were unknown or hardly accessible for scientific research.

**Professional articles:**

1. Professional paper (contribution offering experience useful for improvement of professional practice but not necessarily based on scientific methods);
2. Informative contribution (editorial, commentary, etc.);
3. Review (of a book, software, case study, scientific event, etc.)

**Language**

The article should be in English. The grammar and style of the article should be of good quality. The systematized text should be without abbreviations (except standard ones). All measurements must be in SI units. The sequence of formulae is denoted in Arabic numerals in parentheses on the right-hand side.

**Abstract and Summary**

An abstract is a concise informative presentation of the article content for fast and accurate Evaluation of its relevance. It is both in the Editorial Office's and the author's best interest for an abstract to contain terms often used for indexing and article search. The abstract describes the purpose of the study and the methods, outlines the findings and state the conclusions. A 100- to 250-Word abstract should be placed between the title and the keywords with the body text to follow. Besides an abstract are advised to have a summary in English, at the end of the article, after the Reference list. The summary should be structured and long up to 1/10 of the article length (it is more extensive than the abstract).

**Keywords**

Keywords are terms or phrases showing adequately the article content for indexing and search purposes. They should be allocated heaving in mind widely accepted international sources (index, dictionary or thesaurus), such as the Web of Science keyword list for science in general. The higher their usage frequency is the better. Up to 10 keywords immediately follow the abstract and the summary, in respective languages.

**Acknowledgements**

The name and the number of the project or programmed within which the article was realized is given in a separate note at the bottom of the first page together with the name of the institution which financially supported the project or programmed.

**Tables and Illustrations**

All the captions should be in the original language as well as in English, together with the texts in illustrations if possible. Tables are typed in the same style as the text and are denoted by numerals at the top. Photographs and drawings, placed appropriately in the text, should be clear, precise and suitable for reproduction. Drawings should be created in Word or Corel.

**Citation in the Text**

Citation in the text must be uniform. When citing references in the text, use the reference number set in square brackets from the Reference list at the end of the article.

**Footnotes**

Footnotes are given at the bottom of the page with the text they refer to. They can contain less relevant details, additional explanations or used sources (e.g. scientific material, manuals). They cannot replace the cited literature.

The article should be accompanied with a cover letter with the information about the author(s): surname, middle initial, first name, and citizen personal number, rank, title, e-mail address, and affiliation address, home address including municipality, phone number in the office and at home (or a mobile phone number). The cover letter should state the type of the article and tell which illustrations are original and which are not.

**Address of the Editorial Office:**

**Enriched Publications Pvt. Ltd.**  
S-9, IInd FLOOR, MLU POCKET,  
MANISH ABHINAV PLAZA-II, ABOVE FEDERAL BANK,  
PLOT NO-5, SECTOR -5, DWARKA, NEW DELHI, INDIA-110075,  
PHONE: - + (91)-(11)-45525005